Ultrafast Fluorescence Upconversion of Alloyed III-V/II-VI Core/Shell Quantum Dots

By

Nathaniel Johnson Freymeyer

Dissertation
Submitted to the Faculty of the
Graduate School of Vanderbilt University
in partial fulfillment of the requirements
for the degree of

DOCTOR OF PHILOSOPHY

in
Chemistry

May 8, 2020
Nashville, Tennessee

Approved:

Sandra J. Rosenthal, Ph. D.

Timothy P. Hanusa, Ph. D.

John A. McLean, Ph. D.

Richard F. Haglund, Ph. D.

ACKNOWLEDGEMENTS

I would like to thank my PI, Dr. Sandra J. Rosenthal, for allowing me to join her lab despite my limited knowledge on ultrafast lasers, and for allowing me to grow and learn. I would also like to thank the rest of my committee, Dr. Timothy P. Hanusa, Dr. John A. McLean, Dr. Richard F. Haglund, for taking their time to guide me throughout this process.

All of the lab members past and present have helped contributed towards my completion of the work. Especially, Dr. James McBride for help in figuring out the best way to reword that pesky sentence or in figuring out the best way to present data so that everyone can understand it. Your feedback was critical towards my growth as a chemist. Your electron microscopy skills have provided many of the figures throughout this document. Dr. Joseph Keene, thanks for teaching me the upconversion experiment and putting up with my inability to find upconverted signal for the longest time. Without your initial training and guidance on the laser system, none of this work would have been possible. Dr. Noah Orfield, thank you for helping out with the laser whenever Kemar and I could not get it to work and passing along your knowledge. Dr. Kemar Reid, the initial InP/ZnSe samples that you provided helped figure out the best structures for analysis with the upconversion experiments. I also appreciate how you were always willing to try and determine why the laser system quit functioning as expected or determining what that line in the manual actually meant.

The work in this dissertation would not be possible without the help of Sophie Click, who provided the thick-shell InP/ZnSe samples analyzed and repeatedly cleaned up additional sample in the glove box without complaining. Best of luck in wrapping up another project on InP/ZnSe!

Dr. Talitha VanWie, thank you for being the senior graduate student during most of my graduate school career and trying to figure out how to navigate the process. You were also valuable whenever I went into the wet lab and could not remember where anything was located. It was so much fun going to a bunch of #VandyBoys baseball games with you (and Will) on their way to a National Championship! Dr. Oleg Kovtun, while you were on the bio-side of lab your understanding of how things worked were critical to my success in graduate school.

A special thank you to my parents and sister for always supporting me throughout the process and constantly checking in on how I was doing. I also appreciate how both of my grandmothers always wanted to make sure that I obtained the best education possible and constantly asked how things were going despite not understanding anything that I was doing. Without the support of my family, I would not have been successful in earning my degree.

I would also like to acknowledge funding from the National Science Foundation research grant CHE-1506587.

TABLE OF CONTENTS

Page

LIST OF TABLES

LIST OF FIGURES

Figure Page

CHAPTER I

INTRODUTION

1.1 SEMICONDUCTOR NANOCRYSTALS

Quantum dots (QDs) are semiconductor nanocrystals with at least one dimension on the nanoscale that exhibit unique size-tunable absorption and emission properties because of quantum confinement.[1] Additionally, their narrow photoluminescence-line widths, high photostability, and increased brightness make them useful for numerous potential applications. QDs with different elemental compositions, structures, and sizes have been synthesized and optimized for various applications ranging from solar cells, lasers, biological labeling and tracking, to solar concentrators.[2-8] Commercially, QDs are available for biological labeling and are used in high-end display technology including Samsung's QLED TVs and Kindle Fire tablets.

Cadmium selenide (CdSe)-based QDs are the most well studied QD system and nanocrystals have been synthesized with a wide variety of structures, sizes, and surface ligands. Since the Bohr exciton diameter of CdSe is 11.2 nm, any QDs synthesized with a size of less than 11.2 nm will exhibit quantum confinement.[9] Merely by changing the size of the QDs, their absorption and emission can be changed to cover the entire visible spectrum.[10] With the help of surface state emission, single source white light emitting ultrasmall CdSe QDs have also been synthesized.[11]

More recently, work is shifting away from heavy-metal containing structures (such as CdSe) towards those that are made from less toxic materials such as indium phosphide (InP), copper indium sulfide (CIS), and zinc nitride (Zn_3N_2). These materials still have wavelength tunable absorption and emission properties stemming from quantum confinement but lack the synthetic development that has been carried out for Cd-based QDs. New research is focusing on developing these emerging materials to have the same optical properties and structural robustness as that currently available for Cd-based QDs.

1.1.1 Quantum Confinement

In bulk materials, the valence band and conduction band are made up of continuous states which are separated by a material dependent band gap. The band gap (E_g) of a bulk semiconductor material is defined as the energy necessary to excite an electron to the valence band (VB) and form a hole in the conduction band (CB) at rest with respect to the lattice and far enough apart such that their Coulomb attraction is negligible. An exciton pair is formed when the hole and electron approach one another and become closer than the band gap. The hole and electron are bound together by an attractive coulombic interaction, with the distance between the electron and hole known as the Bohr exciton diameter (a_B).[1, 12]

Louis E. Brus first proposed the idea that electronic properties of small materials behave differently from those in the bulk in 1984.[1] Because the size of a QD is smaller than the Bohr exciton radius, QDs have distinct energy levels that allow for size- and shape-tunable absorption and emission properties.[13] Instead of the exciton having electron-hole Coulomb interaction, the physical dimensions of the material force the electron and hole wavefunctions to overlap.[12] As the QDs become smaller, the size of the band gap increases to account for the additional energy required by the stronger wavefunction overlap. This change is attributed to a reduction in the density of states as the size of the QDs decreases and can be modeled by the Brus equation:

$$E_{ex} = \frac{\hbar^2\pi^2}{2R^2}\left(\frac{1}{m_e} + \frac{1}{m_h}\right) - \frac{1.8e^2}{\varepsilon_2 R} + \frac{e^2}{R}\overline{\sum_{n=1}^{\infty}\alpha_n\left(\frac{S}{R}\right)^{2n}} \qquad (1.1)$$

in which ħ is the reduced Planck's constant; R is the nanocrystal radius; m_e and m_h are the effective masses of the electron and hole, respectively; e is the absolute charge of an electron; ε_2 is the dielectric constant of the semiconductor material; α_n is a constant that relates the dielectric constants of the semiconductor material and the surrounding medium; and S is the wavefunction that describes the position of the electron and hole in the 1S exciton.[1] As the size of the QD gets smaller, the nanocrystal radius in the denominator of the first term will dominate which results in the large change in band gap observed. Therefore, changes to a QDs' absorbance and photoluminescence can be obtained by merely changing the size of the QD as can be seen in Figure 1.1. Figure 1.2 summarizes this change in the density of states.

Figure 1.1. CdSe nanocrystals ranging from ultrasmall white light emitting (left) to ~7 nm red emitting (right). These QDs exhibit the size dependance of quantum confinement.

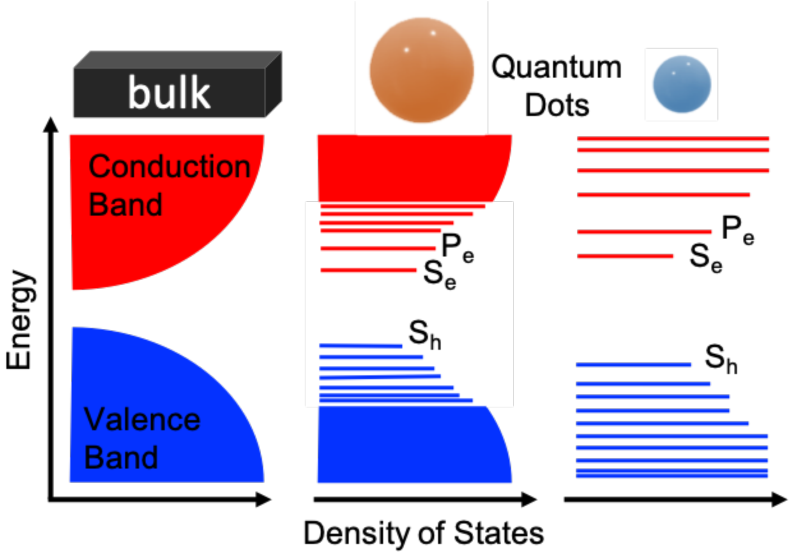

Figure 1.2. Quantum confinement in semiconductor QDs. As the size of the QD gets smaller the distance between the condcution band and valence band increses which correlates to an increase in the band gap of the material and a blue-shift in both the absorbance and fluroescence wavelengths.

1.1.2 Importance of Nanocrystal Surface on Charge Carrier Behavior

The simplest colloidal QD structure consists of an inorganic core made of a semiconductor material with a layer of organic ligands on the surface. With the small size of QDs, a large portion of the atoms are located on its surface. For example, 8.5 nm nanocrystals have 20% surface atoms and 1.2 nm nanocrystals have 88% surface atoms. Ultrasmall QDs (<2 nm) are so small that they move from quantum confined emission to emission that is dominated by the surface states.[11, 14, 15] While QDs offer size-tunable emission and absorption properties, their as-synthesized photoluminescence quantum yield (PLQY) remain low. The surface provides many potential trap states including unpassivated dangling bonds that serve as sites for carrier localization, prevent radiative recombination, and lower PLQY.[16] With this large surface area-to-volume ratio, the surface's properties dictate its properties. To improve their fluorescence efficiency, increase their lifetime, and reduce their intermittency, the number of available trap sites in QDs needs to be decreased with the use of surface passivation.[17, 18]

One method of surface passivation involves adding a shell of a wide bandgap material to the inorganic QD core. Hines and Guyot-Sionnest applied a shell of a wide band gap material, ZnS, on the surface of CdSe QDs as a method of reducing carrier localization at these unpassivated atoms and dangling bonds on the surface.[19] This CdSe/ZnS core/shell QD showed an increased PLQY because the excited charge carriers were both structurally and electronically confined to the core of the QD, and allowed for their use in fluorescence-based biological detection.[19-21] The wide bandgap material used in shelling varies for different core materials to ensure that the band gap is of high enough energy to confine the charge carriers and of sufficient lattice constant to reduce lattice strain between the core and the shell.[22] To that extent, highly luminescent Cd-based nanostructures of many materials have been synthesized including CdSe/CdS, CdTe/CdSe, CdSe/ZnTe, and CdSe(ZnCdS).[23-25]

Furthermore, addition of a cosolvent has also been shown to reduce surface defects by passivating atoms and dangling bonds on the surface of core QDs.[26-28] Hexadecylamine (HDA) has been used as a cosolvent and been shown to narrow the size and shape distribution of CdSe QDs.[29] Additionally, this co-surfactant substantially reduces the observed deep trap emission seen for those CdSe QDs synthesized without HDA.[26] By reducing the number of deep traps, the excitons recombine radiatively more often leading to a higher PLQY and overall more efficient nanocrystal system.

Recent work has suggested that QDs have a dynamic nanocrystal surface whereby the surface atoms are in a state of dynamic flux under excitation which causes the surface and subsurface states to change.[17, 30] Ultrasmall white light emitting nanocrystals (NCs) were observed using aberration-corrected scanning transmission electron microscopy (STEM) videos which showed disordered fluxional surface layers composing most of the particle and leading to white light emission.[30] NCs of larger sizes showed similar movement of the surface layers.[17] Finite-temperature density functional theory (DFT) also supported this idea of a dynamic NC surface.[30] In addition to mid-gap trap states, this dynamic NC surface needs to be controlled for QDs to have optimal photophysical properties including efficient radiative recombination. Decoupling the exciton from the NC surface is vital for obtaining optimal photophysical properties and suggests the use of a wide band gap material shell as a more effective mode of surface passivation whereby the surface layers would then not influence charge carrier recombination.

Aberration-corrected atomic number scanning transmission electron microscopy (Z-STEM) on both CdSe/ZnS and CdSe/CdS has shown, however, that traditional shelling methods are not completely passivating the core and instead have preferential growth on anion-terminated facets.[31] This preferential growth means other facets still possess dangling bonds and unpassivated surface atoms. Thicker shells (~18 monolayers) show more complete shell coverage, but involve longer synthesis times and are not ideal for many applications.[32] To form a more uniform shell, a graded interface between the core and shell of CdS/ZnS QDs and CdSe/CdS has been used and shown to help increase the PLQY.[31, 33] Alloying also helps to ensure that the lattice mismatch introduced by combining two distinct materials together does not detrimentally affect the overall properties of the QDs by reducing the lattice at the interface.[34]

High surface area-to-volume ratios, surface dangling bonds, and dynamic nanocrystal surfaces require activate minimization to optimize the photophysical properties of semiconductor nanocrystals.[26, 35] With a large number of defects, charge carrier localization prevents radiative recombination. By reducing the number of defects at both the interface and on the surface, the extent of radiative recombination can be increased to create QDs with better overall photophysical properties.

1.2 ULTRAFAST SPECTROSCOPY

Charge carriers in quantum dots recombine on the scale of hundreds of nanoseconds, but charge carrier localization occurs much more quickly, within the first few picoseconds after excitation which necessitate laser techniques that offer sub-picosecond resolution.[36] Ultrafast spectroscopy allows the speed and extent of various trapping mechanisms to be measured on the femtosecond timescale and then correlated to changes in the QDs' structure or composition. CdSe-based QDs have been extensively studied using many time-resolved spectroscopic techniques including transient absorption, fluorescence upconversion, photon echo, and transient grating spectroscopies to investigate how changes to the QDs' structure affects its photophysical properties.[26, 37-41] Actual total coverage of the shell, differences in shell coverage between nanocrystals in the same batch, and defects at the core/shell interface must be optimized for each QD system to tune its properties towards a specific application.[31]

1.2.1 Technique and Information Obtained

Ultrafast fluorescence upconversion spectroscopy allows for preferential probing of the radiative state of a QD system immediately after excitation and without interference from other processes. This spectroscopy technique enables the effectiveness of the surface passivation of either surface ligands or a shelling material to be determined by measuring a reduction in radiative recombination. [14, 26, 34, 35, 42-44] Nonradiative recombination that is caused by carrier localization (trapping) on the QD surface or within its structure quenches fluorescence. Ultrafast fluorescence upconversion spectroscopy allows changes in radiative recombination to be observed by monitoring the fluorescence decay caused by hole trapping, electron trapping, and exciton lifetime on the pico- to femtosecond timescale. The rate and extent that each of these processes contributes to the overall QD's photophysical properties can be determined and then compared to changes in the QDs' structure. Additionally, the time between laser excitation and when the sample begins emitting can be determined and compared. The carrier dynamics evaluated by this technique are summarized in Figure 1.3.

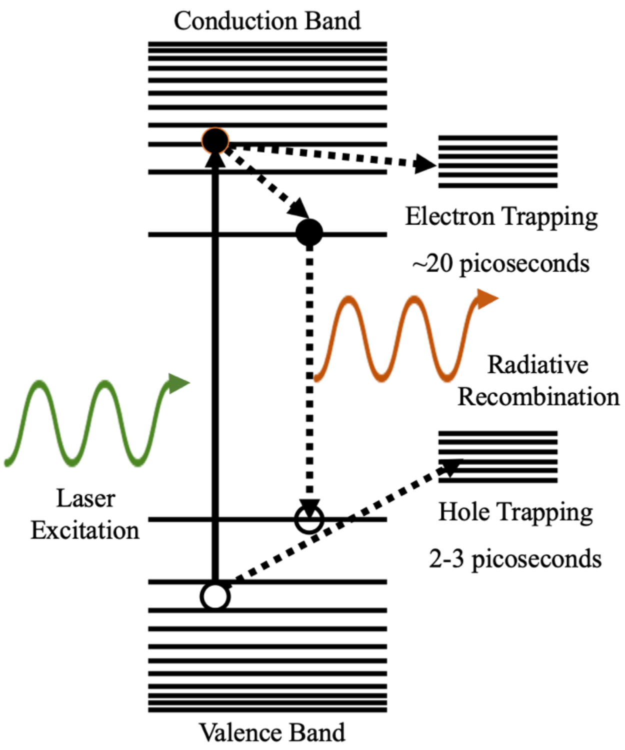

Figure 1.3. Summary of charge carrier dynamics in semiconductor QDs. When an electron is excited from the valence band to the conduction band, a hole is left in the valence band. Ideally the charge carriers recombine and give off light in the form of fluorescence; however, non-radiative processes such as hole and electron trapping reduce the efficiency of QDs. Trapping of charge carriers can occur at the surface of the QD, at a core/shell interface, and at defects in the QD's crystal structure.

Extensive research on the ultrafast carrier dynamics of CdSe-based QDs has been conducted in the Rosenthal Lab to observe how different passivation techniques affect the surface morphology of a QD and thus the extent of charge carrier trapping.[26, 34, 35, 42] Initial work developed a model for exciton relaxation in various sized tri-n-octylphosphine oxide (TOPO)-capped CdSe QDs consisting of both band edge and deep trap dynamics. An initial large amplitude is associated with direct electron/hole recombination from band edge states and falls off rapidly in the first 2-6 picoseconds (ps) as the charge carriers become localized. In these CdSe QDs, a mid-gap trap state exists, caused by surface selenium dangling bonds, which quickly trap the hole based off of its larger effective mass and reduces the observed fluorescence intensity. Additionally, surface cadmium atoms fall close to the conduction band and serve as electron traps. A portion of the excitons also relax to a long-lived triplet state located near the valence band which eventually recombines with a hole and causes the long-lived portion on the observed band edge dynamics.[45] The mid-gap trapping that reduces observed band edge recombination enables the deep trap emission whereby a photogenerated hole recombines with a surface selenium dangling bond electron.[46] The deep trap emission increasing at approximately the same time as the band edge decreases provides further evidence for hole trapping as the fast initial decay process.[42]

Other groups have also used various different ultrafast techniques to develop a relaxation scheme for CdSe QDs. Weiss *et al.* used transient absorption (TA) spectroscopy and time-resolved photoluminescence to probe electron, hole, and band edge relaxation, and found six exponential components of decay. By comparing the TA signals in the near-infrared and visible they determined the extent of electron and hole dynamics to each component. Three distinct populations of NCs were found that each had different radiative and nonradiative decay pathways.[47] Jones *et al.* used Marcus electron transfer theory to determine the temperature-dependent NC trap state dynamics.[48, 49] Kern *et al.* have suggested that at the single-NC level, each CdSe NC exhibits single exponential decay and that the reported multiexponential decays are merely resulting from sample heterogeneity.[50] Alternatively, work by Lian, Gómez-Campos and others have suggested an Auger-assisted electron transfer model for multiple different QDs.[51, 52] While differences exist in how people view the relaxation scheme, everyone acknowledges that the surface plays a crucial role in the carrier dynamics of QDs.

Using knowledge that defects can be detrimental to radiative recombination, QDs were then synthesized with the goal of preventing hole trapping in the dangling selenium bonds. Early work focused on the addition of multiple organic ligands to improve QDs' properties. For example, adding a co-surfactant, hexadecylamine (HDA), helps to passivate the surface and reduces the number of trap states available for holes and improves the radiative recombination that is observed. Additionally, passivation with HDA narrowed the size distribution, reduced the number of shape abnormalities, and removed the broad deep trap emission by reducing the number of available mid-gap trap sites.[26, 27, 43] Using ultrafast fluorescence upconversion spectroscopy, an increase in the time constant for the short-lived component of the fluorescence of the TOPO/HDA QDs was observed when compared to the same component for TOPO-only QDs. Longer time constants indicated more efficient radiative recombination caused by a reduction in trap states within the QDs.[26]

For these TOPO/HDA CdSe QDs, radiative lifetime decreased with size because of increased electron/hole wave function overlap and increased interaction with the surface.[42] Extensive time constants and relative amplitudes were obtained for TOPO/HDA QDs of various sizes and showed an increase in both the short-lived and long-lived components of the fluorescence lifetime at the band edge with increasing QD size.[43] A reduction in the surface area-to-volume ratio means that fewer defects exist per nanocrystal volume and that the charge carriers are more likely to recombine radiatively.[26]

As discussed earlier, shelling CdSe with a wide band gap material such as CdS, ZnS, or ZnSe has also been shown to increase the quantum yield of unpassivated core nanocrystals by passivating the dangling bonds on the surface and increasing charge carrier recombination. This wide band gap material confines both charge carriers to the core in a type-I core/shell structure.[19] Ultrafast fluorescence upconversion spectroscopy showed adding a ZnSe shell passivated the dangling bonds on a CdSe core.[26] Measurements were made for CdSe cores of various sizes shelled with ZnSe and showed that as the size of the QD was increased, the amount of hole trapping also increased due to the band alignment of the core and shell materials. At larger sizes, there is a greater offset between core and shell, trapping the electron in the core while allowing the hole to reach surface traps.[26]

Further work has looked at alloying the core/shell interface to reduce this lattice strain and potentially provide more complete shell coverage.[31, 33, 53, 54] Graded alloy CdS_xSe_{1-x} QDs have a CdSe-rich core and then a graded interface to a CdS-rich shell and can be easily synthesized with a wide variety of ratios between sulfur and selenium. The CdS-rich shell serves as a wide bandgap material that helps to confine the charge carriers to the core and increase radiative recombination. These nanocrystals were characterized using ultrafast fluorescence upconversion spectroscopy to investigate how effectively this compositionally inhomogeneous nano-heterostructure can decouple the exciton from the nanocrystal surface. CdS_xSe_{1-x} QDs were synthesized with a wide variety of ratios between sulfur and selenium, and aliquots were taken throughout the synthesis. Increasing the S:Se ratio caused a slight blue shift in absorption as the samples show a greater extent of quantum confinement since a smaller selenium injection causes a smaller CdSe-rich core to form.

The charge carrier dynamics were evaluated and correlated to an increase in S:Se ratio. Increasing the ratio of sulfur: selenium essentially served to create a larger CdS-shell around the CdSe-core while maintaining roughly the same overall particle size. As the S:Se ratio was increased, the hole could be selectively confined to the core of the QD based upon the large offset of valence bands between CdSe and CdS. There is a complete elimination of the first decay component in the ultrafast fluorescence upconversion data for an increased S:Se ratio indicating complete confinement of the hole to the CdSe-rich core. The second component which correlates to electron trapping remains constant throughout the experiment because of the everchanging under-coordinated surface states. Since the conduction band offset is much smaller, the electron was unable to be fully decoupled in the investigated QDs.[34] The third exponential decay process represent radiative relaxation of the exciton. This component extends past the lifetime of the upconversion experiment. Both the amplitude and time of this component increase with an increase in S:Se ratio indicating less trapping which correlates with better surface passivation and more successful radiative recombination. Additionally, the graded interface is thought to reduce trap states seen between the core and shell of traditional core/shell QDs. Overall higher amplitude signal observed for these graded QDs shows the advantage of this alloyed structure.[34]

Ultrafast fluorescence upconversion spectroscopy has been used to show that both the addition of a co-surfactant, shelling, and alloying are effective ways at increasing radiative recombination in cadmium-based QD systems by passivating the QDs' surface. While trapping is yet to be completely eliminated in any structure, use of similar techniques that have been shown to be beneficial for these QDs systems will help with the development of other new QDs.

1.2.2 Transition Away from Cadmium-Based Nanomaterials

While CdSe-based QDs have been extensively synthesized and characterized for different compositions and morphologies, growing concerns over the toxicity of cadmium[55] have led towards increased research on other QD systems including InP, CIS, and ZnN_3.[22, 56-58] These systems still offer size tunable absorption and emission across the visible spectrum but remove the hazardous heavy metal cadmium. However, limited work on both synthesis and characterization of these QD systems has been carried out and therefore do not offer as robust a variety of structures and composition for various applications as what has been developed for CdSe-based QDs.

Perhaps the most well studied of these systems are InP QDs. InP QDs offer size tunable emission from the visible to the near infrared and lower intrinsic toxicity.[59-63] Despite the advantage of removing cadmium, multiple other challenges exist in this emerging system including large sample polydispersity, lack of stability when exposed to air, broad emission line widths, and low photoluminescence quantum yields (PLQYs).[22]

Unpassivated InP QDs show extremely low to no PL emission due to a highly defective QD surface—thought to be dominated by phosphorus dangling bonds.[64] To begin addressing these concerns with InP QDs, work is underway using many of the same techniques that were first tested for CdSe-based quantum dots. InP QDs have been shelled with ZnS and ZnSe. ZnS offers the advantage of having the wider band gap which should better confine the charge carriers; however, the lattice mismatch is larger (7%) so only a few layers of shelling material can be grown, and numerous defects are thought to be formed at the core/shell interface. On the other hand, ZnSe has a much smaller lattice mismatch and thick-shells have been grown, but the smaller band gap means that not all of the charge carriers may be able to be confined to the core. Alternatively, HF etching has been used to remove some of the surface ligands and shows an increase in PLQY and QD stability.

These new InP-based QD structures lack the thorough characterization and refinement which has been carried out for CdSe-based systems and thus research is needed to address these concerns and determine the best modes of surface passivation. More work is needed to be able to synthesize InP QDs with the ease and reproducibility of CdSe so that it can be more widely used.

1.3 OVERVIEW

This work looks at the role of the core/shell interface and its effect on QDs' photophysical properties. Chapter 2 discusses the experimental techniques used in the work covering both the steady state and ultrafast measurements. Chapter 3 covers work completed on using a different method of QD cleanup and its potential implications on surface ligands and passivation. Gel permeation chromatography was used as a method of purification for graded alloy CdS_xSe_{1-x} QDs with size separation being observed based upon elution time. Fractions were analyzed for shifts in their absorption and emission wavelengths along with changes in brightness and elemental composition. Chapter 4 discusses thick-shell InP/ZnSe QDs where it was observed for the first time that indium was being incorporated into the ZnSe shell. This chapter looks at the role the excess indium has on the ultrafast carrier dynamics of thick-shell InP/ZnSe QDs using ultrafast fluorescence upconversion spectroscopy. Chapter 5 reflects on this work and provides some thoughts on the issues with the InP QD system that will need to be addressed prior to their further implementation.

CHAPTER II

EXPERIMENTAL

2.1 SYNTHESIS

QDs can often be easily synthesized using a one-pot method whereby temperature and long-chained ligands are used to control the nucleation and growth to maintain their nano-size. QDs are typically synthesized in an inert atmosphere with careful control over the ratio and quantity of starting materials to obtain nanocrystals with the desired structure and composition. The selection of the proper surface ligands is important not only to maintain the nano-sized products, but also to optimize the photophysical properties of the NCs as discussed in chapter 1. Shelling can either take place as a separate discrete step in the synthetic process or by controlling the precursor's reactivity.

2.1.1 CdS_xSe_{1-x} QDs

Graded alloy CdS_xSe_{1-x} QDs were synthesized following a literature method reported by Harrison *et al.*[33] and modified by Keene *et al*.[34] using a one-pot method relying on a difference in reactivity between the sulfur and selenium precursors. In a 100mL three neck flask, 40 mL 1-octadecene (ODE) was combined with 2.56 mL oleic acid and 0.256 g cadmium oxide (CdO). The reaction was purged under argon while heating to 150°C with vigorous stirring to remove oxygen and water from the reaction flask. The solution was continuously heated and stirred to 300°C until solution was clear and colorless. A solution of 1.12 mL 0.75M solution S:TBP/ODE and 0.48 mL 0.75M solution Se:TBP/ODE was swiftly injected to synthesize QDs with initial S:Se ratio of 7:3.

Following growth at 260ºC for 2 hours, the reaction flask was cooled with compressed air to <90°C. The QDs were separated into six centrifuge tubes and a mixture of 3:2 butanol:ethanol was added, and the mixture centrifuged for 5 minutes at 7500 rpm. After the initial centrifugation step, two different methods were then used to remove unreacted synthetic precursors and purify the as-synthesized QDs and are discussed in chapter 3.

2.1.2 Thick-Shell InP/ZnSe QDs

A thick-shell of wide band gap ZnSe was grown on InP cores to passivate the surface of InP QDs using discrete steps of synthesizing the InP cores followed by a continuous-injection shell growth process.[65] To synthesize the InP cores, 160 mg indium myristate was dissolved in 5 mL octadecene. This solution was degassed at 100ºC then heated to 300ºC. A solution of 45 uL of 0.15 mmol of tris(trimethylsiyl)phosphine ($(TMS)_3P$) in 1 mL trioctylphosphine (TOP) was quickly injected and the nanocrystals were grown at 300ºC for 30 min. After the core synthesis, 50 mg zinc myristate in 3 mL of trioctylamine was added and the mixture was then degassed again at 100ºC. To facilitate thick-shell growth, 6 mL of 0.4 M zinc oleate and 6 mL of 0.4 M TOP-Se was added dropwise at 1.5 mL/hour. The QDs were then annealed at 300°C for 2 hours. After synthesis, the QDs were washed three times using isopropyl alcohol with a small quantity of acetonitrile added to cause the QDs to flocculate. The mixture was centrifuged for 10 minutes at 7000 rpm. The QDs were dissolved in toluene for further analysis.

2.2 CHARACTERIZATION

Thorough characterization of QDs looks at their photophysical properties, size, shape and elemental composition/structure. Absorption and emission measurements provide information about QD size, brightness, and color. Transmission electron microscopy and energy dispersive x-ray spectroscopy allow the structure and composition of the QDs to be determined. This section addresses how these measurements are taken for QD samples.

2.2.1 Static Optical Absorption and Emission

All synthesized QDs are initially characterized using static optical absorption and photoluminescence to determine the band gap and emission wavelength. For many of the early more well studied QD systems such as CdSe, sizing curves have been developed that allow for the size of the nanocrystals to be determined just from the absorption data.[66] Additionally, the sample's optical density determines how much light is being absorbed by the QDs at a specific wavelength. Absorption spectra were obtained using a Varian Cary 50 UV-Vis spectrophotometer and photoluminescence spectra were obtained with an ISS PC1 Photon Counting Spectrofluorimeter or a Photon Technology International QuantaMaster 40.

2.2.2 Photoluminescence Quantum Yield

Photoluminescence quantum yield (PLQY) is a measurement of how bright QDs are. Higher PLQYs generally mean more efficient radiative recombination of charge carriers. Specifically, PLQY measures a ratio of photons absorbed by the QD to photons emitted:

$$PLQY = \frac{\#\, photons\ emitted}{\#\, photons\ absorbed}\ x\ 100\ \% \qquad (2.1)$$

Measurements were taken using the single point calibration method using a laser dye (typically rhodamine 6G or sulforhodamine B) which have a known PLQY. The absorbance of both the QDs and reference dye were obtained at the excitation wavelength using a Varian Cary 50 UV-Vis spectrophotometer to ensure both had an optical density between 0.09 and 0.1. Their fluorescence was then obtained with a Photon Technology International QuantaMaster 40 and the area under the curve summed. The QD sample's PLQY is then determined using equation 2.2:

$$PLQY = Q_R \frac{I}{I_R} \frac{QD_R}{QD} \frac{n^2}{n_R^2} \qquad (2.2)$$

the subscript R denotes values for the reference dye, I is the integrated fluorescence intensity, OD is the optical density or absorbance of the sample at the excitation wavelength, and n is the refractive index of the solvent.[67]

2.2.3 Transmission Electron Microscopy and Energy Dispersive X-ray Spectroscopy

Transmission electron microscopy (TEM), energy dispersive spectroscopy (EDS), and scanning-TEM-EDS (STEM-EDS) were also used to characterize QD samples. TEM allows the sizes of the QDs to be determine and provides valuable information about their structure. EDS looks at the x-rays that are given off by the QDs after their interaction with electrons in the TEM and allows for elemental composition to be determined. A FEI Tecnai Osiris S/TEM electron microscope equipped with ChemiSTEM™ technology was used to perform STEM-EDS, which allows for elemental mapping of QDs on the nanoscale. Size was analyzed using ImageJ and EDS spectra were analyzed using FEI TIA offline image analysis software.

2.3 FEMTOSECOND FLUORESCENCE UPCONVERSION SPECTROSCOPY

2.3.1 The Upconversion Technique

As previously mentioned, femtosecond fluorescence upconversion spectroscopy allows direct measurement of the excited state of a QD sample and probing of the ultrafast charge carrier dynamics on the picosecond timescale without interference from other processes. The reduction in radiative recombination is measured, and the rate and extent of decay can be compared to determine which processes are occurring in a QD sample. This optical gating technique relies on the combination of the QDs' fluorescence with a gate beam in a sum frequency generation process:

$$\omega_{sum} = \omega_{fluorescence} + \omega_{gate} \qquad (2.3)$$

Samples' fluorescence is probed for 10 picoseconds prior to excitation and 100 picoseconds after excitation to measure the time it takes for the QD sample to begin emitting, the hole trapping constant, the electron trapping constant, and to provide further information about the long-lived radiative recombination. As discussed extensively in section 1.2, these times are compared across various different particle morphologies to determine which is most effective at passivating the surface of the QD. The technique requires two pulses (excitation and gate) that are perfectly overlapped in time and space in a $LiIO_3$ nonlinear mixing crystal to generate a sum frequency signal:

$$\frac{1}{\lambda_{upconverted}} = \frac{1}{\lambda_{fluorescence}} + \frac{1}{\lambda_{gate}} \qquad (2.4)$$

2.3.2 Ultrafast Laser System and Experimental Setup

The ultrafast laser setup has been described previously.[34, 35, 43] The Coherent Verdi V-18 is a diode pumped Nd:YAG laser that generates 18 W of 532 nm CW light. This signal pumps a mode-locked titanium:sapphire (Ti:sapph) oscillator (Mira 900 basic, Coherent) that operates at 76 MHz and has 17 nJ of energy per pulse. These pulses seed a regenerative amplifier (RegA 9000, Coherent) that amplifies the beam to 5μJ per pulse at 250 kHz to provide sufficient energy to power the optical parametric amplifier (OPA 9400). The OPA's seed pulse is split and 25% generates a white light continuum using whole beam self-focusing in a sapphire crystal. The remaining 75% travels to a BBO crystal where the second harmonic is generated to parametrically amplify the signal wavelength. Additionally, the OPA generates three other pulses: idler, residual pump (800 nm), and residual second harmonic (400 nm). The final signal pulse obtained from the OPA is wavelength tunable from 450-700 nm, while the idler similarly tunes from 930-2300 nm. The residual pump is used as the gate beam for the upconversion experiment discussed later. The system operates at 250 kHz and yields instrument response functions (IRFs) <200 fs. RegA and OPA pulses are measured using frequency resolved optical gating (FROG).[68]

Ultrafast fluorescence upconversion spectroscopy involves optical gating using two laser pulses: gate and excitation. The excitation pulse is wavelength tuned to match the wavelength at which the QD sample absorbs light. In the case of the thick-shell InP/ZnSe QDs, samples are excited at 490 nm to ensure higher enough absorption of laser pulses while preventing excitation of the QD shell. Residual 800 nm not frequency doubled in the OPA serves as the gate pulse. The excitation beam reflects off of a delay stage which allows for its arrival time to be altered and thus to probe the carrier dynamics over the course of time. Time resolution for the upconversion experiment is obtained by directly overlapping the pump and gate pulse spatially and temporally in the non-linear mixing crystal (1 mm XC8-LiIO$_3$-Type-I SFM-800/500-1000//308-44 nm, Cleveland Crystals, Inc.). A gaussian beam overlap is observed and the FWHM is recorded and used in the data fitting talked about below. A graph of a typical instrument response function (IRF) is seen in Figure 2.1.

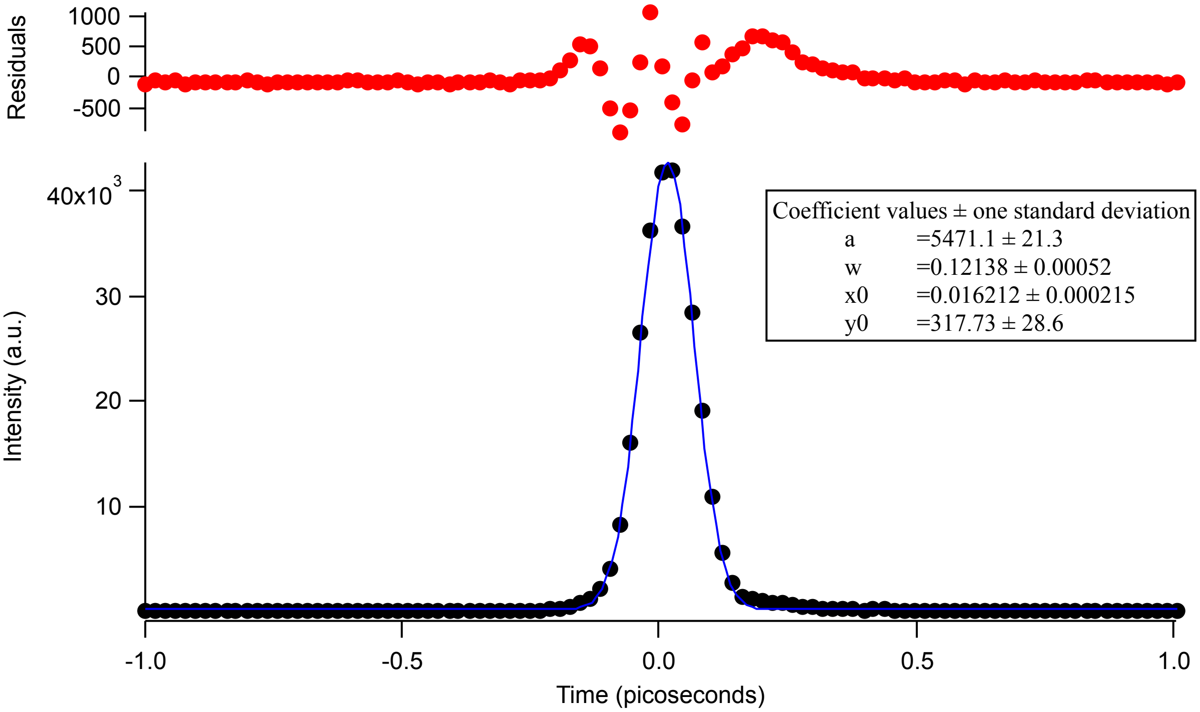

Figure 2.1. Typical instrument response function with gaussian fit and residuals, which provides the time resolution of the experiment, in this case FWHM = 121.4 fs.

After obtaining an IRF, fluorescence from a laser dye selected to match wavelengths with the QDs' emission is focused using a rhodium coated elliptical reflector onto the non-linear mixing crystal where it is overlapped with the gate pulse to form upconverted signal. A UV-dispersing prism (STS#37261, CVI Laser Corp.) separates upconverted signal from residual photons. Upconverted signal is directed into a UV-optimized monochromator (McPherson), detected by a photomultiplier tube (Hamatsu R1527P), and recorded digitally by a photon counter (SR400, Stanford Research Systems). Then, QDs are placed into the 2 mm cuvette under an argon atmosphere, which is constantly stirred while under laser excitation, and the QDs' fluorescence is focused onto the non-linear mixing crystal. A thick-shell InP/ZnSe QD under laser excitation in the upconversion experiment can be seen in Figure 2.2.

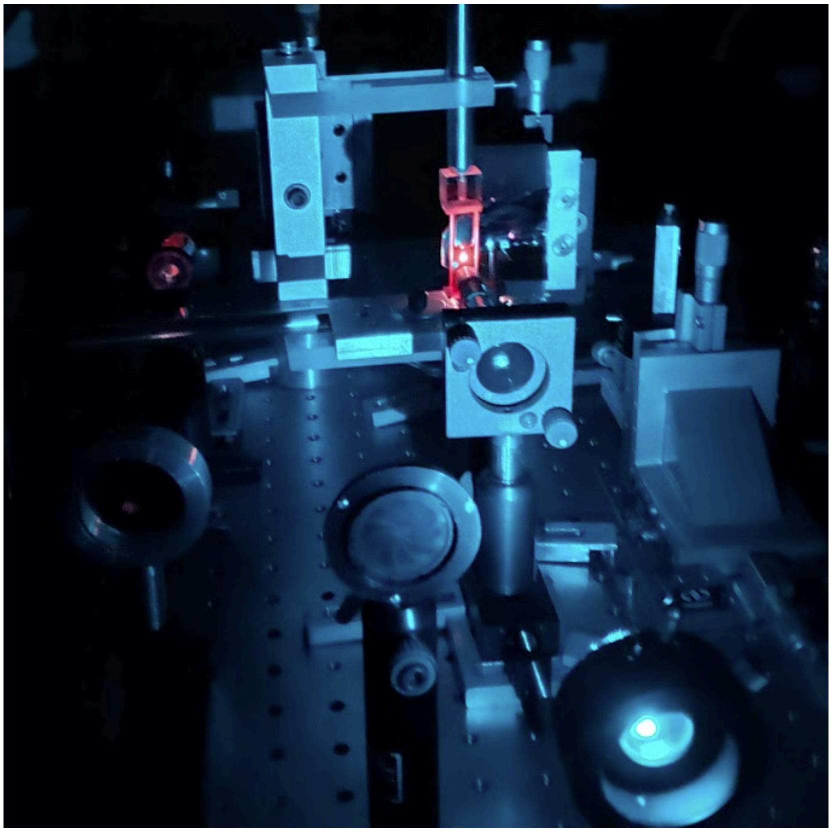

Figure 2.2. Thick-shell InP/ZnSe QD sample under laser excitation in the ultrafast fluorescence upconversion experimental setup.

After moving a set distance, the photons are summed for a period of one second prior to the stage advancing to the next position to delay or accelerate the arrival of the laser pulse to the experiment, which allows for times from -10 picoseconds to 100 picoseconds to be probed. This time range encompasses hot carrier cooling, hole trapping, and electron trapping. Radiative recombination extends beyond the lifetime of this experiment but can be probed using techniques such as time-correlated single photon counting. A complete layout of the ultrafast laser setup can be seen in Figure 2.3.

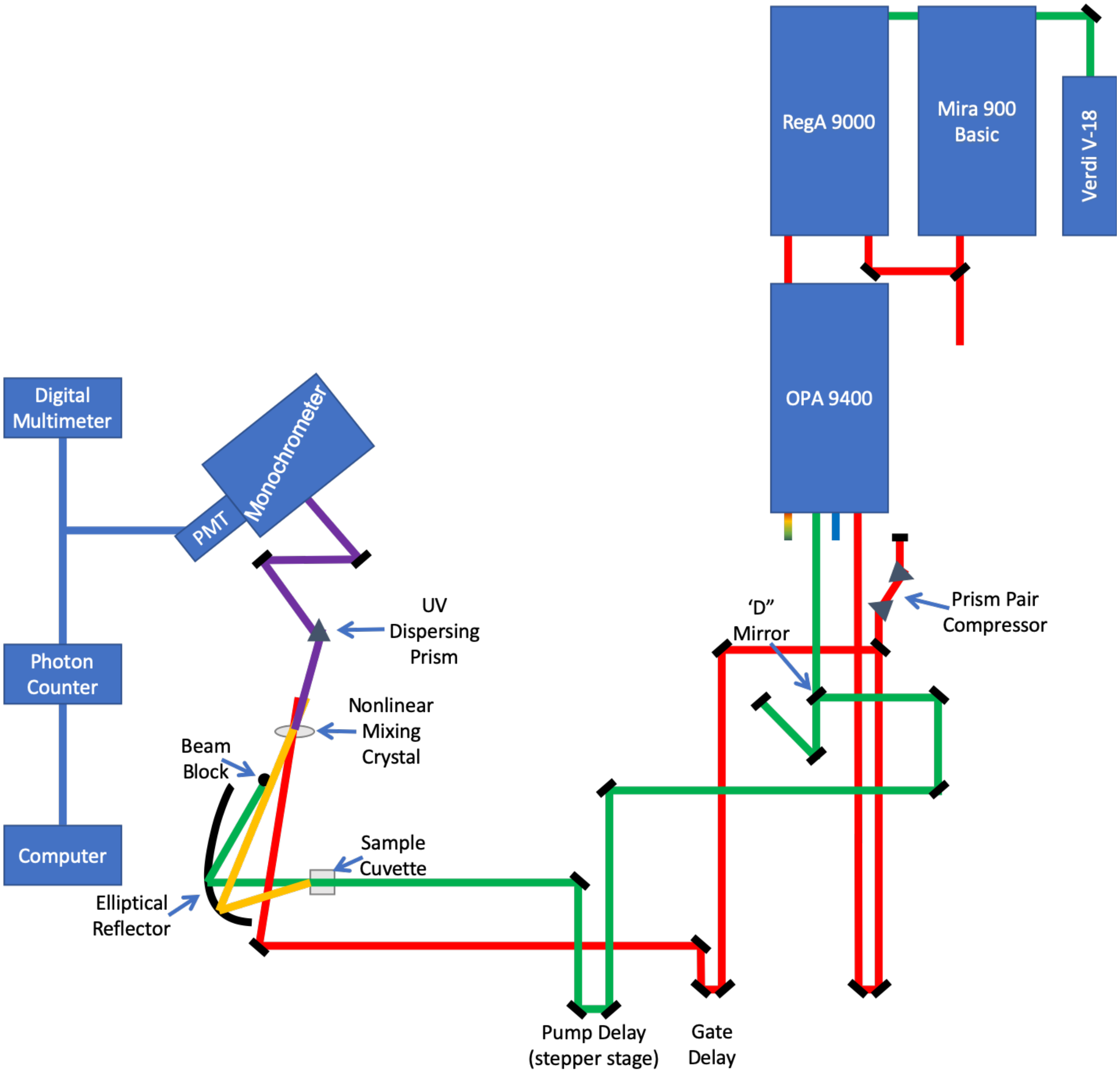

Figure 2.3. Ultrafast laser setup showing the femtosecond fluorescence upconversion setup. Wavelength tuned pulses of approximentally 200 fs are generated by the Verdi, Mira, RegA, and OPA. The pump beam excites the QD sample inside of a cuvette while the gate beam provides the timing of the experiment. Samples' fluoresence is focused using a rhodium-coated elliptical reflector onto a nonlinear mixing crystal where the two signals are overlapped. Signal is recorded with a photomultiplier tube and digitized with a photon counter.

2.3.3 Sample Considerations

While the transition from a flow cell to a small volume cuvette has allowed for analysis of smaller quantities of material, several factors need to be considered to obtain sufficient decay data. At the most basic level, the sample needs to exhibit stability under laser excitation for several hours. InP QDs often readily oxidize upon exposure to air and excitation by laser beam causes increased photo-oxidation. Care must be taken during the QD cleanup process to ensure that the sample is not exposed to oxygen or solvents that can degrade the synthesized dots while also ensuring that all impurities have been removed that could lead to scattering during the ultrafast experiment.

Reducing the exposure of the QD sample to oxygen prior to analysis and ensuring that the excess surface ligands and unreacted precursors are removed from the synthesized particles has taken a stepwise process. The initial synthetic cleanup was a simple phase exchange, which did little to remove unreacted precursors and caused the sample to separate into phases upon laser excitation. Gel permeation chromatography (GPC, further discussed in the next chapter) has provided cleaner QDs with limited oxidation when the procedure is carried out inside of a glovebox filled with nitrogen. However, substantial challenges with carrying out GPC inside of the glove box led back to a precipitation/redissolution method where isopropyl alcohol with a small quantity of acetonitrile was used. The sample is then stored inside of a glove box with limited amounts removed as necessary inside of a sealed cuvette for analysis. Concerns over oxidation and aggregation of InP/ZnSe samples led to the QD cleanup taking place in the glove box on the same day as analysis with very minimal exposure to air to transfer the sample from the vial to the cuvette used for analysis. Additionally, samples with too thin a shell of ZnSe rapidly photodegraded and were unable to be analyzed.

2.3.4 Data Analysis

The ultrafast fluorescence upconversion spectra are fit using Equation 2.7, a convolution of the Gaussian instrument response function $\left(f(W,t)\right)$ centered at t=0 with a full-width at half-maximum (FWHM) of W with several exponential decays $\left(g(A,\tau,t)\right)$ with decay lifetime τ and pre-exponential factor A.[69] The number of exponential decays varies as needed to represent the decay pathways in the specific QD sample analyzed (in this case, n=4).[35] A time shift (t_0) and offset (y_0) allow the function to decay to baseline instead of 0. A_i represents the *i*th decay amplitude and τ_i is its corresponding decay time; W is the fwhm of the Gaussian instrument response function (IRF).

$$f(W,t) = \left(\frac{2\sqrt{\ln 2}}{W\sqrt{\pi}}\right) exp\left[-4t^2\frac{\ln 2}{W^2}\right] \qquad (2.5)$$

$$g(A,\tau,t) = Aexp\left(\frac{-t}{\tau}\right) \qquad (2.6)$$

$$Fit = \sum_{i=0}^{n}\left[\frac{A_i}{2}\left(1+erf\left[\left(\frac{1}{4}\right)\frac{8(t-t_0)(\ln 2)-W^2/\tau_i}{W\sqrt{\ln 2}}\right]\right)\exp\left[\frac{-\left(16(t-t_0)(\ln 2)/\tau_i\right)-W^2/\tau_i^{\,2}}{16\ln 2}\right]\right]+y0 \qquad (2.7)$$

The data were fitted *via* a custom procedure in Igor Pro, which utilizes the Levenberg-Marquardt algorithm (LMA) to search for the coefficient values that minimize chi-square and estimates the standard deviation of the fit coefficients.

Interference from the optical parametric amplifier causes some upconverted signal to be recorded prior to the observed fluorescence decay. Since the OPA selectively amplifies one wavelength of light, the residual white light continuum still contains the monitored wavelength and this signal was also upconverted and recorded. This signal is masked during data fitting as a well-established baseline occurs on both sides on this peak as seen in Figure 2.4.

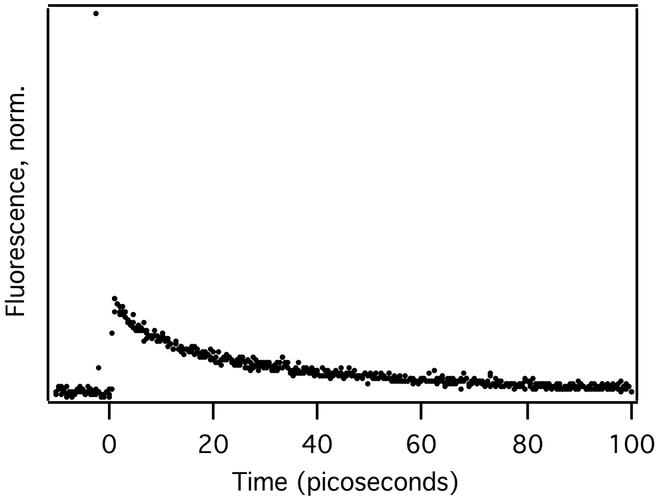

Figure 2.4. Complete ultrafast decay curve of thick-shell InP/ZnSe QDs showing interference from IRF before the arrival of decay signal

CHAPTER III

COLUMN CHROMOTOGRAPHY AS A METHOD OF SIZE SELECTIVE SEPARATION

This chapter describes efforts to utilize graded alloy CdS_xSe_{1-x} QDs and gel permeation chromatography (GPC) to evaluate the role that GPC can serve in size selective QD precipitation. Understanding the way that an alternative cleanup procedure affects the properties of this well-studied QD system will help to shape the way that this technique is used on emerging QD systems. Since the properties of these graded alloy QDs have been extensively studied, the knowledge obtained about how changes in size, shape, and shell coverage alter photophysical properties can help to refine further InP/ZnSe syntheses.

3.1 GRADED ALLOY CdS_xSe_{1-x} QDs

As discussed earlier, graded alloy CdS_xSe_{1-x} QDs that contain a CdSe-rich core and a CdS-rich shell were synthesized in an attempt to optimize the core/shell interface and improve the photophysical properties of CdSe/CdS core/shell structures. A gradual transition from core to shell material relaxes the confinement potential at the interface and alters the band structure. The alloyed structure also helps to form complete shell coverage around the core rather than preferential addition at certain facets that leads to incomplete surface passivation.[34]

These QDs can be easily synthesized with a wide variety of ratios of sulfur to selenium which lead to different amounts of surface passivation.[33] The synthesis is completed in one-pot with a single injection and relies on the difference in reactivity between Se:tributylphosphine

(TBP) and S:TBP to form a graded interface. Since Se:TBP reacts more quickly, it is incorporated into the core while the stronger bonded S:TBP takes longer to react and thus forms the shell of the QD. However, the resulting nanocrystals often have a large size distribution and heterogenous shapes, which leads to different photophysical properties for QDs synthesized in the same batch.[70] The composition and structure of these graded QDs can be seen in Figure 3.1. All QDs show some extent of surface passivation with a CdS shell, but not all QDs show the same amount of shell coverage.

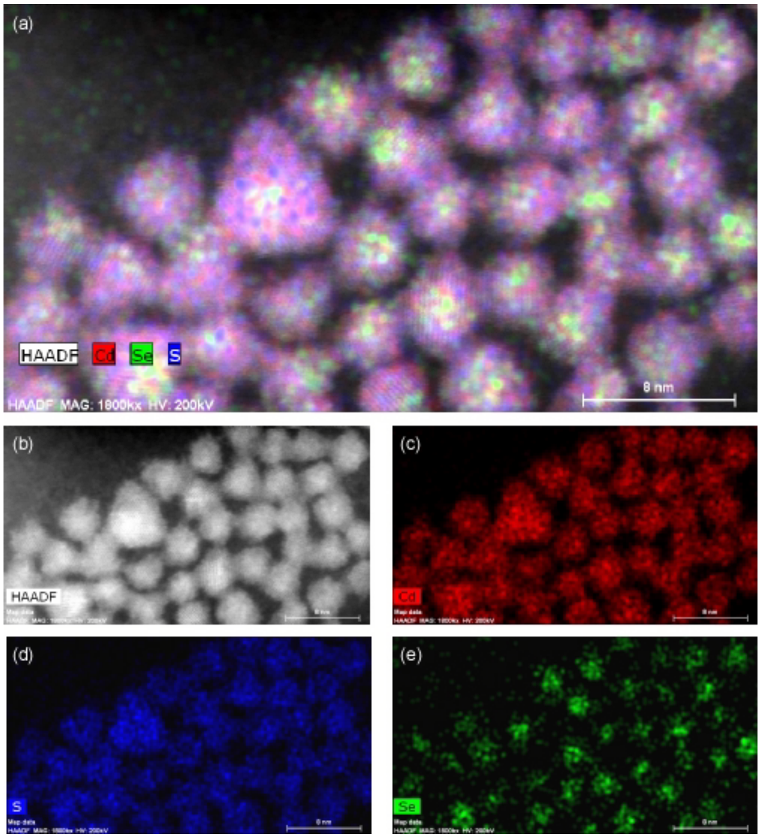

Figure 3.1. STEM and EDS maps of graded alloy CdS_xSe_{1-x} QDs showing a CdSe-rich core and CdS-rich shell. Reprinted with permission from Keene, J. D.; McBride, J. R.; Orfield, N. J.; Rosenthal, S. J., Elimination of Hole–Surface Overlap in Graded CdS_xSe_{1-x} Nanocrystals Revealed by Ultrafast Fluorescence Upconversion Spectroscopy. *ACS Nano* **2014,** *8* (10), 10665-10673. Copyright 2014 American Chemical Society.

Here, column chromatography was used to size selectively separate these CdS_xSe_{1-x} QDs with the goal of evaluating the difference in carrier dynamics for QDs with a thicker-shell of CdS. Since the photophysical properties of QDs in the same batch can differ based upon their composition and structure,[71, 72] a desire exists to evaluate the properties of each subpopulation. QDs with a thicker shell should further help to decouple the excitons from the surface of the QD, and thus hopefully reduce electron trapping as well. By controlling which size and shape of QDs are being analyzed, the population of dots that will be better for various applications can be determined.

3.1.1 Traditional Nanoparticle Sample Cleanup

As-synthesized colloidal QDs have unreacted precursors, reaction byproducts, high boiling point solvents, and excess ligands added to control growth and improve stability.[73] Prior to use these excess materials need to be removed and the QDs purified. Traditionally this purification has taken place using a precipitation and redissolution process whereby the QDs are dissolved in an appropriate solvent and then flocculated using an antisolvent to increase the polarity of the solvent mixture. The QDs are centrifuged out of solution and the soluble impurities are decantated away. For these graded alloy CdS_xSe_{1-x} QDs, this typically involved an initial centrifugation step where the synthesized QDs were centrifuged with a 3:2 butanol:ethanol solution. The QDs were then resuspended in minimal toluene and enough ethanol was added to cause the QDs to precipitate. Samples were centrifuged an additional three times using these toluene/ethanol washes.

While this method is convenient and easily scalable for many QDs systems, it can also inadvertently remove surface ligands from the surface of the QD which can harm the photophysical properties of the synthesized QDs.[73] Therefore, other techniques are being evaluated that are less harsh on the surface of the QD, and that might involve less excess solvent making it more environmentally friendly.

3.2 COLUMN CHROMOTOGRAPHY

Recently, GPC has been introduced as a highly precise and effective method of QD purification.[73] This method relies on size exclusion to remove impurities from the synthesized QDs instead of solubility. GPC offers several advantages over traditional precipitation and redissolution techniques. This method removes fewer surface ligands from the synthesized particles than traditional sequential precipitation and redissolution methods, yet still yields pure nanocrystals. Additionally, it removes impurities which are soluble in the solvent used during redissolution and shows greater batch-to-batch repeatability.[73]

3.2.1 Technique

To perform GPC, QDs were passed through a column with styrene-divinylbenzene copolymer. These polymer beads trap unreacted precursors in their pores and the cleaned nanocrystals exit the column. In this case, to prepare the column for use in purification, 4 g of styrene-divinylbenzene copolymer (200-400 mesh particle size, 2% cross-linked) were swelled in toluene overnight. These beads were then placed into the column and toluene was run across the beads until no free polystyrene was observed. QDs were prepared for GPC by completing one precipitation and redissolution using appropriate solvents. These QDs were then suspended in toluene and then allowed to flow across the beads as can be seen in Figure 3.2.[73] QDs were collected in several fractions to observe if there were any changes in the QDs' properties between those the eluted more quickly and those that had a longer retention time. Additionally, comparisons were made between QDs that passed through the column and those that were cleaned with a more traditional precipitation and redissolution method to see the role of the column cleanup on the QDs' properties.

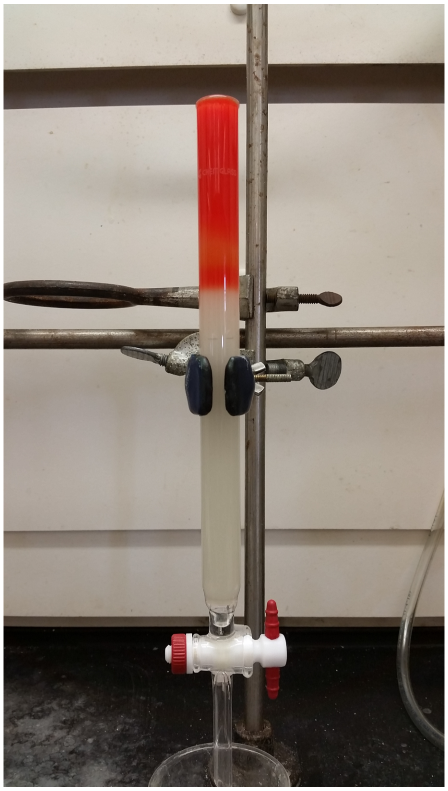

Figure 3.2. CdS_xSe_{1-x} QDs in a column with styrene-divinylbenzene copolymer. The large QDs flow through the column while the small unreacted precursors get trapped in the pores on the beads.

3.3 SIZE SELECTIVE QD ENGINEERING OF CdS_xSe_{1-x} NANOPARTICLES

The QDs that passed through the column were initially separated into five equally sized fractions based upon volume eluted out of the column, and each fraction's absorption, emission, and PLQY were determined. Several fractions were also analyzed with TEM and STEM-EDS to look at the change in size and elemental composition. Interestingly, size-separation of these QDs was observed when using GPC. These results are summarized in Table 3.1.

3.3.1 Optical Characterization

Absorbance measurements, fluorescence measurements, and PLQY were acquired for precipitated QDs and the various eluted fractions (Figure 3.3). Little change in wavelength and brightness was observed for the first three fractions eluted from the GPC column indicating that a large portion of the synthesized QDs share similar properties. Once the fourth fraction was eluted, however, a small redshift was seen in both the absorption and emission wavelengths indicating that larger QDs were being eluted. An even greater redshift was seen with QDs eluted in the fifth and final fraction again indicating a further size increase in eluted QDs since the smaller band gap correlates with an increase in nanoparticle size and an increase in the density of states.

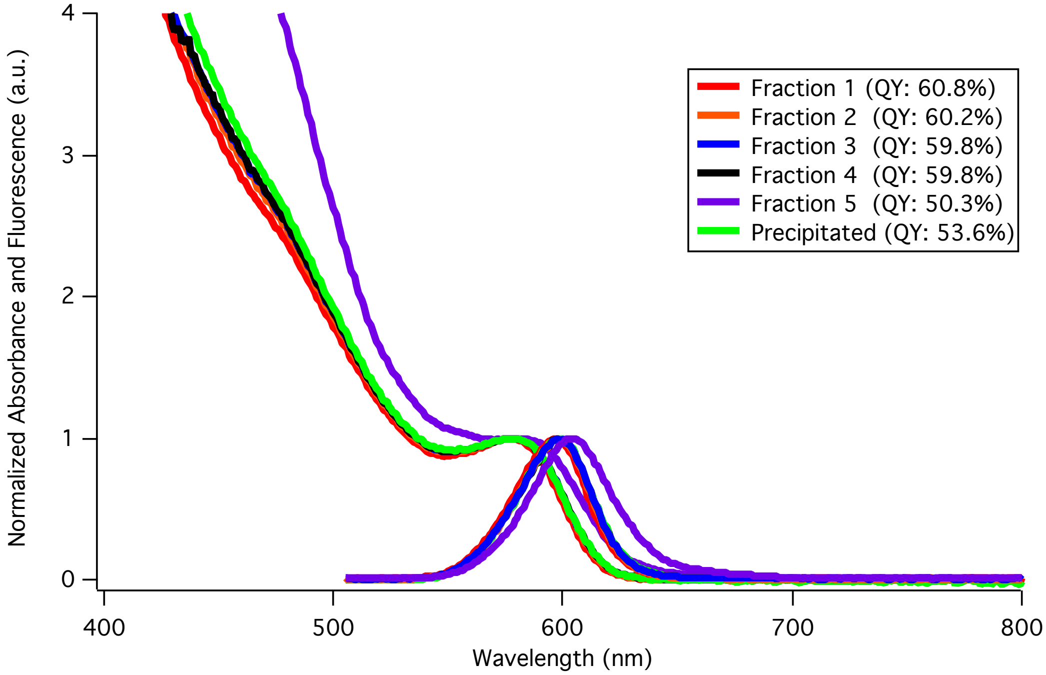

Figure 3.3. Absorption and emission of graded alloy CdS_xSe_{1-x} QDs for various eluted fractions after column chromatography. Larger dots with more red absorption and emission are found in the later fractions.

The precipitated QDs showed an absorption and emission in between that of the early and late fractions, which would be expected as it is a measurement of the average properties for the entire sample. Its absorption and emission wavelength are redshifted from the first four fractions which indicates that the large nanocrystals are influencing the overall ensemble properties, but not to any great extent as the precipitates QDs fall much closer to the first fraction than the last fraction.

Using the taken absorption and emission measurements, PLQY was determined for the precipitated sample and all five individual fractions. The ensemble PLQY of the QDs that were precipitated out of solution was 53.6%, which falls in between the percentages observed for fractions 1-4 and fraction 5. The earliest fractions show a higher QY (~60%) than the last fraction (50.3%), which seems to indicate that the different size QDs have different photophysical properties beyond just the wavelengths of absorption and emission.

The full-width half-maximum (FWHM) of the fluorescence signal also provides evidence about the size distribution of the eluted QDs. A larger FWHM indicates a larger size distribution since for quantum confined nanocrystals, the emission wavelength changes as the size of the QD changes. Again, the FWHM was very similar (39.0-39.5 nm) for the first three eluted fractions meaning that the size of all those QDs were similar. The fourth and fifth fractions increased up to 44.8 nm, while the precipitated QDs again had a FWHM between the first and last fractions. Reducing the FWHM would also help improve the size selectivity of the various QD fractions.

3.3.2 TEM and STEM-EDS Characterization

TEM and STEM-EDS was performed on fractions 1, 4, and 5 in addition to the precipitated nanocrystals. Fractions 2 and 3 were not analyzed since they shared very similar optical properties to fraction 1 and thus would be expected to share similar sizes and elemental compositions. As previously mentioned, using a traditional precipitation and redissolution method of cleaning graded alloy CdS_xSe_{1-x} QDs causes a wide distribution of sizes and shapes as can be seen in the TEM image Figure 3.4. The average size of these nanocrystals was 4.42 ± 0.90 nm. It is also clear that the larger particles compose a small fraction of overall synthesis.

For those nanocrystals cleaned using GPC, those that eluted from the column initially had a smaller size and lower standard deviation than those than eluted in later fractions moving from 4.28 ± 0.80 nm in the initial fraction to 5.38 ± 1.94 nm in the final fraction. This size distribution can be seen in TEM images Figure 3.5. Fraction 5 appeared to have to distinct subpopulations with different average sizes: one centered at 4.07 nm and a second peak centered at 5.78 nm indicating that even with separation into 5 fractions all of the smallest particles were not being removed, and thus that less than 20% of the particles were receiving this thick-shell coverage. A histogram summarizing the change in size distribution with elution fraction is shown in Figure 3.6.

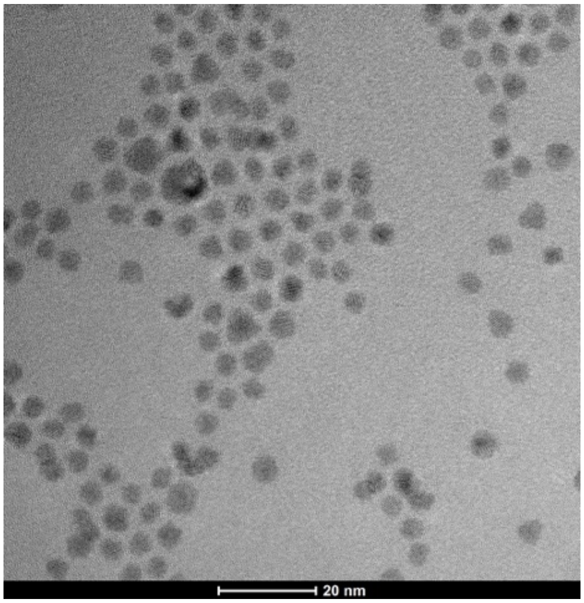

Figure 3.4. TEM of precipitated graded alloy CdS_xSe_{1-x} QDs showing large polydispersity in QD sizes.

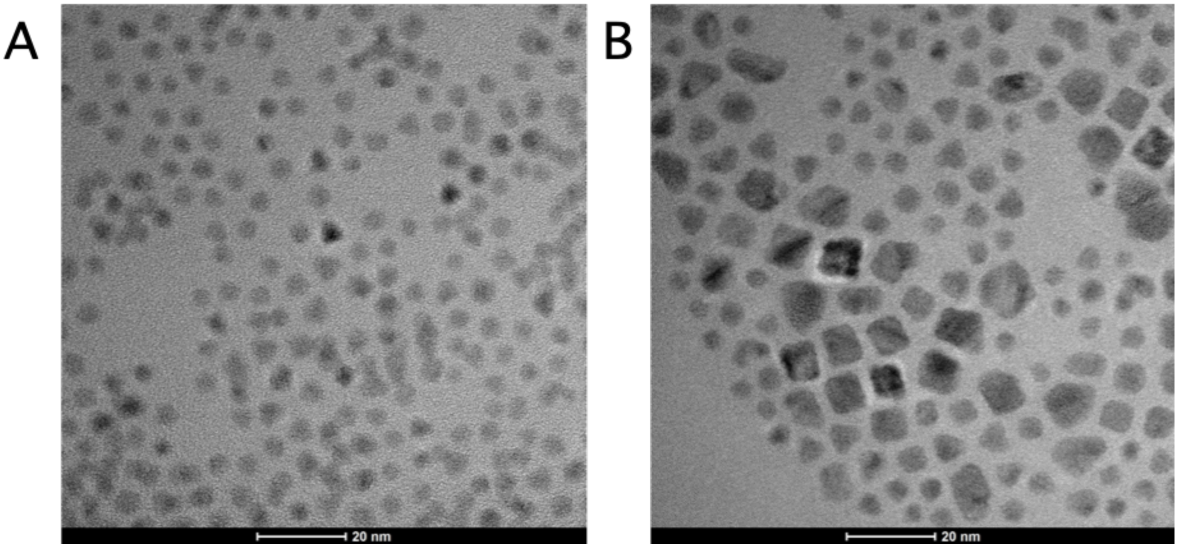

Figure 3.5. TEM images of graded alloy CdS_xSe_{1-x} QDs showing a clear difference in average size of QD between the first eluted fraction (A) and the last (B).

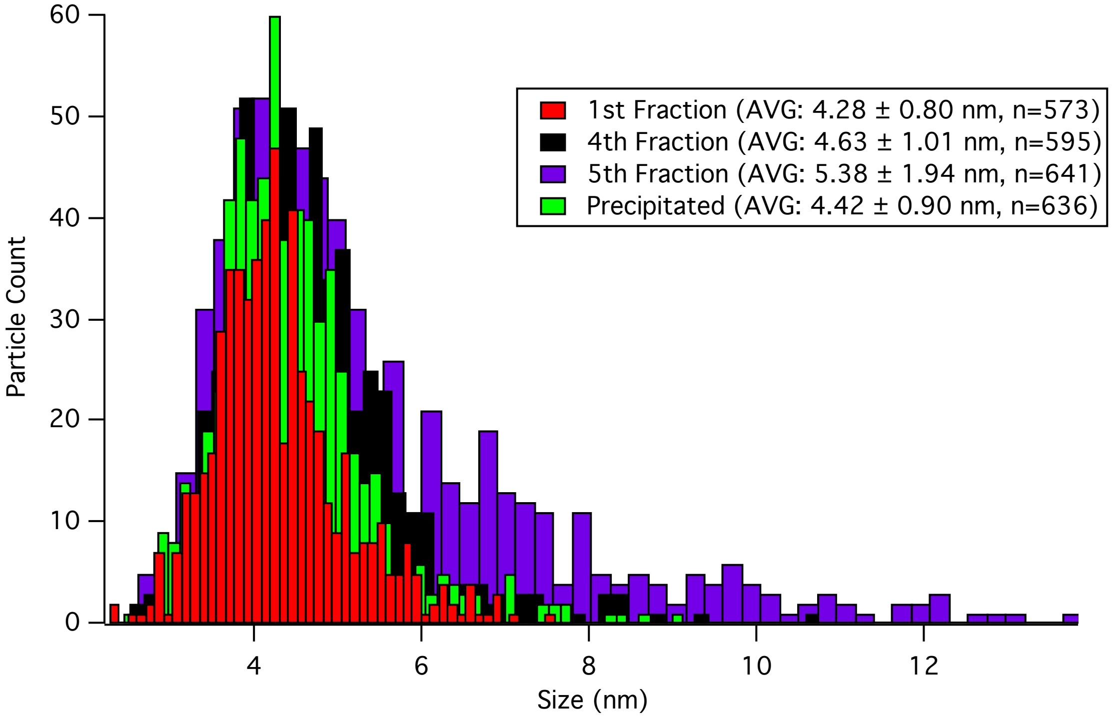

Figure 3.6. Histogram of sizes of CdS_xSe_{1-x} QDs from TEM showing the change in average particle size for various elution fractions.

To investigate the elemental composition and location, TEM-EDS and STEM-EDS mapping was used to look at the composition of cadmium, sulfur, and selenium in the various fractions. As is expected additional sulfur was seen for those QDs eluted in later fractions since the larger size meant more shell growth. Sulfur composed 29.4 % of the QD in the first fraction which increased to 36.9 % and was correlated with a drop in selenium percentage from 17.7 to 8.9. The elemental composition of these NCs can be seen in Figure 3.7 where the core is CdSe and the large NCs have a thick-shell of CdS that helps to further passivate the surface of the CdSe cores. Again, the precipitated NCs fell in-between that of the first and last fractions but was much closer to the initial elusion fraction again indicating that these larger QDs with more shell make up a small population of the overall synthesis that can be amplified by GPC.

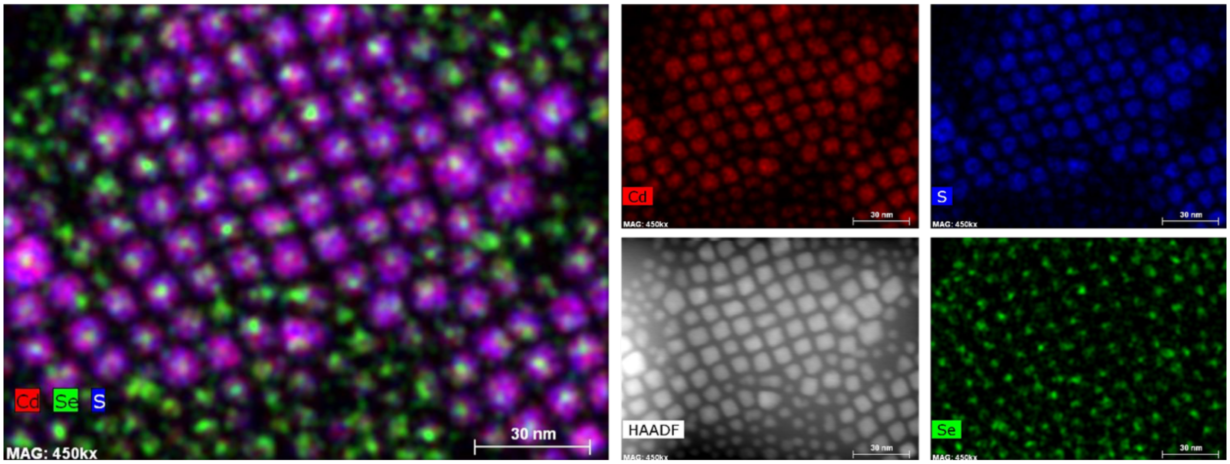

Figure 3.7. STEM-EDS image of fifth fraction graded alloy CdS_xSe_{1-x} QDs showing additional sulfur incorporation into large QDs.

Table 3.1 Summary of properties for various eluted fractions of graded alloy CdS_xSe_{1-x} QDs

	1st Fraction	2nd Fraction	3rd Fraction	4th Fraction	5th Fraction	Precipitated
Quantum Yield (%)	60.8	60.2	59.8	59.8	50.3	53.6
Absorbance Peak (nm)	578	578	578	579	581	579
Fluorescence Peak (nm)	594.4	595.9	596.1	596.3	603.7	596.2
Fluorescence FWHM	39	39.2	39.5	39.6	44.8	39.9
Average Size ± Standard Deviation (nm)	4.28 ± 0.80			4.63 ± 1.01	5.38 ± 1.94	4.42 ± 0.90
Cd Atomic %	52.91			53.42	54.28	53.82
Se Atomic %	17.66			15.44	8.86	16.27
S Atomic %	29.44			31.13	36.86	29.91

3.4 FURTHER REFINEMENTS OF SIZE SELECTIVITY

As the fifth fraction of eluted QDs still showed a substantial portion of smaller QDs and two size distributions in the TEM data, smaller fractions were eluted to determine if these smaller fractions would have QDs of more uniform size. Therefore, an additional synthesis was performed and the CdS_xSe_{1-x} QDs were passed through a new column for purification and then separated into 11 individual fractions. Absorption, emission, and QY were determined for the smaller fractions (Figure 3.8, Table 3.2), and show a similar redshift in absorption and emission between the earlier and later elution fractions as was seen for fewer fractions. Additionally, this redshift was able to be increased, indicating better size separation. With 11 fractions, the emission is redshifted from 594 nm to 611 nm indicating that the later fractions have an even more substantial presence of large-sized QDs that have a thick-shell of CdS that should be more efficient at passivating the surface of the QDs. Interestingly, while the QY decreases between fractions 1 and 9, it again increases with the 11th fraction which might indicate better surface passivation for those large QDs with a thick-shell. However, the quantity of QDs eluted in this fraction was not substantial enough to perform ultrafast spectroscopy.

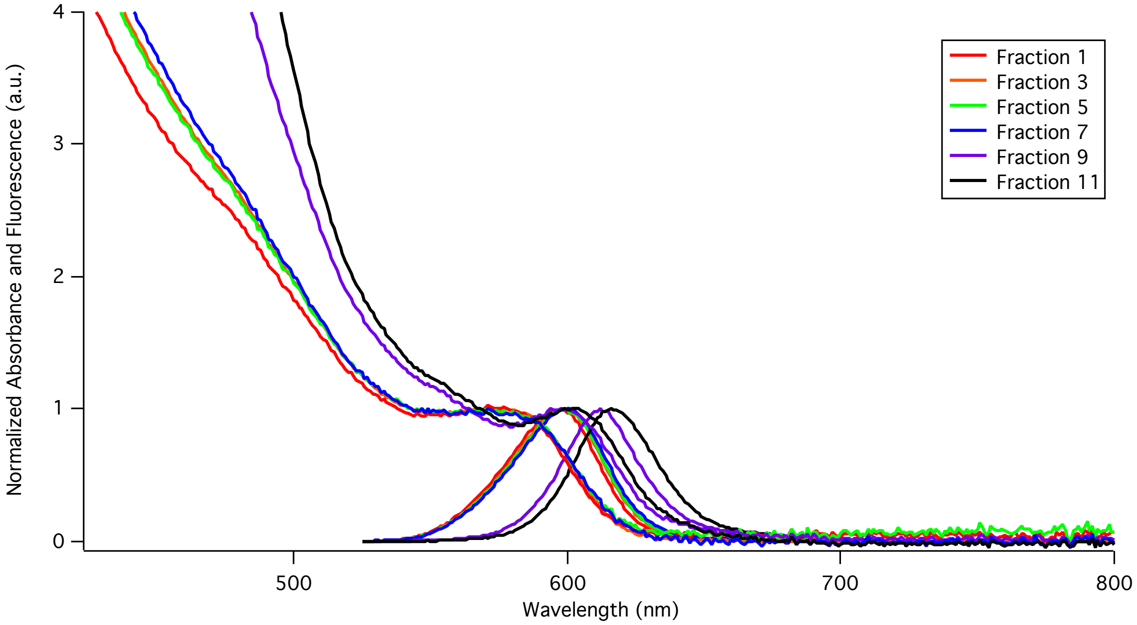

Figure 3.8. Absorption and fluorescence measurements for smaller elution fractions of graded alloy CdS_xSe_{1-x} QDs showing even better size selectivity.

Table 3.2. Size selection with additional smaller elution fractions

	Quantum Yield	Fluorescence Peak	Fluorescence FWHM	Absorbance Peak
Fraction 1	82.3	594	41	573
Fraction 3	78.2	595	41	573
Fraction 5	80.8	596	42	571
Fraction 7	73.0	597	42	571
Fraction 9	46.7	612	36	598
Fraction 11	59.7	618	38	599

Since smaller fractions provided the ability to further size separate the QDs, but without yielding a substantial quantity of QDs, the typical synthesis was doubled, and then separated into 5 fractions with the hope that this last fraction would contain mostly large, thick-shelled QDs. However, after fraction 5 showed just a small shift in fluorescence wavelength from fraction 1, an additional purification step was performed on the fifth fraction QDs whereby they were run through the column again and separated into eight additional fractions. The final eluted fraction from the second GPC step showed a further increase in the population of large dots as can be seen in the histogram Figure 3.9 and the TEM images in Figure 3.10. STEM-EDS also revealed that most of the QDs eluted in the last fraction after the second GPC step had a thick-shell of CdS (Figure 3.11).

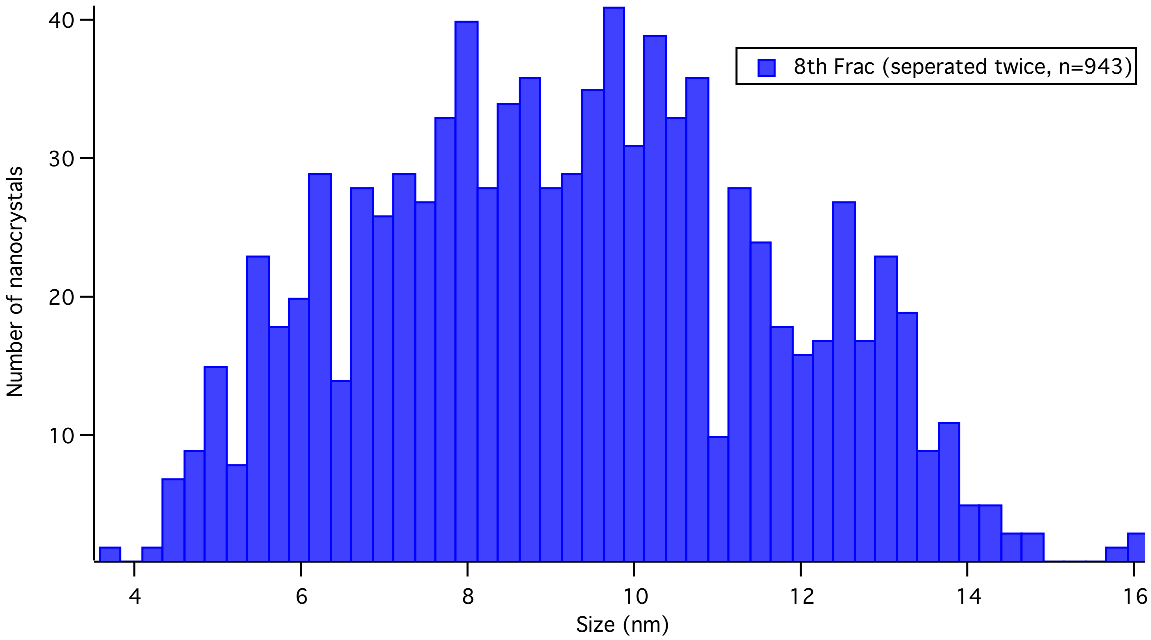

Figure 3.9. Histogram of sizes for the eighth fraction after second GPC purification step for CdS_xSe_{1-x} QDs from TEM images. This second purification step further amplified the large population of QDs.

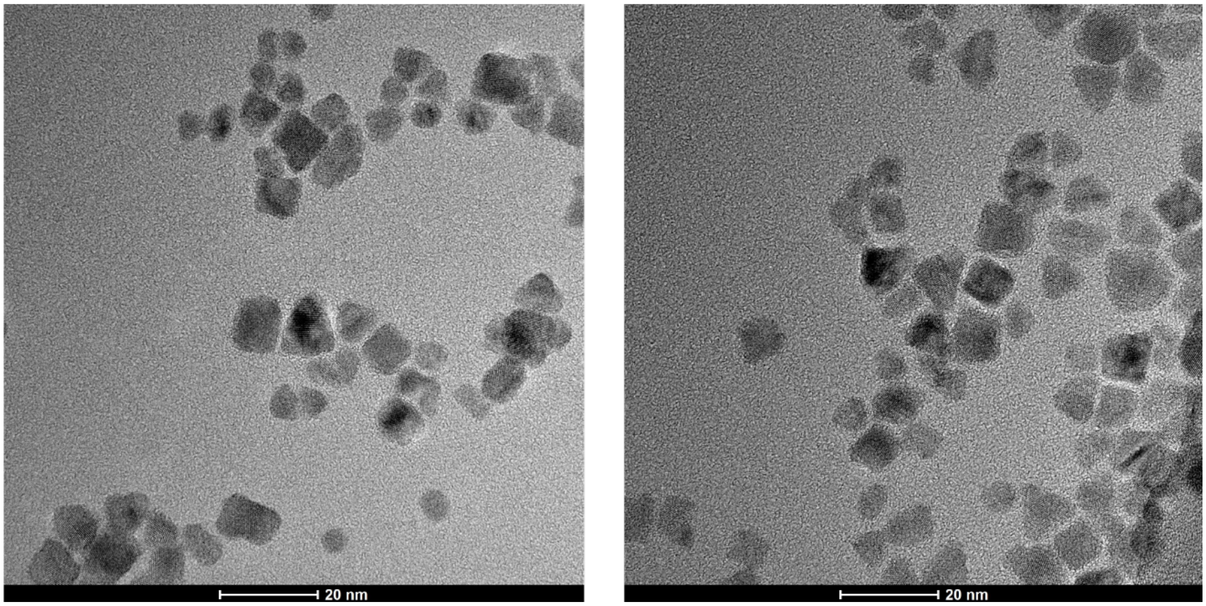

Figure 3.10. TEM images of the eighth eluted fraction of CdS$_x$Se$_{1-x}$ QDs from a second GPC step. The population of large QDs has been amplified.

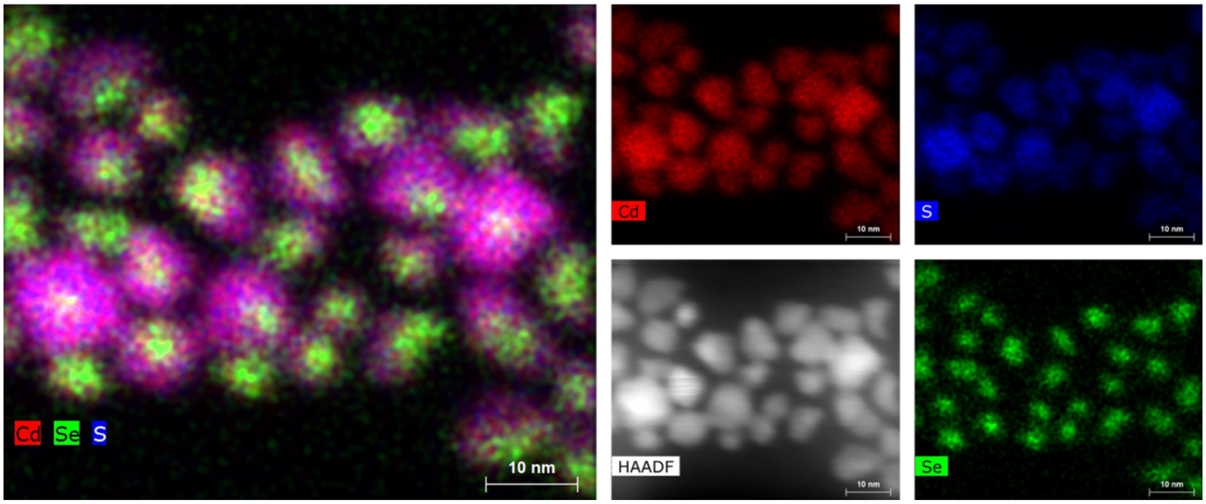

Figure 3.11. Eighth fraction of CdS$_x$Se$_{1-x}$ QDs STEM-EDS showing further amplification of large QDs with substantial sulfur incorporation upon the use of two GPC steps.

3.5 FUTURE WORK

By repeating the GPC technique twice on the same synthetic batch of QDs, the population of large dots has been selectively amplified. The large QDs show a shift in both absorption and emission, and a visible difference in size and elemental composition. This amplification of the population of large dots would allow for the ultrafast carrier dynamics of different subpopulations to be probed to determine how the carrier dynamics differ for those with a thin shell of CdS and those with a thicker shell. It is hypothesized that the addition of the extra CdS-shell to the core will further passivate the surface and increase radiative recombination of the charge carriers. This GPC can also then be applied to InP/ZnSe QDs as a method of separating the QDs by size whereby the largest QDs should show the most complete shell coverage.

CHAPTER IV

EFFECT OF INDIUM-ALLOY ON CARRIER DYNAMICS OF InP/ZnSe QUANTUM DOTS

The following chapter is primarily adapted from: Freymeyer, N. J.; Click, S. M.; Reid, K. R.; Chisholm, M. F.; Bradsher, C.E.; McBride, J. R.; Rosenthal, S. J., Effect of Indium Alloying on the Charge Carrier Dynamics of Thick-Shell InP/ZnSe Quantum Dots. *J. Chem. Phys.* **2020**, Accepted.

4.1 INTRODUCTION

As thoroughly discussed in the introduction, quantum dots (QDs) exhibit unique size-dependent optical and electronic properties resulting from quantum confinement.[1] Because of these properties, QDs are well suited for use in displays, as biological probes, in photovoltaic devices, and as low-threshold lasers.[3-8, 74-77] Many of these current applications rely on cadmium-based QDs due to the ease of synthesis of materials with high quality photophysical properties and a band gap that is size-tunable across the visible spectrum. However, growing concerns over the toxicity of cadmium[55] have led to increased research into cadmium-free QD alternatives. Indium phosphide (InP) QDs, in particular, offer size-tunable emission over the visible and near-infrared range and lower intrinsic toxicity.[22, 57, 59-61, 63] Currently, InP QDs often have low photoluminescence quantum yields (PLQYs) and reduced photostability,[22, 62] and continued development of InP QD materials is necessary to enable InP QDs to be synthesized with competitive properties to that currently available from CdSe QDs.

Substantial efforts have been made towards optimizing the photophysical properties of semiconductor nanocrystals by altering their surface chemistry. The surface of native QDs expose defects for charge carrier localization where dangling bonds from unpassivated surface atoms serve as trap states for charge carriers and prevent direct electron and hole recombination.[16] Often for CdSe the surface is passivated with additional organic ligands such as hexadecylamine.[26, 35] Alternatively, the application of a semiconductor shell with a wide band gap passivates the core QD surface atoms which helps to remove surface traps and to confine the charge carriers to the core of the QD.[19]

Unpassivated InP QDs are known to show extremely low to no PL emission due to a highly defective QD surface—thought to be dominated by phosphorus dangling bonds.[64] For this reason, InP QDs are typically passivated with a shell of a type-I band gap material such as ZnS to confine both electrons and holes to the QD core, decoupling them from the QD surface.[22] Alternatively, etching InP with hydrofluoric acid has also shown an increase in stability and PLQY.[78] Depending on the hydrofluoric acid concentration, this increase in PLQY can be attributed to either passivation of indium dangling bonds by fluoride ions acting as atomic ligands or photochemical etching of the InP QDs.[79] Recent efforts have also looked at the effect of an alloyed indium interface and the application of multiple shelling layers as ways of further confining charge carriers.[80] Particular interest is focused on application of a ZnSe shell because its smaller lattice mismatch (3.4% between core and shell, instead of the 7.7% seen for InP/ZnS) allows for a thicker shell to be grown.[65, 81-87] These thicker shelled QDs show improved photophysical properties and an increase in PLQY is observed.

As previously stated, ultrafast fluorescence upconversion spectroscopy probes charge carrier dynamics on femtosecond timescales and has helped the surface dynamics of QDs to be understood. Extensive work has been performed looking at these carrier dynamics for CdSe QDs.[14, 26, 34, 35, 42, 43] Some work has studied the ultrafast charge carrier dynamics on InP and InP/ZnS,[88-90] but remains limited as only thin shells of ZnS can be applied to InP cores because the relatively large lattice mismatch between core InP and shell ZnS limits epitaxial growth.

4.2 INITIAL THICK-SHELL InP/ZnSe QD SYNTHESIS

InP/ZnSe QDs were synthesized using the method described in chapter 2 as developed by Reid *et al.*[65] This section addresses initial work carried out to characterize these QDs.

4.2.1 Optical Characterization

Absorbance and PL for these thick-shelled QDs can be seen in Figure 4.1 where a large increase in absorption is observed at higher energies upon the application of the ZnSe shell. These thick-shell InP/ZnSe exhibited reduced blinking (95% on-times), narrow PL linewidths (40 nm FWHM), higher PLQY (40%) and longer biexciton lifetimes (~540 ps biexciton lifetime) than those seen for InP/ZnS QDs.

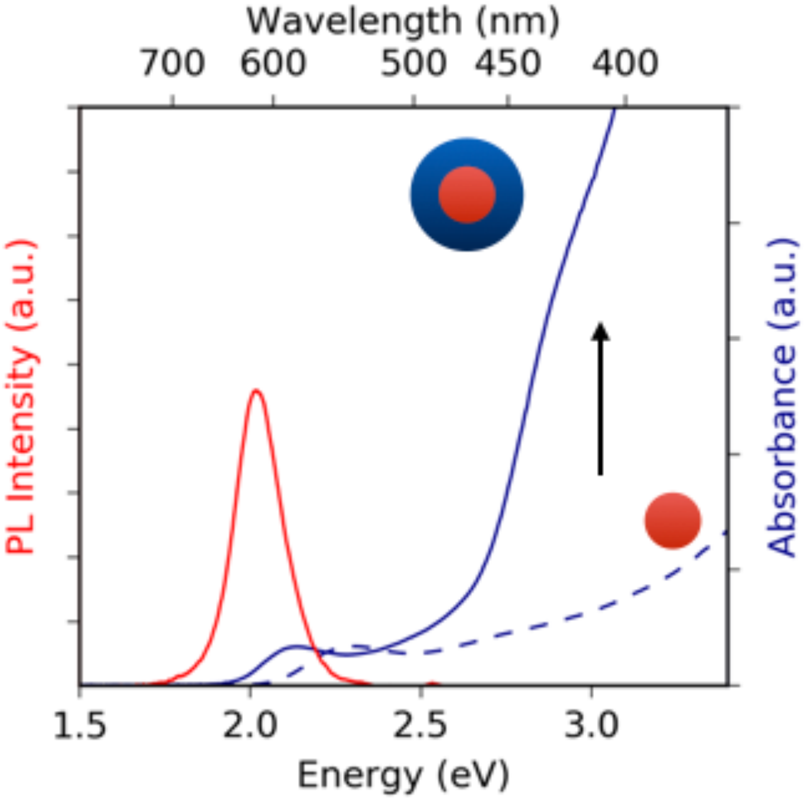

Figure 4.1. Absorbance (blue) and photoluminescence (red) of thick-shell InP/ZnSe QDs and absorbance of InP cores. The dashed line represents the unpassivated InP cores while the solid line represented the shelled InP/ZnSe nanostructure. Adapted with permission from Reid, K. R.; McBride, J. R.; Freymeyer, N. J.; Thal, L. B.; Rosenthal, S. J., Chemical Structure, Ensemble and Single-Particle Spectroscopy of Thick-Shell InP–ZnSe Quantum Dots. *Nano Lett.* **2018,** *18* (2), 709-716. Copyright 2017 American Chemical Society.

4.2.2 Structural Characterization

TEM and STEM-EDS were used to characterize these thick-shelled InP/ZnSe QDs. An increase in size from ~3.0 nm for the InP core to 14.1 nm for the thick-shell structure (Figure 4.2) was observed which corresponds to a shell thickness of ~5.5 nm (~17 monolayers). Some irregularity in the shapes and morphology of the QDs produced by our shell growth method is observed and can be seen in Figure 4.3. It is thought that these extended (bulk) shell defects propagate from the InP core region which prevents proper shell growth. These structural defects and their role in the photophysical properties of thick-shell InP/ZnSe QDs will be further discussed later when coupled with ultrafast fluorescence decay curves.

STEM-EDS of these thick-shelled QDs showed that the InP core tends to be centered in a symmetrically grown ZnSe shell (Figure 4.4). Interestingly, a significant amount of indium incorporation into the ZnSe shell was also observed for the first time in these QDs. Alloying of the interface between CdSe core and CdS shell has been shown to increase the biexciton lifetime and emission efficiency when compared to an abrupt core/shell boundary, and relaxes the confinement potential at the interface.[53, 91] As alloying of sulfur into CdS_xSe_{1-x} QDs has been shown to completely eliminate hole trapping by decreasing the interactions of charge carriers with the surface of the QD and reducing charge carrier trapping defects at the core/shell interface,[34] we theorized indium-alloy for InP/ZnSe would play a similar role on the carrier dynamics.

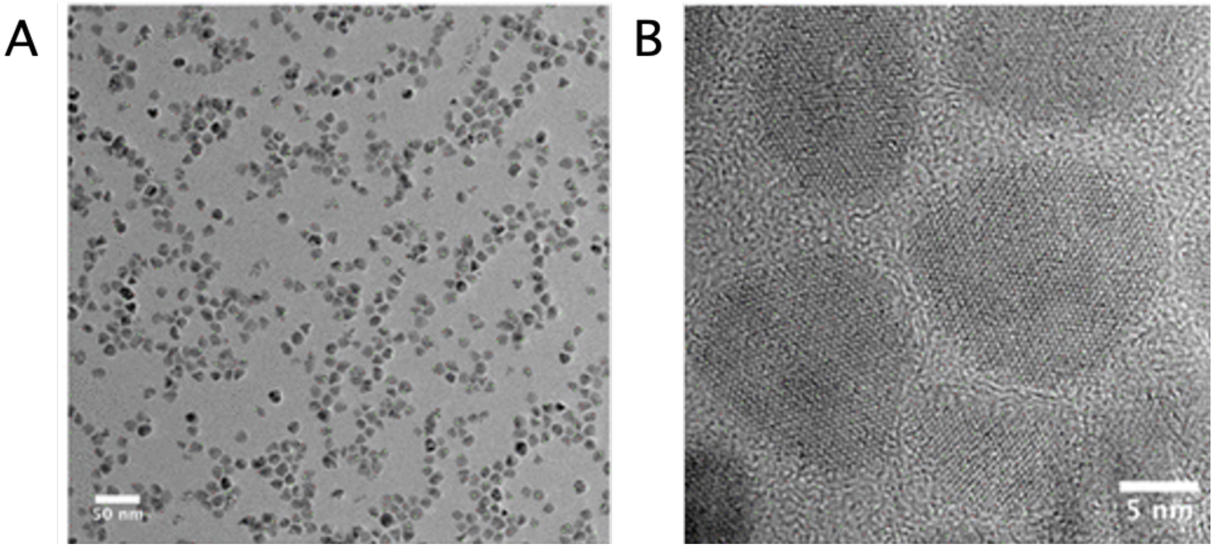

Figure 4.2. TEM images of thick-shell InP/ZnSe QDs where the thick-shell growth was attributed to the high temperature growth process and relatively low lattice mismatch. Adapted with permission from Reid, K. R.; McBride, J. R.; Freymeyer, N. J.; Thal, L. B.; Rosenthal, S. J., Chemical Structure, Ensemble and Single-Particle Spectroscopy of Thick-Shell InP–ZnSe Quantum Dots. *Nano Lett.* **2018,** *18* (2), 709-716. Copyright 2017 American Chemical Society.

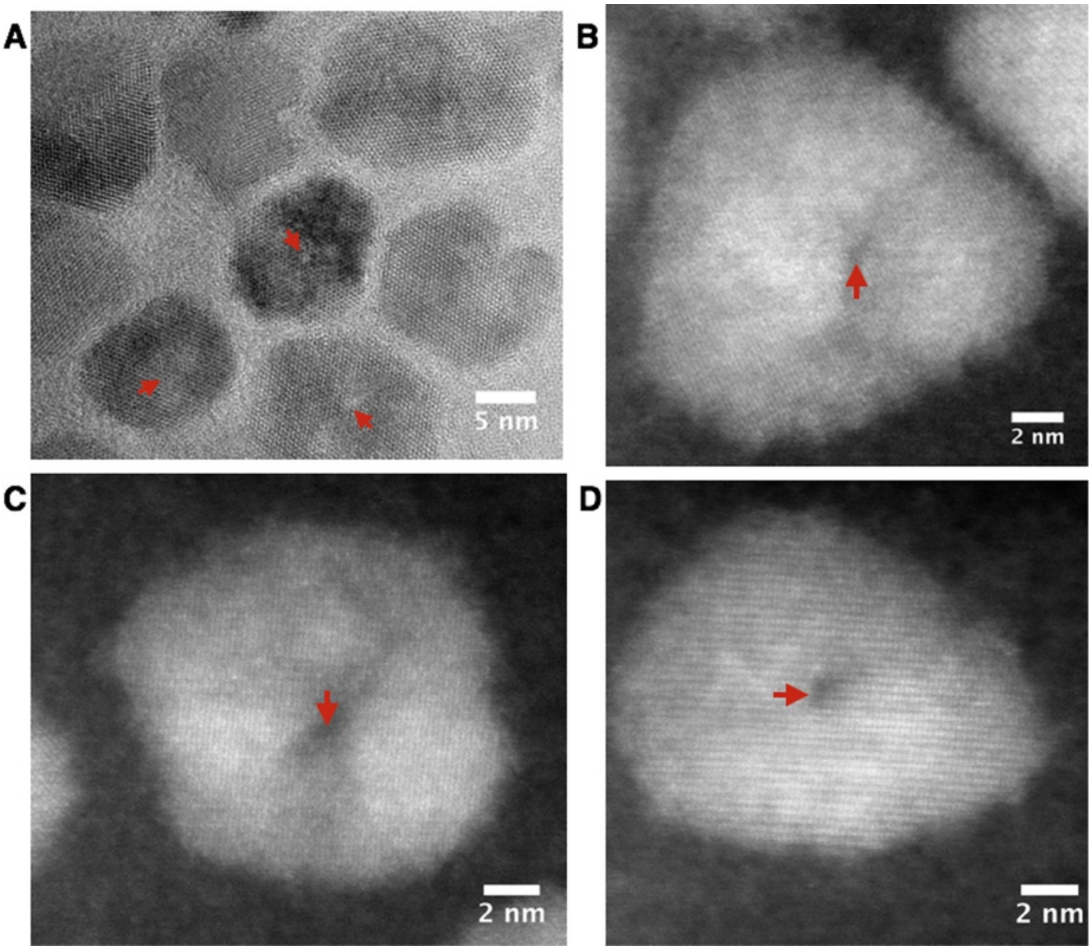

Figure 4.3. HR-TEM images of thick-shell InP/ZnSe QDs reveal defects present in many QDs. Defects are indicated with red arrows. Reprinted with permission from Reid, K. R.; McBride, J. R.; Freymeyer, N. J.; Thal, L. B.; Rosenthal, S. J., Chemical Structure, Ensemble and Single-Particle Spectroscopy of Thick-Shell InP–ZnSe Quantum Dots. *Nano Lett.* **2018,** *18* (2), 709-716. Copyright 2017 American Chemical Society.

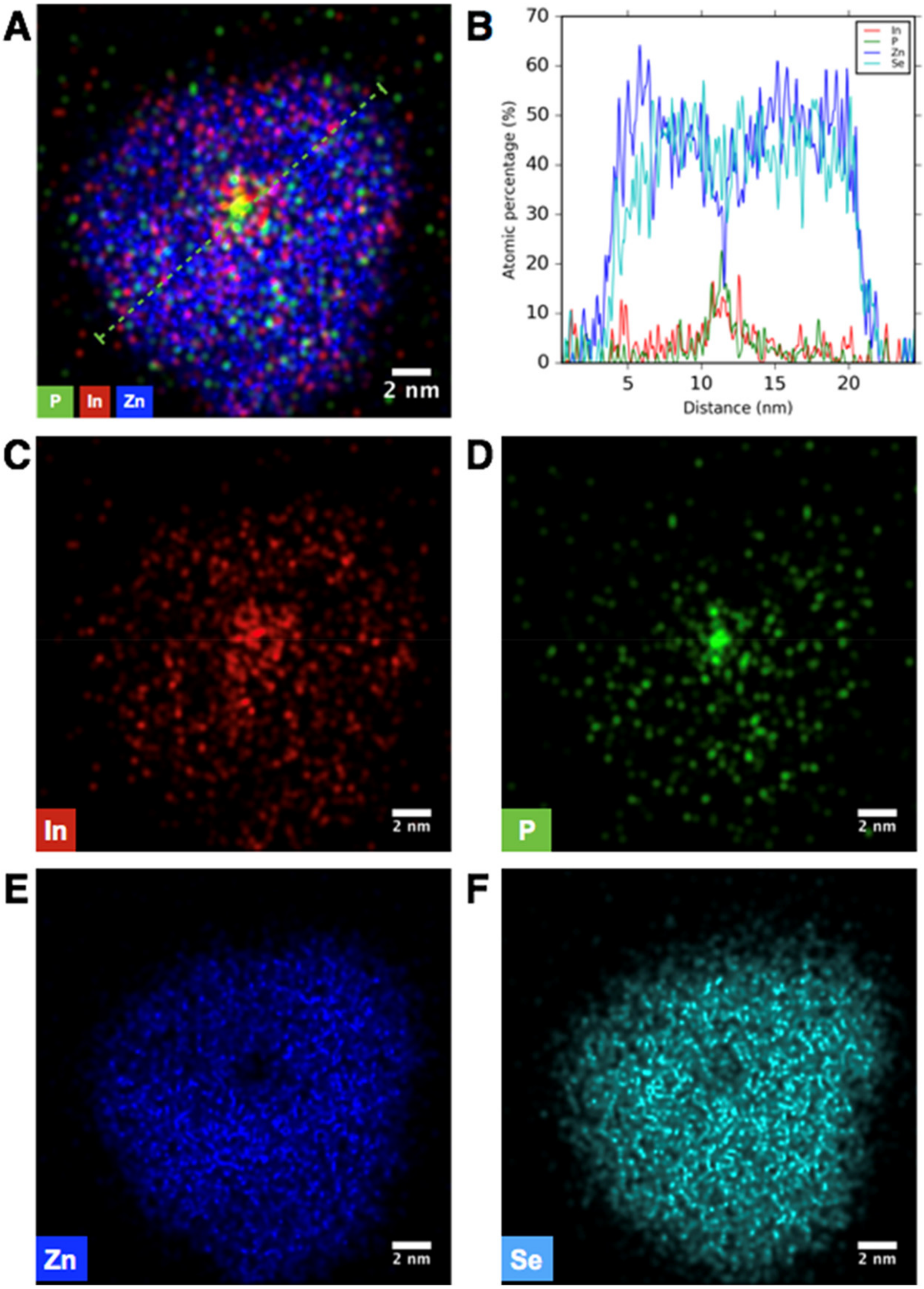

Figure 4.4. Elemental Mapping (STEM-EDS) of thick-shell InP/ZnSe QDs shows incorporation of indium from the core into the shell. Reprinted with permission from Reid, K. R.; McBride, J. R.; Freymeyer, N. J.; Thal, L. B.; Rosenthal, S. J., Chemical Structure, Ensemble and Single-Particle Spectroscopy of Thick-Shell InP–ZnSe Quantum Dots. *Nano Lett.* **2018,** *18* (2), 709-716. Copyright 2017 American Chemical Society.

4.3 EFFECT OF INDIUM-ALLOY ON CARRIER DYNAMICS OF InP/ZnSe QUANTUM DOTS

In this work, we report the synthesis of nanocrystals with and without this additional indium incorporation in the shell and provide structural characterization of these two QD structures. Furthermore, we used femtosecond fluorescence upconversion spectroscopy to investigate the effect of indium incorporation on the extent and speed of charge carrier trapping and its effect on radiative charge carrier recombination for these InP/ZnSe QDs.[92]

InP/ZnSe QDs were synthesized based on a modification of the above method developed by Reid *et al.* utilizing a continuous injection shelling method at high temperatures to grow a thick ZnSe shell on an InP core.[65] Two QD types were prepared using similar InP starting cores, but with a different chemical composition of the shell. QDs with indium incorporated into the shell, referred to in this text as 'alloy', were synthesized by following Reid *et al's* previously reported procedure where the shelling precursors were injected directly into unpurified cores in their reaction solution.[65] Unreacted indium precursor is thus free to be incorporated into the shell of the nanocrystals and create interface with both indium and zinc cations between the core and shell of the QDs over the course of the thick shell growth. Conversely, InP/ZnSe QDs with indium restricted to the core, hereon referred to as 'core/shell', were synthesized using a similar procedure with the addition of a purification step after the core InP synthesis reducing the amount of free indium available during the shelling procedure. As the unreacted indium has been removed, a more chemically abrupt interface is formed between the core and shell of the synthesized QDs.

4.3.1 Particle Characterization

Figure 4.5 shows the absorbance and photoluminescence spectrum for these two distinct structures. Both QD samples absorb (582 nm alloy/583 nm core/shell) and emit (614/612 nm) at very similar wavelengths despite the difference in shell composition. Additionally, both samples show similar PLQY with the alloy QDs at 30% and the core/shell QDs at 33%. Ensemble fluorescence lifetimes also exhibited similar behavior as the average lifetimes were found to be 16.56 ± 0.08 ns for the alloy and 17.92 ± 0.09 ns for the core/shell (Figure 4.6).

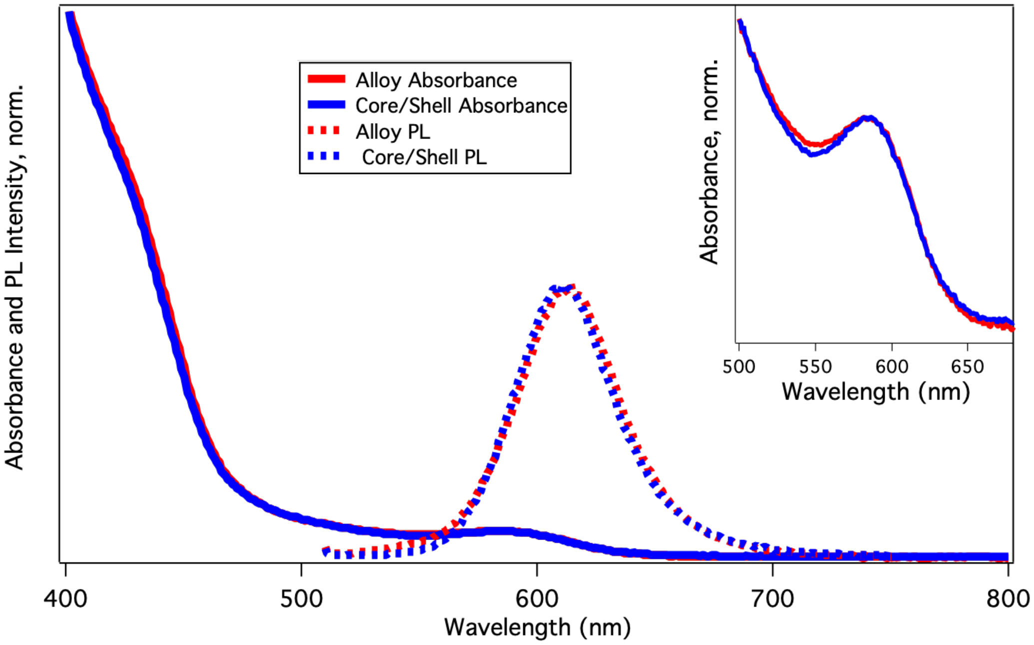

Figure 4.5. Absorbance and fluorescence of thick-shell InP/ZnSe QDs showing similar optical properties for both the alloy and the core/shell QDs.

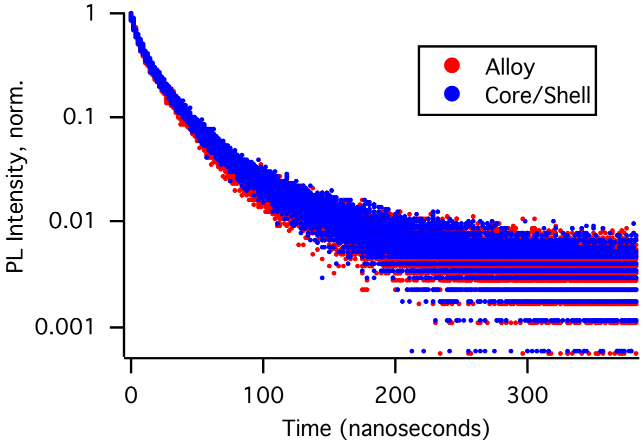

Figure 4.6. Nanosecond decay curves showing similar nanosecond lifetimes for both core/shell and alloy InP/ZnSe QDs

Scanning transmission electron microscopy coupled with energy-dispersive X-ray spectroscopy (STEM-EDS) was used to characterize the structure and elemental composition of the synthesized QDs. Similar InP core sizes (3.3 nm, Figure 4.7) are observed for both the alloy and core/shell samples which yield the observed absorption and PL. Upon application of a ZnSe shell, the average size for the alloy nanocrystals increased to 9.8 ± 3.7 nm , which is slightly smaller than the core/shell average of 11.9 ± 2.7 nm (Figure 4.8). Toufanian *et al.* have reported little shell-thickness dependence on the photoluminescence lifetimes for Zn-based shelling on InP QDs.[93] With the similar absorption, emission, and core size between the alloy and core/shell QDs, the indium in the shell is not directly contributing to the band gap of the QDs. Therefore, any measured differences in the ultrafast carrier dynamics can be attributed to the shell composition and not the slight difference in overall QD size. These optical and structural properties are summarized in Table 4.1.

Table 4.1 Structural and optical properties of thick-shell InP/ZnSe QDs

	Core/Shell	Alloy
Absorbance (nm)	583	582
Emission (nm)	612	614
Quantum Yield (%)	32.8	29.4
Core Size (nm)	3.3 ± 0.4	3.3 ± 0.6
Particle Size (nm)	11.9 ± 2.7	9.8 ± 3.7

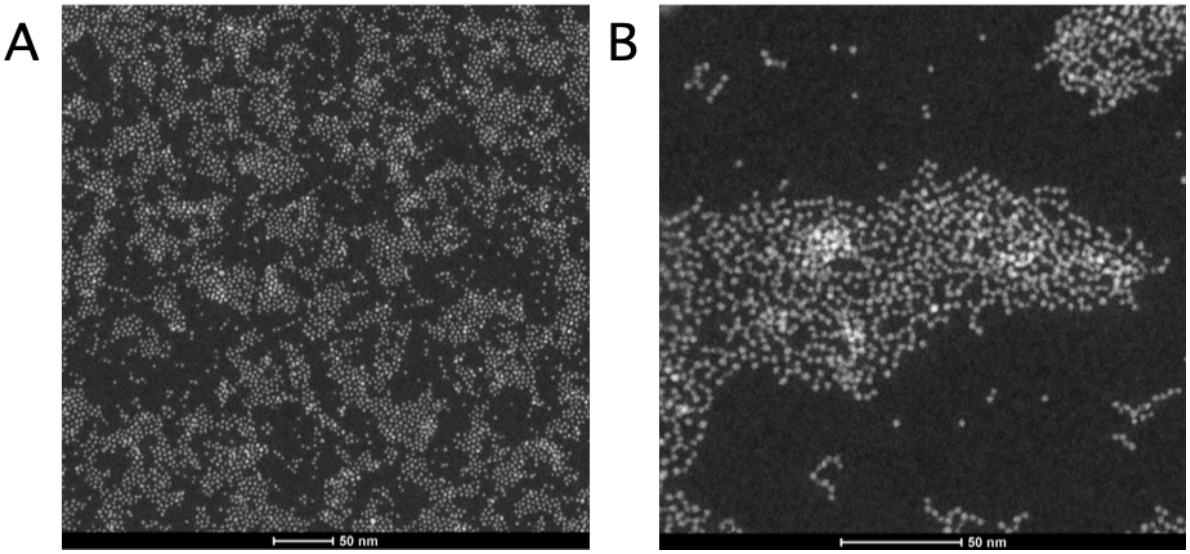

Figure 4.7. STEM images of InP Cores A) InP cores used for alloy QDs B) InP cores used for InP core/shell QDs (acquired at different magnifications)

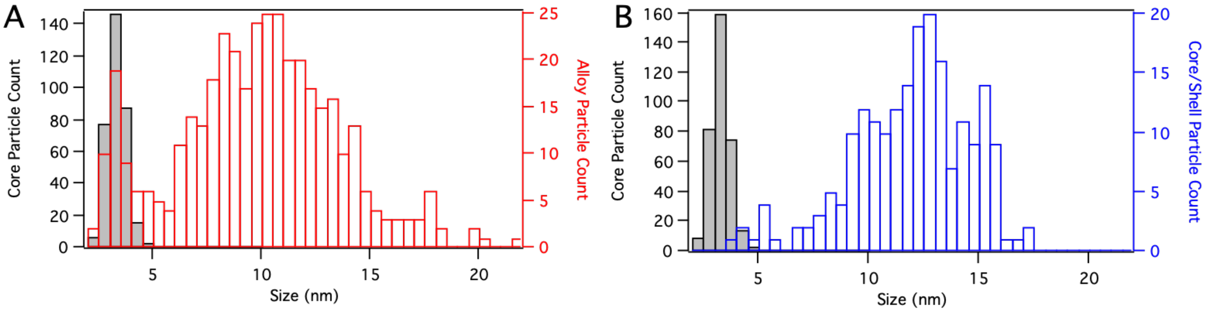

Figure 4.8. Size distributions of (a) alloy InP/ZnSe QDs and (b) core/shell InP/ZnSe QDs. The filled black boxes show the sizes of the InP cores while the colored outlines reflect the complete InP/ZnSe nanocrystals.

Figures 4.9 and 4.10 show EDS maps for the two compositions. A clear difference can be seen where the indium is confined to the core for the core/shell QDs while the alloy QDs show more indium farther from the core. An increase in indium atomic percentage is seen both for the total QD and the shell of the alloy QDs with atomic percentages of about 3.1% indium and 0.6% phosphorous in the shell. The core/shell QDs showed much lower percentages (1.4% In and 0.3% P in shell, see table 4.2 for complete percentages). A line scan of an individual particle (Figures 4.11 and 4.12) also show greater indium counts in the shell of the alloy QDs relative to the core/shell QDs. Therefore, while there are trace amounts of indium located throughout both shells, there is significantly more indium consistently alloyed in the alloy sample.

Table 4.2 Atomic percentages for thick-shell InP/ZnSe QDs synthesized with differing indium incorporations into the shell. These percentages are averages across at least 4 QDs.

	Alloy			Core/Shell		
Element	Total (Atomic Percent)	Shell (Atomic Percent)	Core (Atomic Percent)	Total (Atomic Percent)	Shell (Atomic Percent)	Core (Atomic Percent)
Indium	3.6	3.1	4.7	2.2	1.4	6.0
Zinc	69.0	72.0	58.5	52.7	53.0	48.1
Selenium	26.5	24.4	34.6	43.5	45.2	41.1
Phosphorus	0.9	0.6	2.2	1.5	0.3	4.0

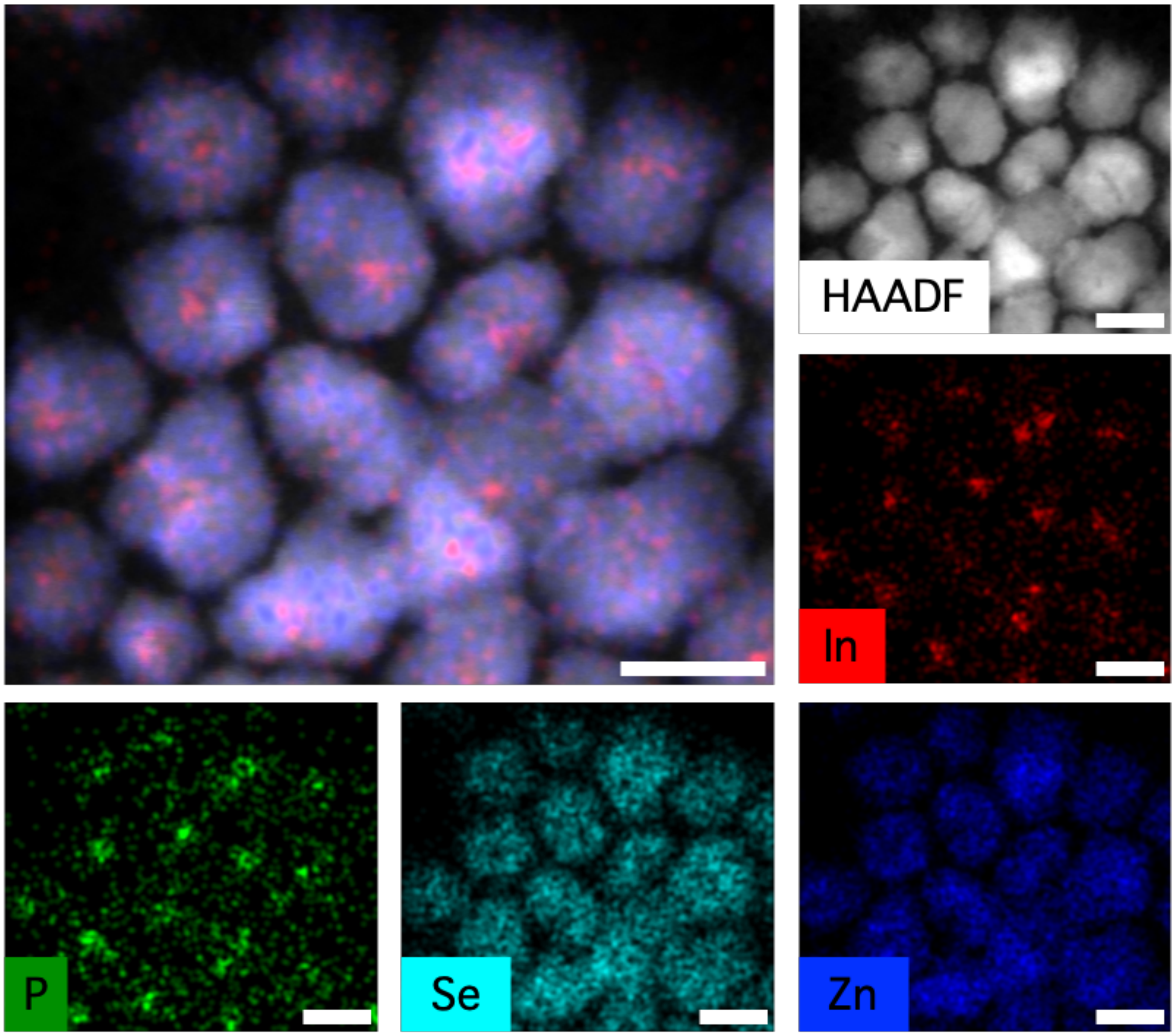

Figure 4.9. STEM-EDS of thick-shell core/shell InP/ZnSe QDs showing a more rigid interface between the core InP and the shell ZnSe. This interface reduces the amount of In seen in the entire particle. Scale bar = 10 nm

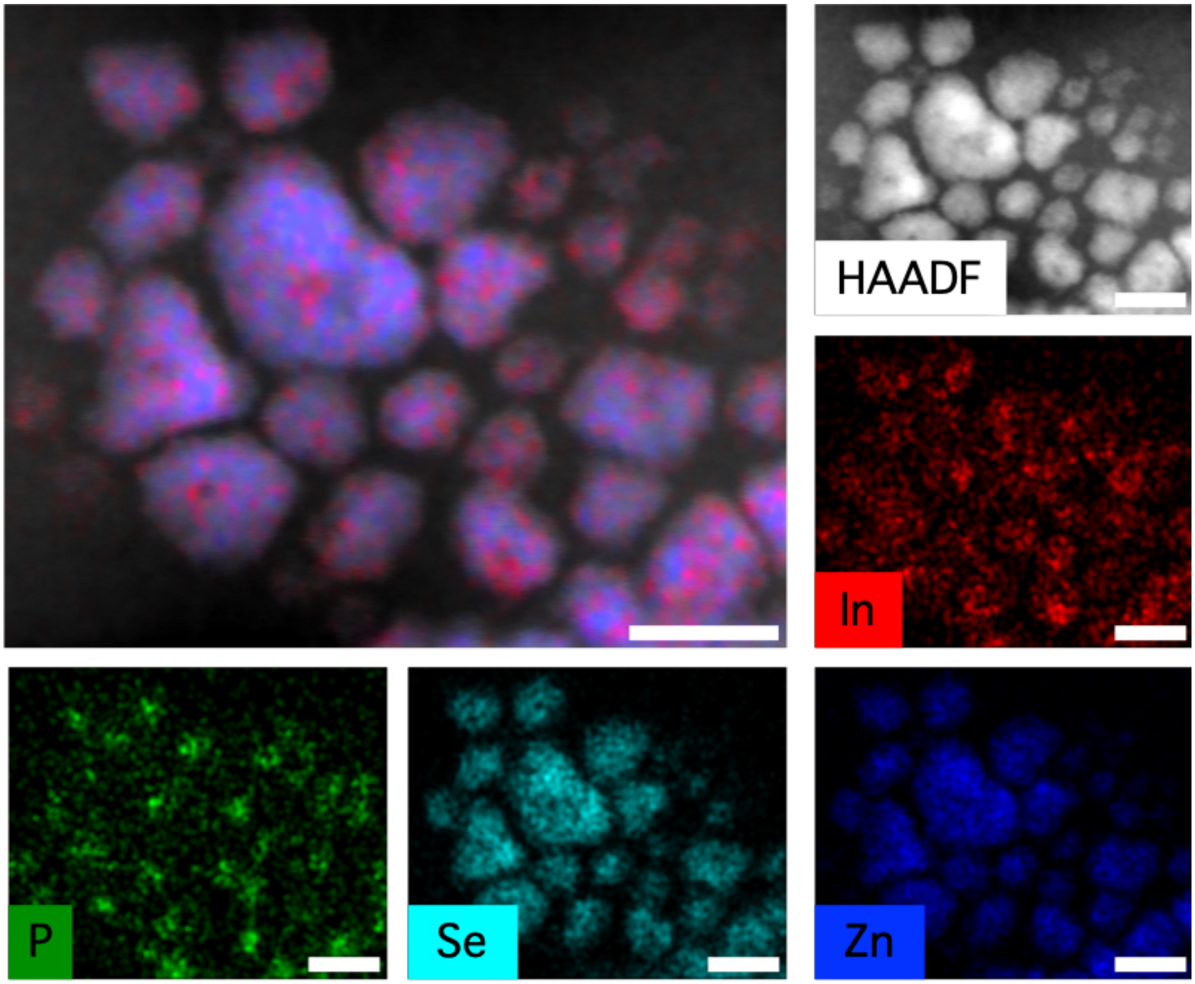

Figure 4.10. STEM-EDS of alloy InP/ZnSe QDs showing incorporation of indium into the ZnSe shell. Scale bar = 10 nm

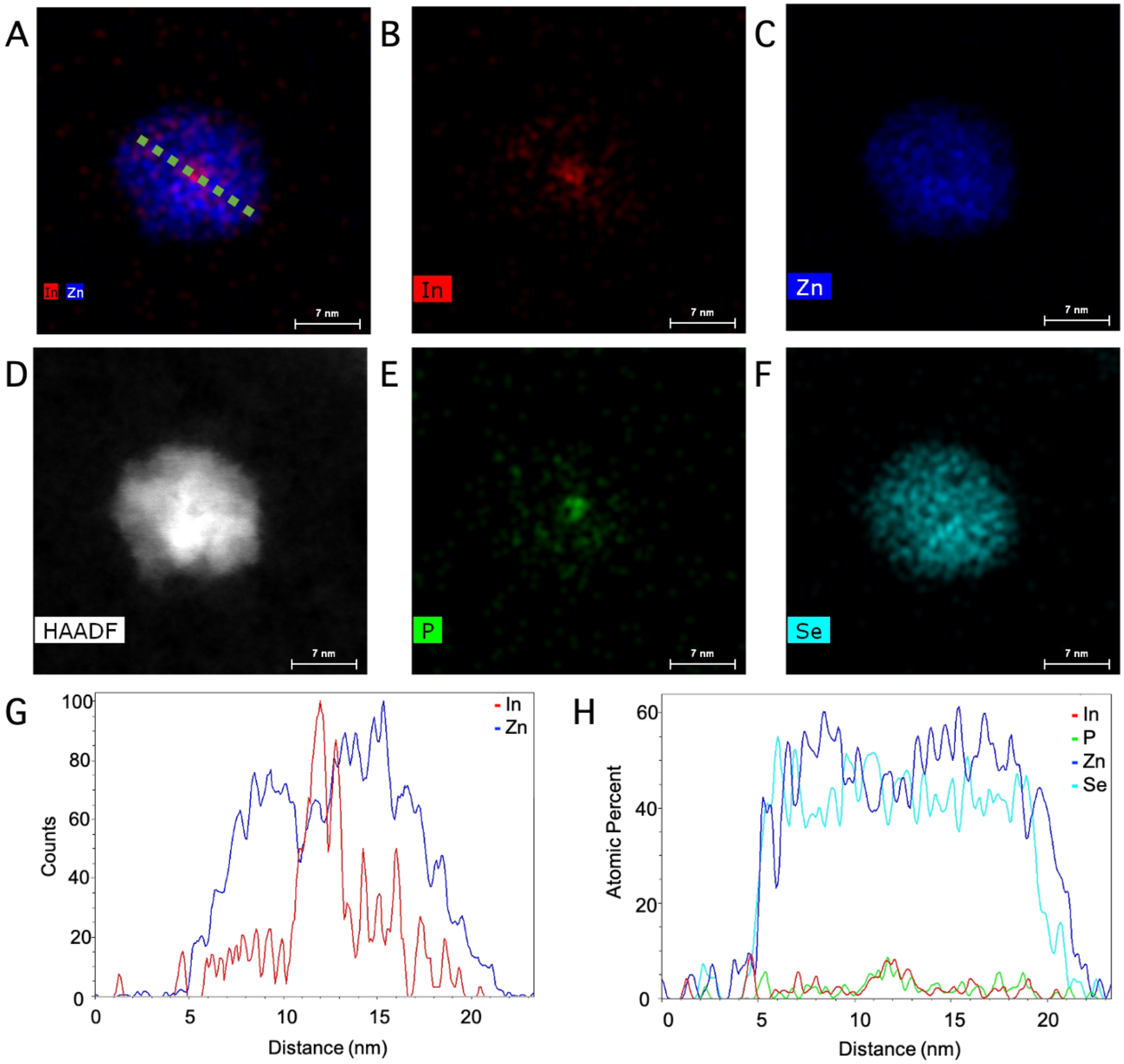

Figure 4.11. Elemental characterization of a core/shell InP/ZnSe QD obtained using STEM-EDS. A) Energy dispersive X-ray chemical map. Map of B) Indium intensity C) Zinc intensity D) HAADF E) Phosphorous intensity F) Selenium intensity G) Map of counts of indium and zinc signal following the green line in A). A spike in indium signal is seen in the core of the QD. H) Map of atomic percentages for indium, phosphorous, zinc, and selenium across the same line shown in A). This confirms the thick-shell of ZnSe with an increase is both indium and phosphorous in the core of the QD.

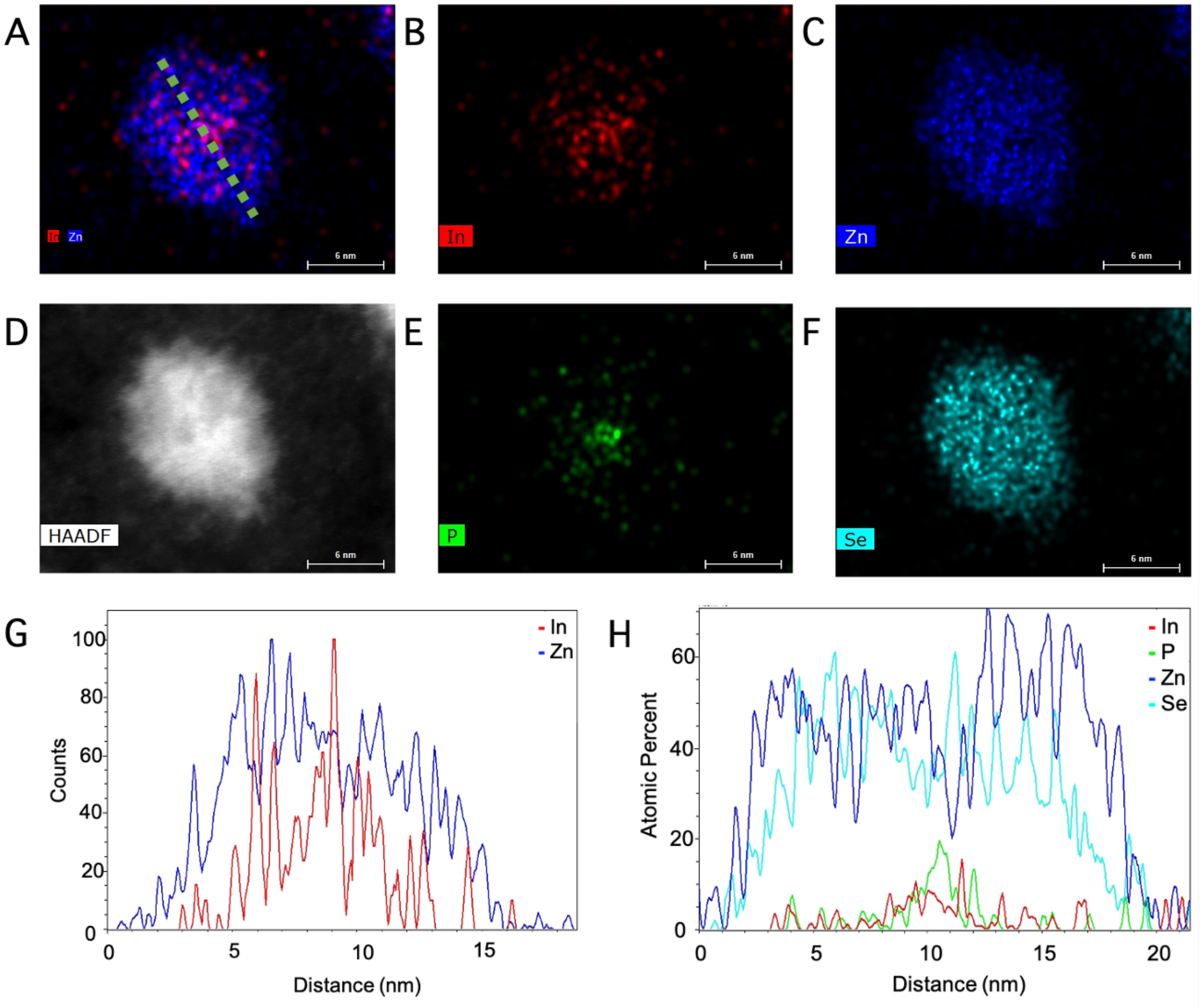

Figure 4.12. Elemental characterization of an alloy InP/ZnSe QD obtained using STEM-EDS. A) Energy dispersive X-ray chemical map. Map of B) Indium intensity C) Zinc intensity D) HAADF E) Phosphorous intensity F) Selenium intensity. G) Map of counts of indium and zinc signal following the green line in A). Greater indium intensity is observed throughout the QD. H) Map of atomic percentages for indium, phosphorous, zinc, and selenium across the same line shown in A). This confirms the thick-shell of ZnSe with an increase is both indium and phosphorous in the core of the QD with some additional indium incorporation in the shell of the alloy QDs.

Additionally, aberration-corrected STEM was used to characterize these thick-shell InP/ZnSe QDs (Figure 4.13). While InP has a lower percentage of lattice mismatch with ZnSe than ZnS, epitaxy of ZnSe onto InP is still challenging. The observed uneven and irregular shell coverage likely contributes to the decreased PLQY observed for both alloy and core/shell QDs as it has been shown that defect-free coverage and a reduction in dark QDs are both necessary for high PLQYs.[31] This lack of uniform coverage likely causes structural and electronic defects that negatively affect the optical properties of our InP/ZnSe QDs.[94]

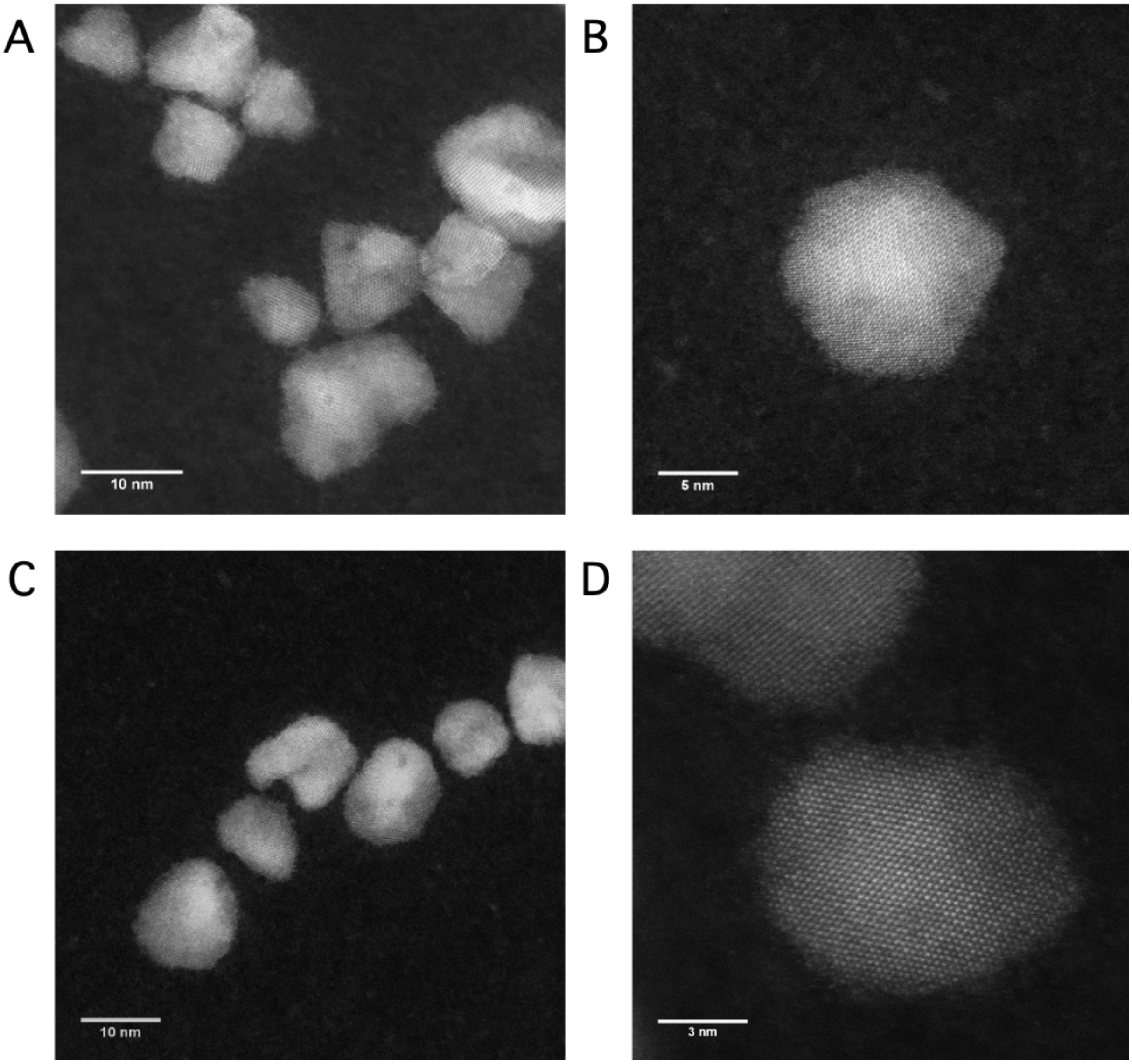

Figure 4.13. A) and B) Aberration-corrected STEM images of core/shell InP/ZnSe QDs. C) and D) Aberration-corrected STEM image of alloy InP/ZnSe QDs.

4.3.2 Ultrafast Data Analysis

To investigate the effectiveness of the surface passivation for the two different interfaces, femtosecond fluorescence upconversion spectroscopy was used to probe the charge carrier dynamics. The experiment utilized a femtosecond laser system previously described in Chapter 2.[34, 35, 43] The ultrafast fluorescence upconversion spectra were fit as previously discussed with 4 decay components.[35] In this case, τ_4 was taken from the nanosecond fluorescence lifetime measurements and held constant during ultrafast data fitting. Using a global τ_1 was first determined from ultrafast data taken every 20 fs immediately before and after QD excitation (see Figure 4.14a), τ_2 and τ_3 were both then determined while fitting the decay observed in the first 100 picoseconds after excitation (with points obtained every 200 fs, see Figures 4.14b and 4.14c). The ultrafast decay curves of both the alloy and core/shell InP/ZnSe QDs can be seen in Figure 4.14 and the results of the fittings are summarized in Table 4.3.

Table 4.3 Ultrafast carrier dynamics for alloy and core/shell InP/ZnSe QDs

	rel. amp_2	rel. amp_3	rel. amp_4	τ_1 (ps)	τ_2 (ps)	τ_3 (ps)	τ_4 (ns)
Core/Shell	0.22 ± 0.08	0.58 ± 0.08	0.21 ± 0.1	0.1607 ± 0.0124	5.9 ± 2.7	26.1 ± 3.8	17.92 ± 0.09
Alloy	0.38 ± 0.03	0.60 ± 0.02	0.01 ± 0.01	0.1427 ± 0.0087	5.5 ± 0.7	36.8 ± 3.1	16.56 ± 0.08

The rise time (τ_1) has a negative amplitude and reflects the amount of time that it takes for the QDs to begin emitting after excitation and accounts for hot carrier cooling.[34] A very short rise time is observed for both alloy (144 fs) and core/shell sample (161 fs) with the alloy sample showing a slightly faster rise time than the core/shell sample. These values for InP/ZnSe match closely to previous work on InP/ZnS and InP QDs that suggests carrier cooling occurs on very short (~200 fs) timescales and that the rise time is independent of the shell composition.[78] Recent ultrafast transient absorption experiments on core/alloy/shell InP/ZnSeS QDs again suggest that exciton cooling occurs quickly in InP-based QDs.[95]

Both the core/shell and alloy InP/ZnSe QDs exhibit overall fast decays, that are attributed to the band alignment between the core InP and shell ZnSe. Given the small offset in band gap between quantum confined InP and ZnSe, the charge carriers are not fully confined to the core of the QDs and are thus likely trapped both at the interface between the InP and the ZnSe and at the QDs surface. This trapping reduces the amount of radiative recombination that can occur.

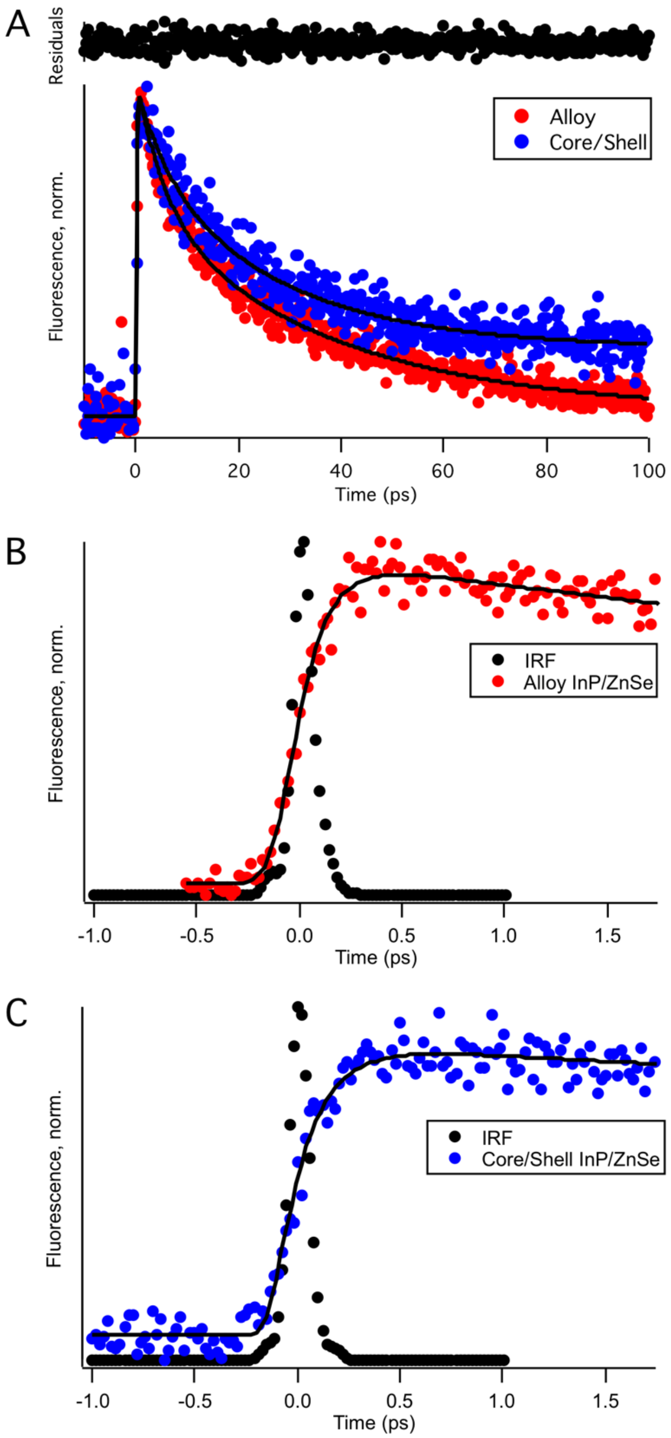

Figure 4.14. Ultrafast fluorescence decay curves for both alloy and core/shell InP/ZnSe QDs. Each curve is the summation of ten individual scans. Residuals are typical for both scans. A) Full long scan B) and C) Short scans used to calculate τ_1, the time it takes for the QDs to begin emitting. The decay trace is overlaid with the IRF.

Triple exponential decay of both alloy and core/shell samples was observed, but the decay's rate and extent for each process differed. Based upon the effective masses of the charge carriers for InP ($m_h^* = 0.65, m_e^* = 0.067$) , the decays are assigned to hole trapping (τ_2), electron tapping (τ_3), and radiative recombination respectively (τ_4).[34] τ_4 is the long-lived radiative recombination component of the decay, which extends past the lifetime of this ultrafast fluorescence upconversion experiment, and was measured using a nanosecond experiment (see Figure 4.6). Figure 4.15 summarizes the differences in carrier dynamics between the two samples.

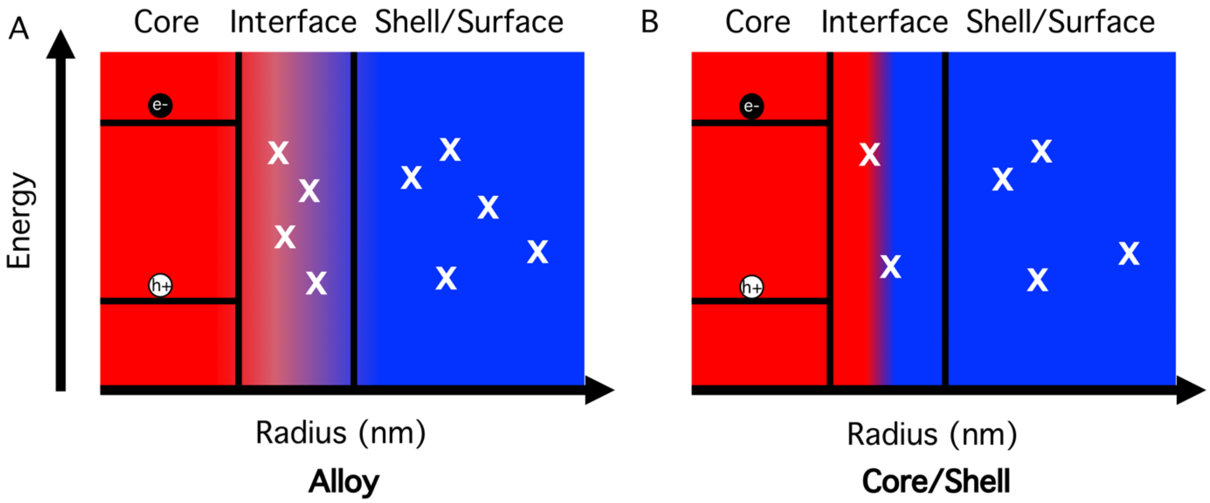

Figure 4.15. Summary of charge carrier dynamics in thick-shell InP/ZnSe QDs. More extensive trapping occurs in the alloy QDs than the core/shell QDs. The incorporation of indium into the shell allows for rapid localization of charge carriers at many interfacial sites.

The second decay constant, τ_2, and its relative amplitude reveal that rapid hole trapping contributes a smaller overall portion to the observed decay for both samples compared to τ_3, which is associated with electron trapping. The domination of electron trapping matches previous work carried out by Rowland *et al.* who observed electron trapping as the dominant trapping mechanism in InP and InP/ZnS QDs using ultrafast transient absorption (TA) spectroscopy.[96]

While both systems show similar trapping time constants, the extent of trapping for the alloyed QDs is greater than what is seen for the core/shell QDs, particularly for rapid hole trapping. Since the electron microscopy indicates both alloy and core/shell particles exhibit similar morphologies, the only major difference would be the inclusion of a higher amount of indium in the shell. This indicates the inclusion of In^{3+} creates vehicle for accelerated hole trapping. In and P have been shown to be electronic dopants for II-VI semiconductors and generate intra-gap states serving as non-radiative recombination centers.[80] For the case where indium atoms are incorporated into ZnSe, two additional energy levels are generated 0.59 and 0.41 eV above the valence band which provide multiple states for extensive trapping.[97] These additional energy levels allow for rapid localization of the charge carriers and prevent radiative recombination. The more extensive trapping in alloyed QDs confirms that indium alloying is detrimental to long-lived carriers and thus their radiative recombination.

Although the chemical composition of the thick ZnSe shell is different between these QD systems, the overall ultrafast carrier dynamics remain similar. This similarity indicates that the structural irregularities in the shell coverage revealed by the aberration-corrected STEM images in Figure 4.13 are more influential than the indium dopant states. These states rapidly populate then remain saturated resulting in similar static quantum yields as the core/shell samples. However, the defects states created by the indium in the shell will likely limit the maximum attainable quantum yield through improved shell passivation. An additional layer of a material with higher energy of the conduction band should enhance the PLQY by preventing the electron from reaching the surface trap states.[82] ZnS provides a wider band gap and should better confine charge carriers, but comes with greater lattice mismatch and greater defects and the interface between core and shell which can also prevent charge carrier recombination. Therefore, minimizing the extent of indium alloying and growing an outer layer of a wider bandgap material (ZnS on top of the ZnSe layer) are both important next steps in the development of an ideal InP QD system. Won *et al.* and Lee *et al.* have made significant progress recently on improving the brightness and structure of InP/ZnSe/ZnS QDs.[63, 98]

4.4 CONCLUSION/FUTURE DIRECTIONS

Core/shell and alloy thick-shell InP/ZnSe QDs were synthesized by varying the amount of indium incorporated into the ZnSe shell. These QDs were characterized with extensive structural and optical data to investigate the effect on charge carrier dynamics. While both of these QD systems offer a thick-shell architecture which should help increase radiative recombination in QDs, ultrafast fluorescence upconversion spectroscopy data revealed that extensive charge carrier localization still occurs in both QD structures. Extensive carrier trapping in the alloyed QDs suggests that minimizing alloying is required when applying a II-VI semiconductor shell to a III-V core.

CHAPTER V

CONCLUSIONS AND FUTURE WORK

5.1 OVERALL CONCLUSIONS

The surface of a QD provides many locations for charge carrier localization and thus needs to be passivated with a material that is both structurally and optically suited towards the core material. While alloying has proven an effective method of reducing lattice strain and core/shell defects for certain QD system, further size selection or shelling of graded alloy CdS_xSe_{1-x} is required to further optimize its photophysical properties.

On the other hand, charge imbalances when alloying between a II-VI semiconductor shell and III-V core generate far more sites for charge carrier localization than any benefits obtained from reduced lattice strain. For the thick-shell InP/ZnSe QDs discussed here, not only is it important to reduce indium incorporation in the shell, but also to add further wide bandgap material to successfully electronically confine the carriers to the InP core.

5.2 FUTURE DIRECTIONS

Synthetic refinements on emerging QD systems remains critical towards their use in future applications. Ultrafast spectroscopy helps optimize QDs by determining which synthetic change most improves a material's photophysical properties. As had been seen for CdSe-based QDs initially, improved surface passivation leads to better charge carrier recombination. However, the role of the core/shell interface differs when combining materials of different charges. By studying the ultrafast charge carrier dynamics of these emerging QD systems, the most ideal size, shape, and composition can be selected for particular applications.

5.2.1 Thick-Shell InP/ZnSe

As discussed previously, indium incorporation into a ZnSe shell provides extensive locations for charge carrier trapping unlike what is observed with anion alloying in CdS_xSe_{1-x} QDs. These localizations sites occur due to the charge imbalance caused by replacing a Zn^{2+} with an In^{3+}. To improve the carrier dynamics of this system, further synthetic refinement is needed to minimize the extent of indium alloying and grow an outer layer of a wider bandgap material. ZnS is currently being explored as the material to add on top of the ZnSe layer. Using an intermediate layer of ZnSe reduces the core/shell lattice strain that would be observed with just an InP/ZnS QD. The outside ZnS layer would serve to better electronically passivate InP. These new InP/ZnSe/ZnS QDs can then be evaluated to see the improved surface passivation using ultrafast fluorescence upconversion spectroscopy.

InP has a larger Bohr exciton radius (10 nm) relative to that of CdSe (5.6 nm) meaning more sizes of QDs can be synthesized with quantum confinement. With a larger range in sizes of QDs, the difference in carrier dynamics might be more significant than what has already been seen for CdSe. Ideally the charge carrier dynamics should be evaluated for various sizes of InP core as has been carried out for CdSe, but challenges exist both in synthesizing various sized InP QDs, and in successful passivation of the surfaces of these QDs.

5.2.2 Zn_3N_2

Zinc nitride provides another potentially useful QD system that removes the hazardous heavy metal cadmium. As with InP, these QDs offer significant tunability of emission wavelengths from 500-1100 nm.[56] Unlike InP, their unshelled QYs are already greater than 50% indicating interesting charge carrier dynamics as both CdSe and InP cores have QYs of less than 10%. While there has been one reported synthesis of Zn_3N_2, there has been almost no characterization of the photophysical properties because of their susceptibility to aggregation and oxidation. Shelling Zn_3N_2 with another material should reduce the extent of oxidation. However, at this point no reported shelling methods for the Zn_3N_2 core are available so further synthetic refinements are necessary before the charge carrier dynamics of this material will be fully discovered.

APPENDIX A

Cleaning the Inside of the Verdi Output Coupler

Dust and dirt can become deposited onto the inside of the Verdi output coupler which defocuses the beam and causes mode-locking issues in the Mira. If this occurs, visual observation of the output coupler may show a spot near the center where the beam passes through that is discolored from the rest of the output coupler (Figure A.1). If the Verdi beam is not properly focused into the Ti:Sapph in the Mira, the output coupler is the likely cause. The beam will be focused prior to its arrival at the crystal. If the output coupler is the issue, do not adjust the focusing lens, but carefully follow the steps below to remove the Verdi cover and clean it.

1. Ensure that the Verdi is turned off and the shutter is closed.
2. Remove the Verdi cover by unscrewing the four screws in the lid that are circled in Figure A.2.
3. Remove the front of the Verdi by unscrewing two additional screws. The power cable for the light will also need to be removed by simply disconnecting the cable. See Figure A.3.
4. Note the shutter on the front left of the Verdi (next to output coupler). It should be marked for which direction is closed. Make sure during reassembly that it gets placed back together correctly.
5. The entire front box containing the output coupler can be removed by removing the screws as shown in Figure A.4.
6. Clean both the outside and the inside of the output coupler with methanol.

7. Replace box containing output coupler into laser being careful that heat sink below is properly set in place and that while resetting the shutter adapter the two markings are properly aligned.
    a. Before replacing the lid, press the shutter open button on the front panel several times to make sure that it is properly aligned and moving.
8. The Verdi will likely have an error on the front of the power supply regarding the laser safety light being disconnected; press yes to make it go away once it has been reconnected.
9. When aligning the Mira, typical power output values are 1.2 W in the auxiliary cavity, 830 mW CW in the main cavity, and 560 mW modelocked. For the RegA, 1.4 W uncompressed, 1.0 W compressed. In the OPA, typically >20 mW can easily be obtained.

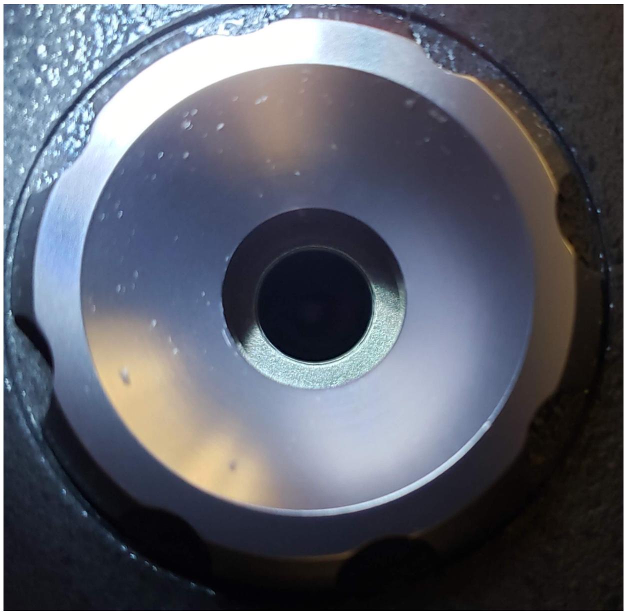

Figure A.1. Dust accumulation on the inside of the Verdi output coupler. Note the place that looks like a smudge slightly below and left of center.

Figure A.2. Coherent Verdi-V18 showing (red circles) which screws need to be removed to slide the cover off.

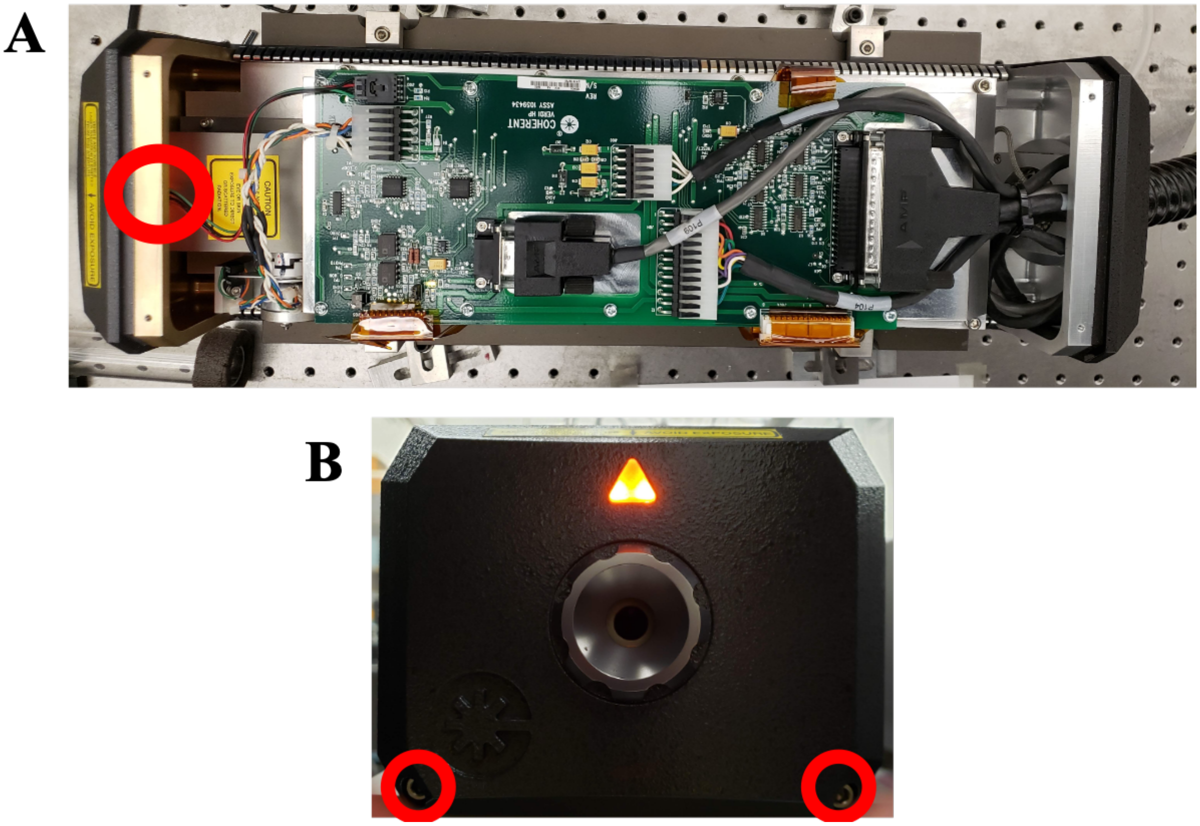

Figure A.3. A) Inside of the Verdi showing where the hazard light disconnects from the front panel. Carefully remove the cable from the front cover. B) The two screws that need to be removed on the front cover so that it can be disassembled.

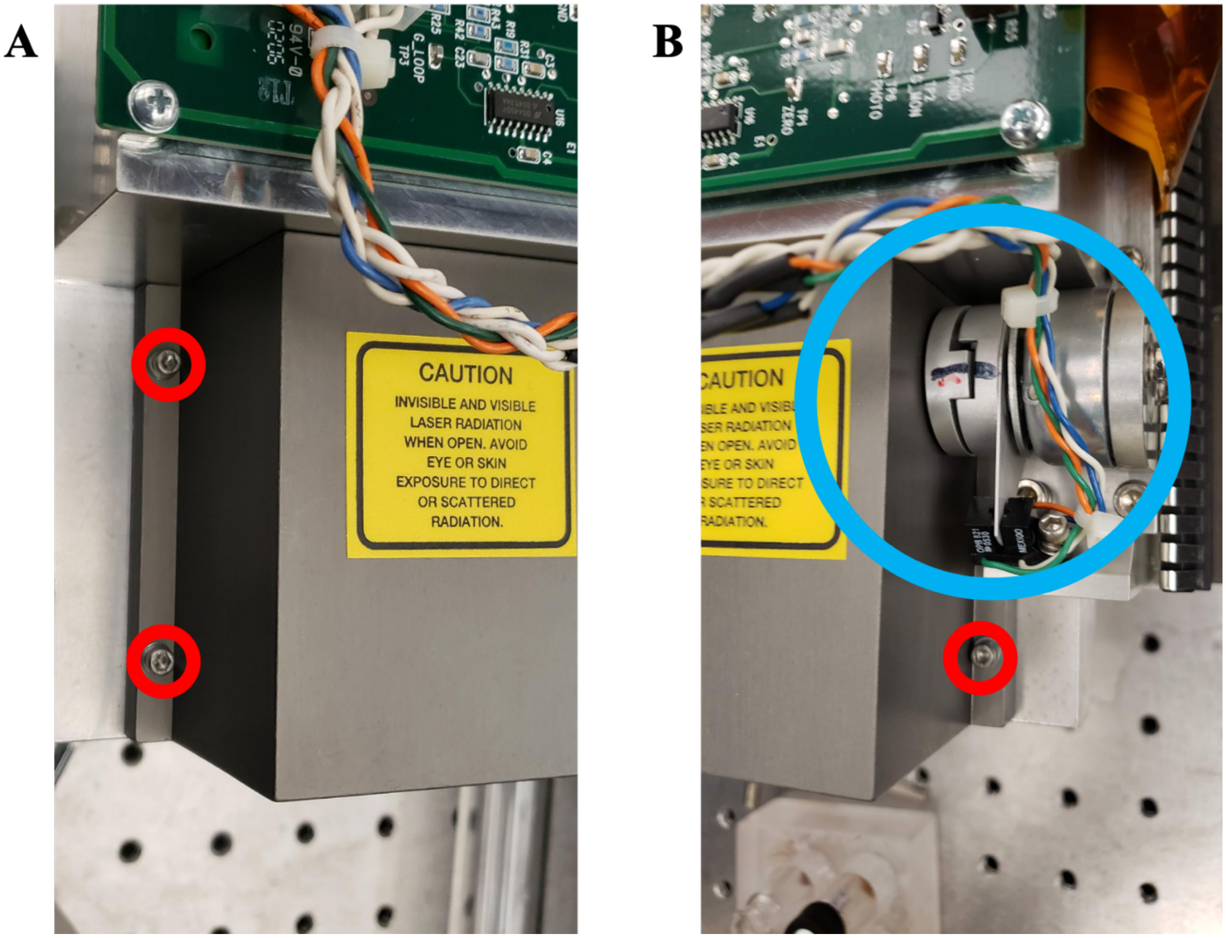

Figure A.4. A) Left side screws (red circle) on the output coupler box that need to be removed to access output coupler. B) Right side screw that needs to be removed to be removed to access output coupler (red circle). The blue circle shows the proper shutter control alignment where the black line is aligned.

APPENDIX B

Upconversion Computer and LabView Upgrades

In order to complete this research, the Macintosh computer needed to be replaced. The program on the original computer was written in LabView 4 and standard at the time of replacement was LabView 15, thus many updates to the LabView virtual instrument (VI) were required in order to function with the current software with a modern operating system. The former setup involved a stepper control board (PCI-Step-2CX) that had no driver that works with any OS newer than Windows 2000 and a stepper amplifier (nu-Drive 2SX-411, 2-axis). Both of these were replaced with a Newport SMC100PP Motion Controller, Single-axis Stepper Motor which was connected to the computer via RS-232-C with an external adapter SMC-USB. The SRS-400 photon counter also needed to be connected to the new computer. A GPIB-USB adapter was used to make this connection.

To enable the LabVIEW VI to work with the current iteration, a conversion program was used that updated the code to a more modern version. As the photon counter still interfaced via GPIB code, minimal changes were needed to enable it to function. On the other hand, the complete interface of the stepper stage was altered to account for the change from a separate stepper control board and stepper amplifier to the single-axis stepper motor. A VISA handle had to be added to all parts of the VI so that it understands where the stepper stage is at that point in time. The program reads the initial location and knows how far to move based upon the length of the scan and how many data points are being obtained. The input view of the VI remains substantially unchanged only removing the calculation of t=0, as the data buffer storage no longer worked, and the calculation would often pull the peak caused by the residual OPA upconversion signal instead of actually t=0. The latest version of the block diagram is on the next several pages.

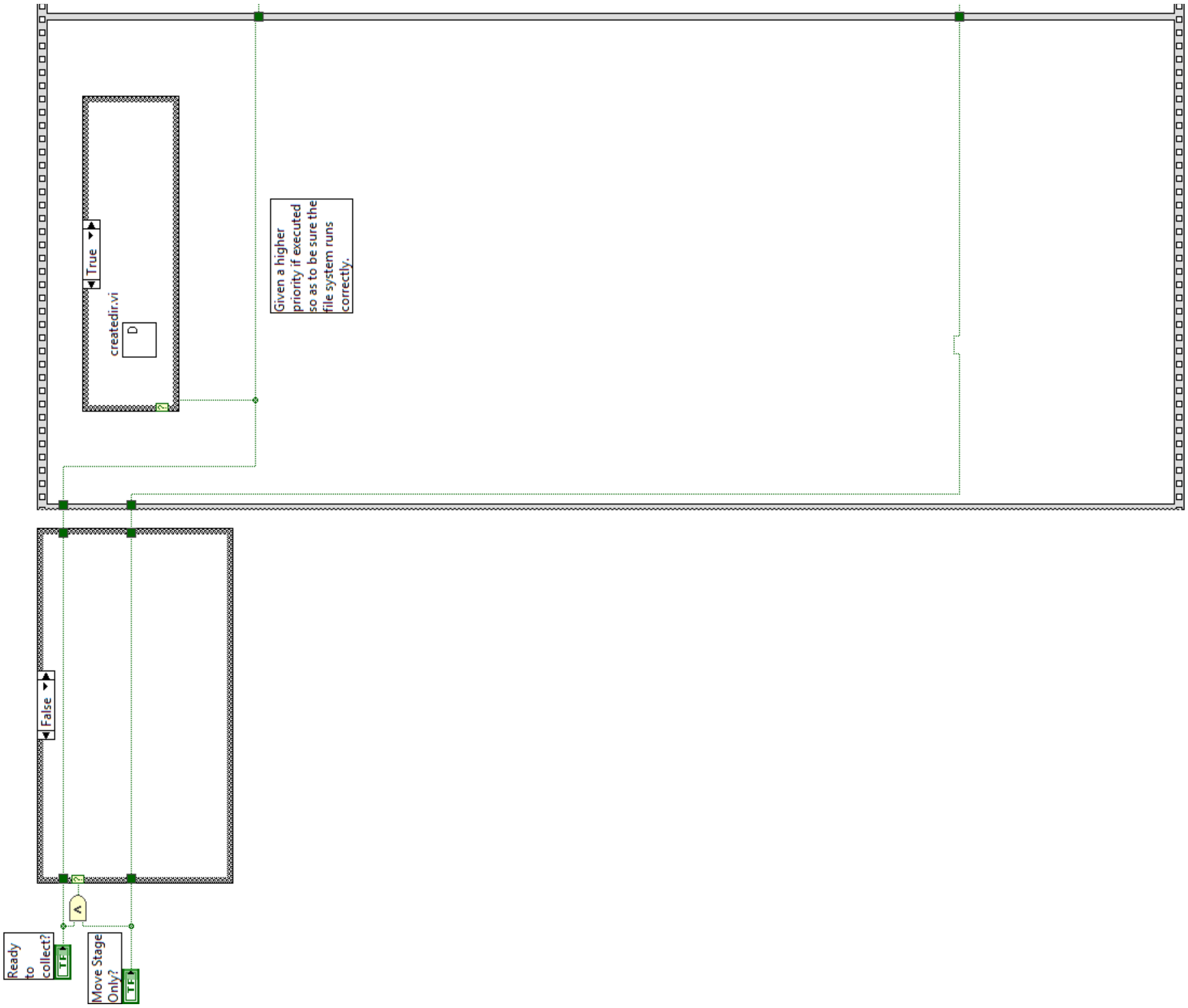

Figure C.1 Block diagram view of the updated LabView VI. (This figure continues on next 6 pages; the top of the current page alligns with the bottom of the next page.)

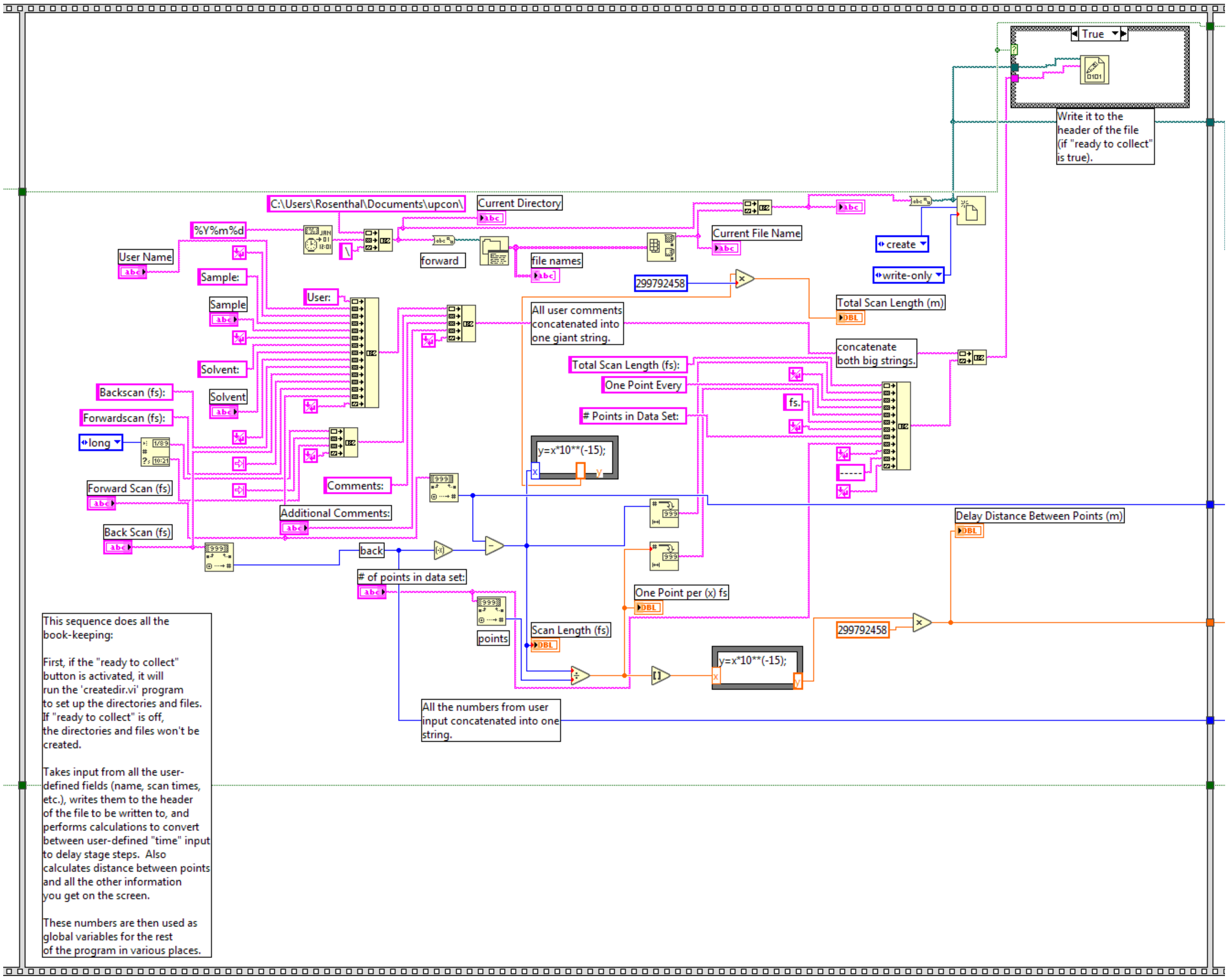

Write it to the header of the file (if "ready to collect" is true).

All user comments concatenated into one giant string.

All the numbers from user input concatenated into one string.

This sequence does all the book-keeping:

First, if the "ready to collect" button is activated, it will run the 'createdir.vi' program to set up the directories and files. If "ready to collect" is off, the directories and files won't be created.

Takes input from all the user-defined fields (name, scan times, etc.), writes them to the header of the file to be written to, and performs calculations to convert between user-defined "time" input to delay stage steps. Also calculates distance between points and all the other information you get on the screen.

These numbers are then used as global variables for the rest of the program in various places.

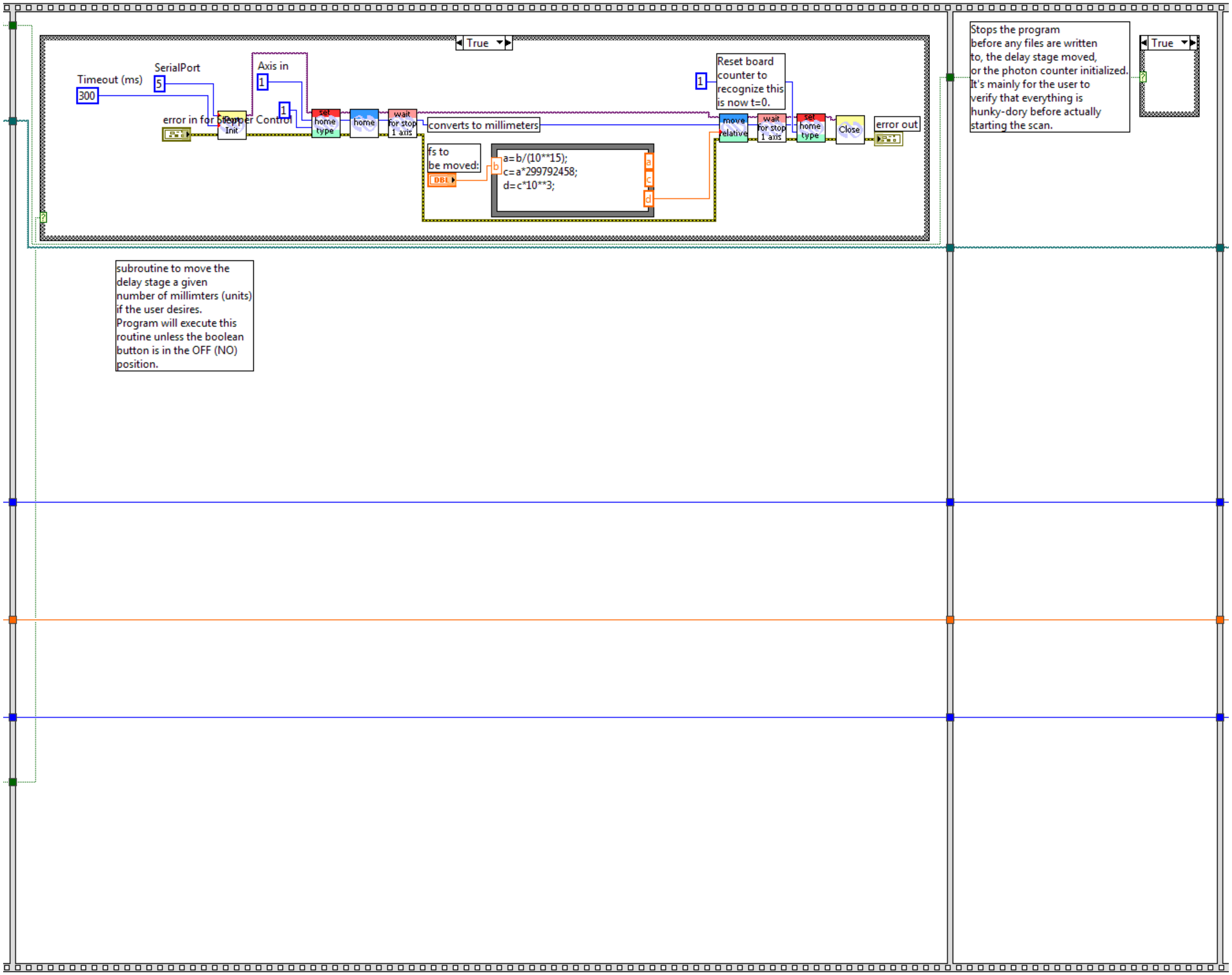

```
a=b/(10**15);
c=a*299792458;
d=c*10**3;
```

subroutine to move the delay stage a given number of millimters (units) if the user desires.
Program will execute this routine unless the boolean button is in the OFF (NO) position.

Stops the program before any files are written to, the delay stage moved, or the photon counter initialized. It's mainly for the user to verify that everything is hunky-dory before actually starting the scan.

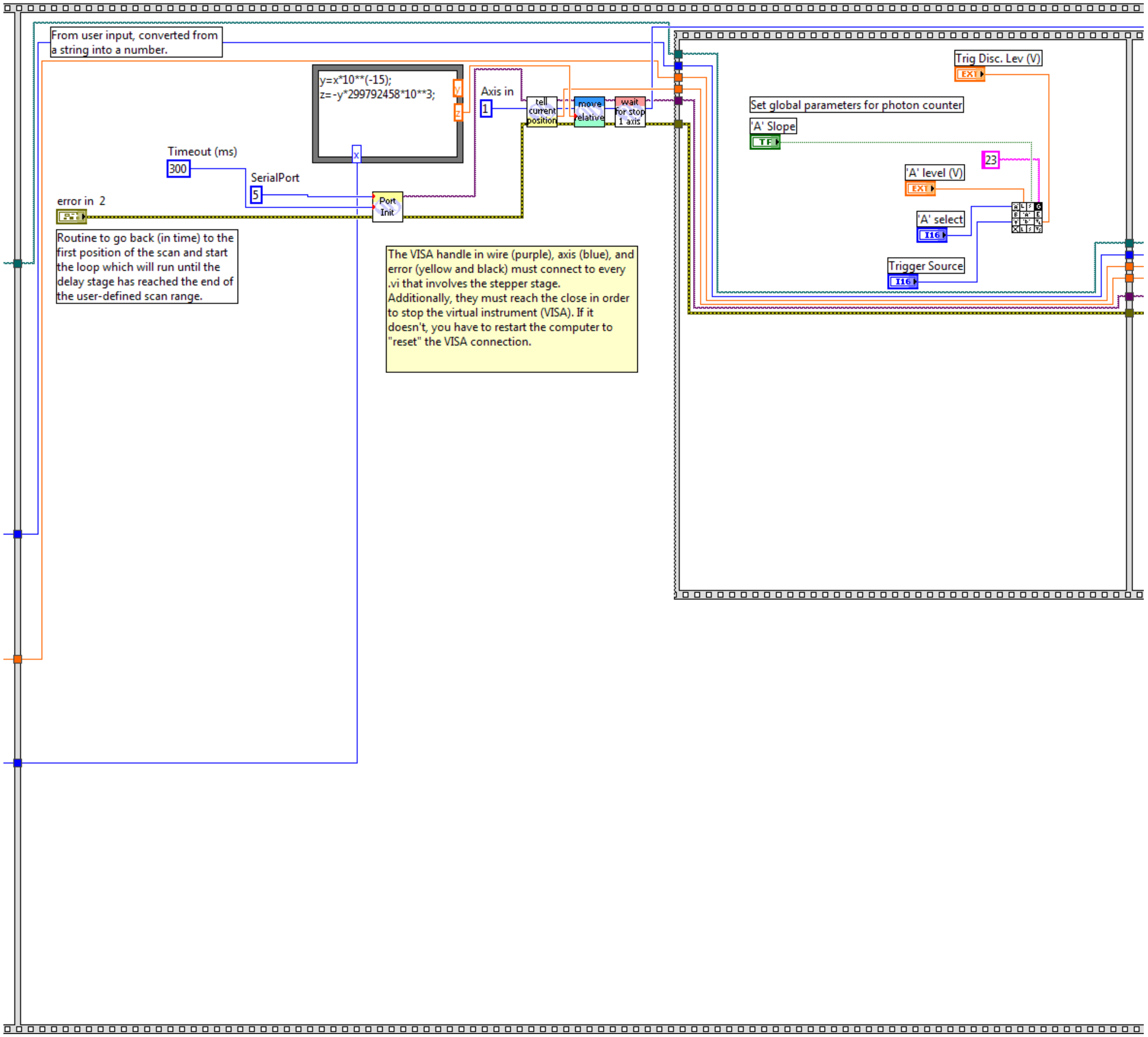

From user input, converted from a string into a number.

```
y=x*10**(-15);
z=-y*299792458*10**3;
```

Routine to go back (in time) to the first position of the scan and start the loop which will run until the delay stage has reached the end of the user-defined scan range.

The VISA handle in wire (purple), axis (blue), and error (yellow and black) must connect to every .vi that involves the stepper stage. Additionally, they must reach the close in order to stop the virtual instrument (VISA). If it doesn't, you have to restart the computer to "reset" the VISA connection.

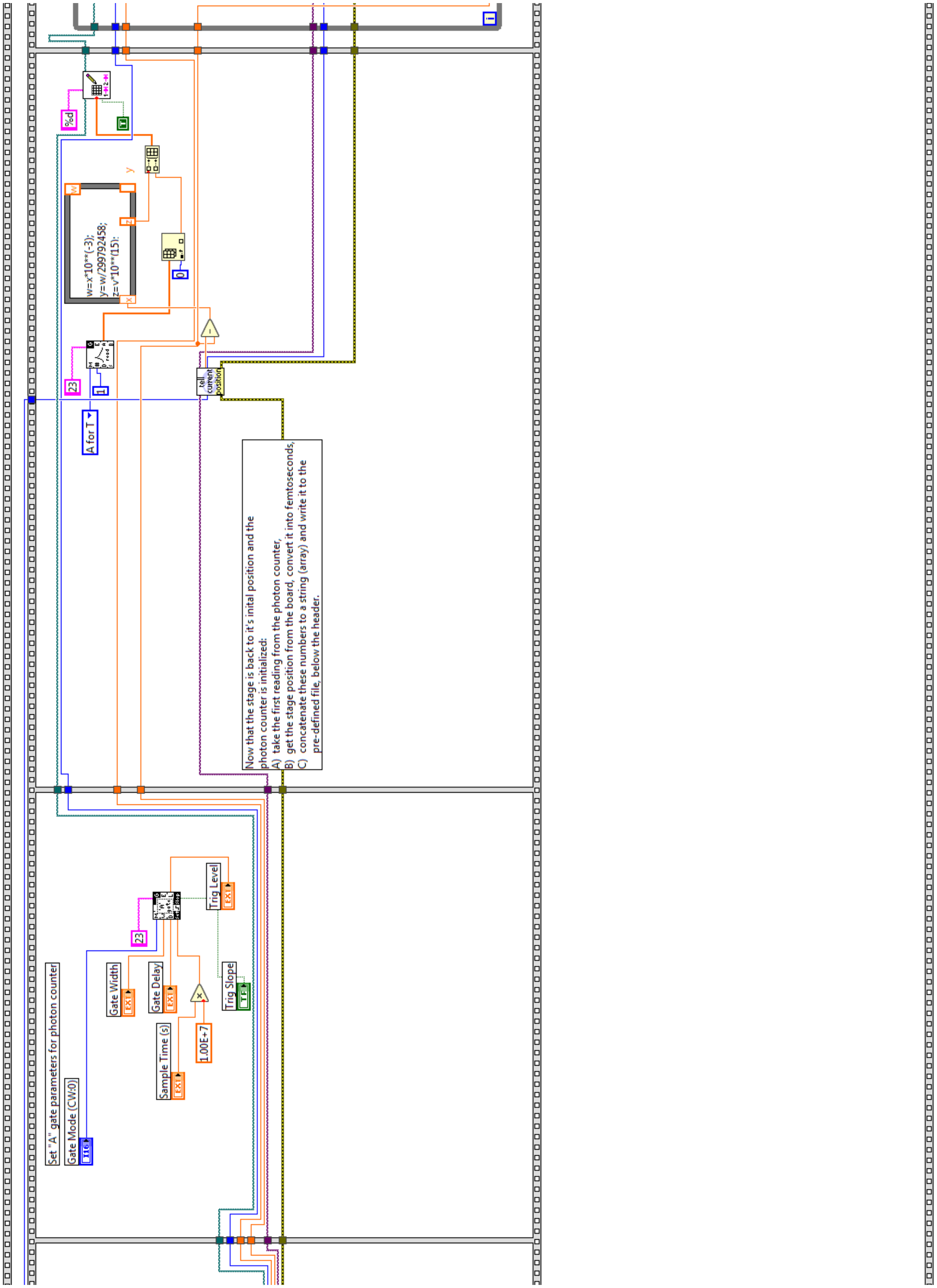

```
w=x*10**(-3);
y=w/299792458;
z=v*10**(15);
```

Now that the stage is back to it's inital position and the photon counter is initialized:
A) take the first reading from the photon counter,
B) get the stage position from the board, convert it into femtoseconds,
C) concatenate these numbers to a string (array) and write it to the pre-defined file, below the header.

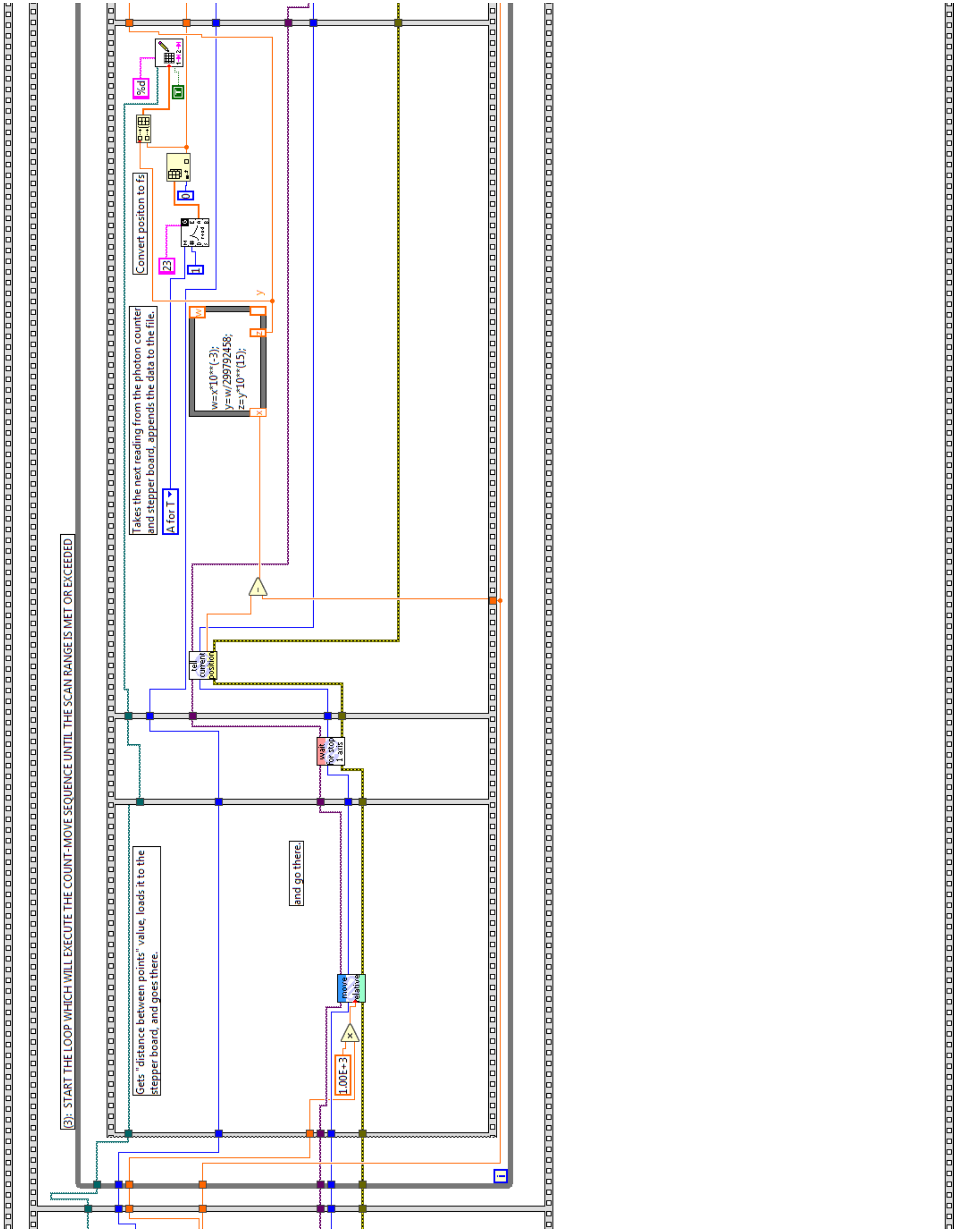
(3): START THE LOOP WHICH WILL EXECUTE THE COUNT-MOVE SEQUENCE UNTIL THE SCAN RANGE IS MET OR EXCEEDED

Gets "distance between points" value, loads it to the stepper board, and goes there.

and go there.

Takes the next reading from the photon counter and stepper board, appends the data to the file.

Convert positon to fs

```
w=x*10**(-3);
y=w/299792458;
z=y*10**(15);
```

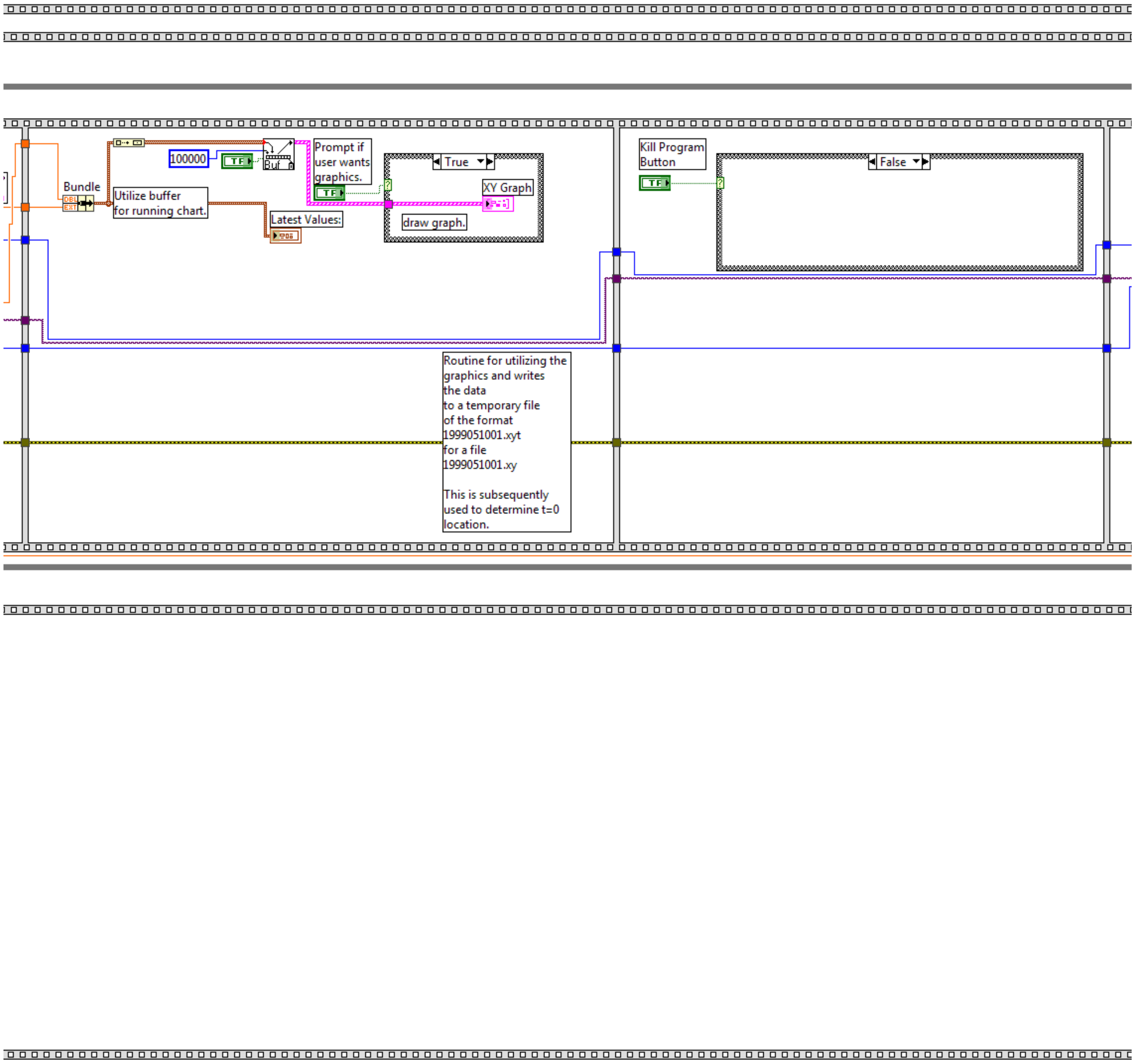

Routine for utilizing the
graphics and writes
the data
to a temporary file
of the format
1999051001.xyt
for a file
1999051001.xy

This is subsequently
used to determine t=0
location.

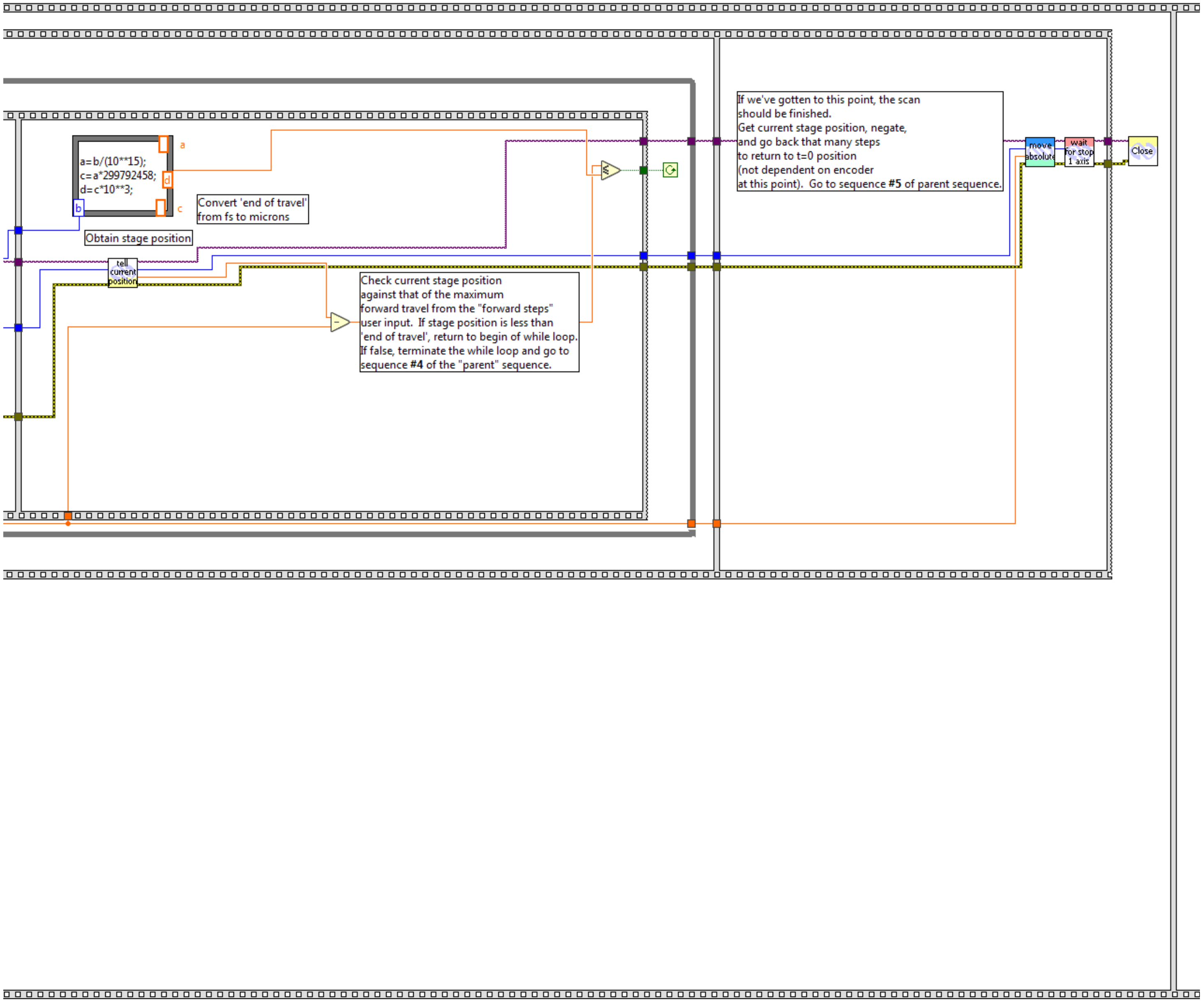

```
a=b/(10**15);
c=a*299792458;
d=c*10**3;
```

Convert 'end of travel' from fs to microns

Obtain stage position

Check current stage position against that of the maximum forward travel from the "forward steps" user input. If stage position is less than 'end of travel', return to begin of while loop. If false, terminate the while loop and go to sequence **#4** of the "parent" sequence.

If we've gotten to this point, the scan should be finished.
Get current stage position, negate, and go back that many steps to return to t=0 position (not dependent on encoder at this point). Go to sequence **#5** of parent sequence.

In the event of an unexpected power loss to the computer or improper shutdown for any reason, the stepper motor can lose its known position and connection to the computer. Instead of a solid green light on the front of the box, it will flash orange. In this case, the stepper motor needs to be manually reset using its software program. Try to ensure that you have located t=0 prior to trying to reconnect to the stepper controller as it typically will reset to its home and not maintain its current location.

1. Open Newport SMC100PP Motion Controller software: SMC100 Utility
2. Click "Discover" on the window.
3. Select COM5 which is the stepper stage and press "Launch Applet."
4. Press Enable in the top left on the main page.
5. If the stage resets to its home position, move the stage under Incremental Motion / PR Move Relative.
    a. Typically, move it in 0.5 increments and watch for the blue spot of the business card.
    b. Once it was close, decrease the increment size until you the blue spot (upconverted signal at t=0) is as bright as possible.
6. Close the SMC Utility and the LabView VI should function normally. If not, restart the computer.

APPENDIX C

Further Surface Passivation Techniques

As discussed in Chapter 3, graded alloy CdS_xSe_{1-x} QDs have been size selectively precipitated with different fraction showing different extents of shell coverage. As observed by Keene et al., dots with higher S:Se ratios showed reduced hole trapping and increased exciton lifetime decay constants.[34] After size selectivity, the population of large dots (> 6 nm) show a material with a thicker CdS shell. Ultrafast fluorescence upconversion on these larger QDs would be particularly interesting to observe if they behave as expected for thick-shelled QDs where reduced trapping occurs because of the thick shell and the graded interface of the material. This thicker shell could also reduce electron trapping and make a more ideal QD structure, but other methods to further confine the charge carriers also exist and are discussed briefly in this appendix.

Instead of using size selection, a thick shell of CdS could be grown onto the as synthesized particles using a technique such as successive ion layer absorption and reaction (SILAR)[32] whereby individual layers of cadmium and sulfur could be deposited onto graded cores. The graded interface should reduce defects at the core shell interface and an additional thick shell of CdS should provide further surface passivation and allow for increased amounts of radiative recombination. Ultrafast fluorescence upconversion spectroscopy would then determine whether the QDs with additional shelling material have effective surface passivation or whether further addition of shell is needed to further improve the photophysical properties of the QDs.

A further layer of ZnS on the surface could also passivate the surface and confine the electrons to the QD structure since it has an even larger band gap and could be carried out using

SILAR.[99] Additionally, a one-pot method for the application of a shell of ZnSe to graded CdSSe NCs has been reported and shown to give very high quantum yields (~95%).[100] These CdSe-based core/gradient alloy shell/shell (CGASS) QDs are synthesized similarly to the graded alloy CdS_xSe_{1-x} QDs discussed in chapter 3, in one-pot using the reactivity difference between Cd and Zn precursors and Se and S precursors. These CGASS QDs can be synthesized to emit colors ranging from blue to the more traditional red often seen for thick-shell QDs.

As discussed previously, Keene *et al.* showed confinement of holes to the core of graded alloy CdS_xSe_{1-x} QDs. As the further addition of wide bandgap ZnS to the surface has resulted in high PLQYs, it is thought that most charge carriers will be combining radiatively inside the nanostructure. With this completely graded interface layer consisting of cadmium, selenium, zinc, and sulfur, there should be few defects at the interface between core/shell. The thick-shell structurally confines the charge carriers while ZnS provides a wide enough electronic barrier. Performing ultrafast fluorescence upconversion spectroscopy of these QDs would enable the trapping mechanisms to be evaluated with the growth of the particle by selectively taking aliquots during growth. It could then be determined which shell layer is responsible for elimination of which trapping mechanism.

To synthesize blue emitting CGASS QDs, 0.4 mmol of CdO was combined with 8 mmol of zinc stearate in 10 mL of ODE and 33.6 mmol of oleic acid. The solution was degassed under vacuum at 140 °C for 20 min and subsequently heated to 300 °C. A swift injection of 0.4 mmol of selenium powder and 8 mmol of sulfur powder dissolved in 4 mL of TOP nucleated growth of the QDs, and shell growth was maintained at 280 °C for 2 hours. Absorbance and fluorescence data in Figure C.1 show that these QDs do emit blue light and STEM-EDS mapping in Figure C.2 shows elemental incorporation of all four components as expected.

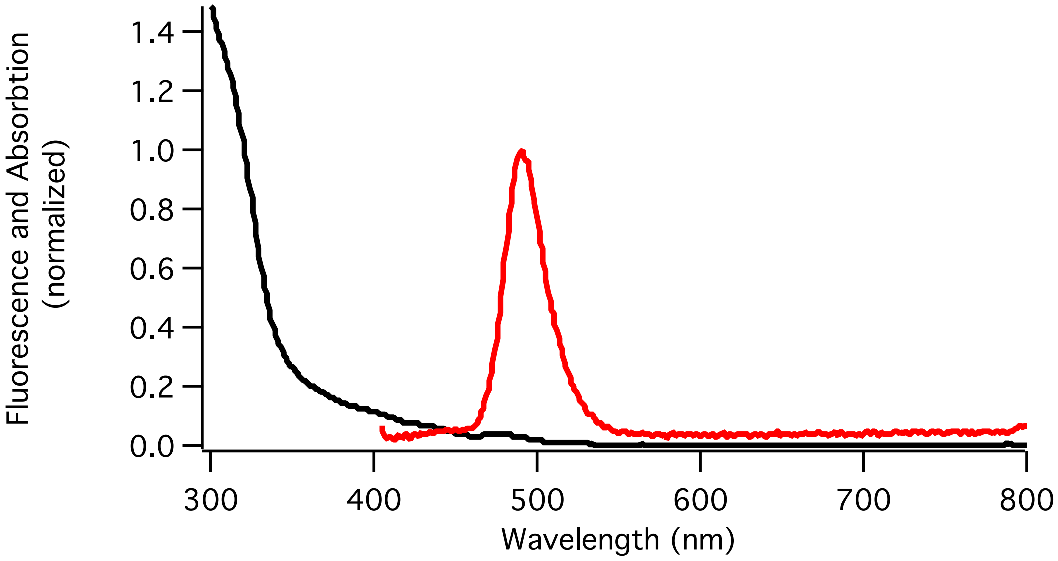

Figure C.1. Absorbance and fluorescence data for CGASS QDs

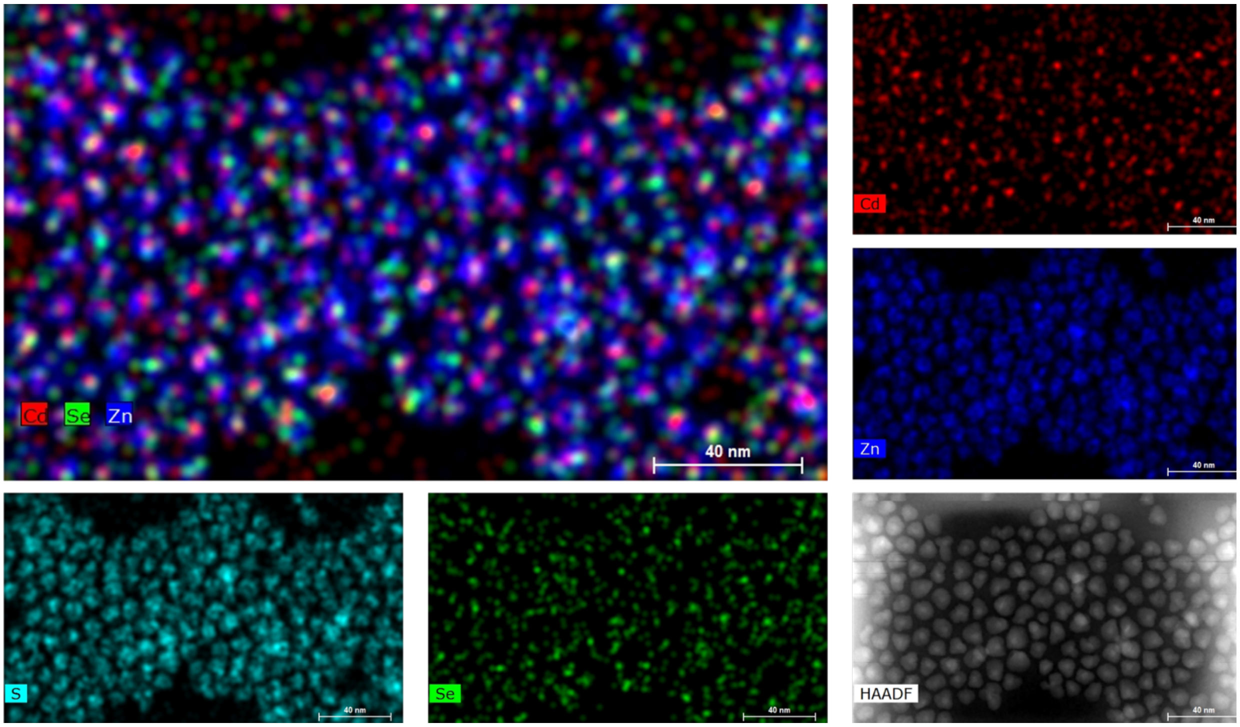

Figure C.2. STEM-EDS mapping of CGASS QDs showing CdSe-rich cores graded to a ZnS-rich shell.

REFERENCES

1. Brus, L. E., Electron–Electron and Electron-Hole Interactions in Small Semiconductor Crystallites: The Size Dependence of the Lowest Excited Electronic State. *J. Chem. Phys.* **1984,** *80* (9), 4403-4409.

2. Rosenthal, S. J., Nanotechnology in Neuroscience Reveals Membrane Mobility Matters. *ACS Chem. Neurosci.* **2019,** *10* (1), 30-32.

3. Kim, T. H.; Jun, S.; Cho, K. S.; Choi, B. L.; Jang, E., Bright and Stable Quantum Dots and Their Applications in Full-Color Displays. *MRS Bull.* **2013,** *38* (9), 712-720.

4. Chang, J. C.; Rosenthal, S. J., A Bright Light to Reveal Mobility: Single Quantum Dot Tracking Reveals Membrane Dynamics and Cellular Mechanisms. *J Phys. Chem. Lett.* **2013,** *4* (17), 2858-2866.

5. Fan, F.; Voznyy, O.; Sabatini, R. P.; Bicanic, K. T.; Adachi, M. M.; McBride, J. R.; Reid, K. R.; Park, Y.-S.; Li, X.; Jain, A.; Quintero-Bermudez, R.; Saravanapavanantham, M.; Liu, M.; Korkusinski, M.; Hawrylak, P.; Klimov, V. I.; Rosenthal, S. J.; Hoogland, S.; Sargent, E. H., Continuous-Wave Lasing in Colloidal Quantum Dot Solids Enabled by Facet-selective Epitaxy. *Nature* **2017,** *544*, 75.

6. Frecker, T.; Bailey, D.; Arzeta-Ferrer, X.; McBride, J.; Rosenthal, S. J., Review—Quantum Dots and Their Application in Lighting, Displays, and Biology. *ECS J. Solid State Sci. Technol.* **2016,** *5* (1), R3019-R3031.

7. Sargent, E. H., Colloidal Quantum Dot Solar Cells. *Nat. Photonics* **2012,** *6* (3), 133-135.

8. Shirasaki, Y.; Supran, G. J.; Bawendi, M. G.; Bulović, V., Emergence of Colloidal Quantum-Dot Light-Emitting Technologies. *Nat. Photonics* **2012,** *7*, 13-23.

9. Kippeny, T.; Swafford, L. A.; Rosenthal, S. J., Semiconductor Nanocrystals: A Powerful Visual Aid for Introducing the Particle in a Box. *J. Chem. Educ.* **2002,** *79* (9), 1094.

10. Efros, A. L.; Rosen, M.; Kuno, M.; Nirmal, M.; Norris, D. J.; Bawendi, M., Band-Edge Exciton in Quantum Dots of Semiconductors with a Degenerate Valence Band: Dark and Bright Exciton States. *Phys. Rev. B* **1996,** *54* (7), 4843-4856.

11. Bowers, M. J.; McBride, J. R.; Rosenthal, S. J., White-Light Emission from Magic-Sized Cadmium Selenide Nanocrystals. *J. Am. Chem. Soc.* **2005,** *127* (44), 15378-15379.

12. Scholes, G. D.; Rumbles, G., Excitons in Nanoscale Systems. *Nat. Mater.* **2006,** *5* (9), 683-696.

13. Kagan, C. R.; Lifshitz, E.; Sargent, E. H.; Talapin, D. V., Building Devices from Colloidal Quantum Dots. *Science* **2016,** *353* (6302), aac5523.

14. Bowers II, M. J.; McBride, J. R.; Garrett, M. D.; Sammons, J. A.; Dukes III, A. D.; Schreuder, M. A.; Watt, T. L.; Lupini, A. R.; Pennycook, S. J.; Rosenthal, S. J., Structure and Ultrafast Dynamics of White-Light-Emitting CdSe Nanocrystals. *J. Am. Chem. Soc.* **2009,** *131* (16), 5730-5731.

15. Rosenthal, S. J.; McBride, J.; Pennycook, S. J.; Feldman, L. C., Synthesis, Surface Studies, Composition and Structural Characterization of CdSe, Core/Shell and Biologically Active Nanocrystals. *Surf. Sci. Rep.* **2007,** *62* (4), 111-157.

16. Ghosh, S.; Kushavah, D.; Pal, S. K., Unravelling the Role of Surface Traps on Carrier Relaxation and Transfer Dynamics in Ultrasmall Semiconductor Nanocrystals. *J. Phys. Chem. C* **2018,** *122* (37), 21677-21685.

17. McBride, J. R.; Pennycook, T. J.; Pennycook, S. J.; Rosenthal, S. J., The Possibility and Implications of Dynamic Nanoparticle Surfaces. *ACS Nano* **2013,** *7* (10), 8358-8365.

18. Pu, C.; Peng, X., To Battle Surface Traps on CdSe/CdS Core/Shell Nanocrystals: Shell Isolation versus Surface Treatment. *J. Am. Chem. Soc.* **2016,** *138* (26), 8134-8142.

19. Hines, M. A.; Guyot-Sionnest, P., Synthesis and Characterization of Strongly Luminescing ZnS-Capped CdSe Nanocrystals. *J. Phys. Chem.* **1996,** *100* (2), 468-471.

20. Chan, W. C. W.; Nie, S., Quantum Dot Bioconjugates for Ultrasensitive Nonisotopic Detection. *Science* **1998,** *281* (5385), 2016.

21. Bruchez, M.; Moronne, M.; Gin, P.; Weiss, S.; Alivisatos, A. P., Semiconductor Nanocrystals as Fluorescent Biological Labels. *Science* **1998,** *281* (5385), 2013.

22. Tamang, S.; Lincheneau, C.; Hermans, Y.; Jeong, S.; Reiss, P., Chemistry of InP Nanocrystal Syntheses. *Chem. Mater.* **2016,** *28* (8), 2491-2506.

23. Kim, S.; Fisher, B.; Eisler, H.-J.; Bawendi, M., Type-II Quantum Dots: CdTe/CdSe(Core/Shell) and CdSe/ZnTe(Core/Shell) Heterostructures. *J. Am. Chem. Soc.* **2003,** *125* (38), 11466-11467.

24. Liu, W.; Choi, H. S.; Zimmer, J. P.; Tanaka, E.; Frangioni, J. V.; Bawendi, M., Compact Cysteine-Coated CdSe(ZnCdS) Quantum Dots for in Vivo Applications. *J. Am. Chem. Soc.* **2007,** *129* (47), 14530-14531.

25. Peng, X.; Schlamp, M. C.; Kadavanich, A. V.; Alivisatos, A. P., Epitaxial Growth of Highly Luminescent CdSe/CdS Core/Shell Nanocrystals with Photostability and Electronic Accessibility. *J. Am. Chem. Soc.* **1997,** *119* (30), 7019-7029.

26. Kippeny, T. C.; Bowers, M. J.; Dukes, A. D.; McBride, J. R.; Orndorff, R. L.; Garrett, M. D.; Rosenthal, S. J., Effects of Surface Passivation on the Exciton Dynamics of CdSe Nanocrystals as Observed by Ultrafast Fluorescence Upconversion Spectroscopy. *J. Chem. Phys.* **2008,** *128* (8), 084713.

27. McBride, J. R.; Kippeny, T. C.; Pennycook, S. J.; Rosenthal, S. J., Aberration-Corrected Z-Contrast Scanning Transmission Electron Microscopy of CdSe Nanocrystals. *Nano Lett.* **2004,** *4* (7), 1279-1283.

28. Talapin, D. V.; Rogach, A. L.; Kornowski, A.; Haase, M.; Weller, H., Highly Luminescent Monodisperse CdSe and CdSe/ZnS Nanocrystals Synthesized in a Hexadecylamine−Trioctylphosphine Oxide−Trioctylphospine Mixture. *Nano Lett.* **2001,** *1* (4), 207-211.

29. Murray, C. B.; Norris, D. J.; Bawendi, M. G., Synthesis and Characterization of Nearly Monodisperse CdE (E = sulfur, selenium, tellurium) Semiconductor Nanocrystallites. *J. Am. Chem. Soc.* **1993,** *115* (19), 8706-8715.

30. Pennycook, T. J.; McBride, J. R.; Rosenthal, S. J.; Pennycook, S. J.; Pantelides, S. T., Dynamic Fluctuations in Ultrasmall Nanocrystals Induce White Light Emission. *Nano Lett.* **2012,** *12* (6), 3038-3042.

31. McBride, J.; Treadway, J.; Feldman, L. C.; Pennycook, S. J.; Rosenthal, S. J., Structural Basis for Near Unity Quantum Yield Core/Shell Nanostructures. *Nano Lett.* **2006,** *6* (7), 1496-1501.

32. Chen, Y.; Vela, J.; Htoon, H.; Casson, J. L.; Werder, D. J.; Bussian, D. A.; Klimov, V. I.; Hollingsworth, J. A., "Giant" Multishell CdSe Nanocrystal Quantum Dots with Suppressed Blinking. *J. Am. Chem. Soc.* **2008,** *130* (15), 5026-5027.

33. Harrison, M. A.; Ng, A.; Hmelo, A. B.; Rosenthal, S. J., CdSSe Nanocrystals with Induced Chemical Composition Gradients. *Isr. J. Chem.* **2012,** *52* (11-12), 1063-1072.

34. Keene, J. D.; McBride, J. R.; Orfield, N. J.; Rosenthal, S. J., Elimination of Hole–Surface Overlap in Graded CdS_xSe_{1-x} Nanocrystals Revealed by Ultrafast Fluorescence Upconversion Spectroscopy. *ACS Nano* **2014,** *8* (10), 10665-10673.

35. Garrett, M. D.; Dukes III, A. D.; McBride, J. R.; Smith, N. J.; Pennycook, S. J.; Rosenthal, S. J., Band Edge Recombination in CdSe, CdS and CdS_xSe_{1-x} Alloy Nanocrystals Observed by Ultrafast Fluorescence Upconversion: The Effect of Surface Trap States. *J. Phys. Chem. C* **2008,** *112* (33), 12736-12746.

36. Kahlow, M. A.; Jarzęba, W. o.; DuBruil, T. P.; Barbara, P. F., Ultrafast Emission Spectroscopy in the Ultraviolet by Time-Gated Upconversion. *Rev. Sci. Instrum.* **1988,** *59* (7), 1098-1109.

37. Hane, J. K.; Prisant, M. G.; Harris, C. B.; Meyer, G. J.; Leung, L. K.; Ellis, A. B., Time-Resolved Luminescence of Electron-Hole Pairs in Cadmium Sulfide Selenide Graded Semiconductors. *J. Phys. Chem.* **1989,** *93* (24), 7975-7977.

38. Burda, C.; El-Sayed Mostafa, A., High-Density Femtosecond Transient Absorption Spectroscopy of Semiconductor Nanoparticles. A Tool to Investigate Surface Quality. *Pure Appl. Chem.* **2000,** *72* (1-2), 165.

39. Guyot-Sionnest, P.; Wehrenberg, B.; Yu, D., Intraband Relaxation in CdSe Nanocrystals and the Strong Influence of the Surface Ligands. *J. Chem. Phys.* **2005,** *123* (7), 074709.

40. Klimov, V. I.; McBranch, D. W.; Leatherdale, C. A.; Bawendi, M. G., Electron and Hole Relaxation Pathways in Semiconductor Quantum Dots. *Phys. Rev. B* **1999,** *60* (19), 13740-13749.

41. Logunov, S.; Green, T.; Marguet, S.; El-Sayed, M. A., Interfacial Carriers Dynamics of CdS Nanoparticles. *J. Phys. Chem. A* **1998,** *102* (28), 5652-5658.

42. Underwood, D. F.; Kippeny, T.; Rosenthal, S. J., Ultrafast Carrier Dynamics in CdSe Nanocrystals Determined by Femtosecond Fluorescence Upconversion Spectroscopy. *J. Phys. Chem. B.* **2001,** *105* (2), 436-443.

43. Garrett, M. D.; Bowers, M. J.; McBride, J. R.; Orndorff, R. L.; Pennycook, S. J.; Rosenthal, S. J., Band Edge Dynamics in CdSe Nanocrystals Observed by Ultrafast Fluorescence Upconversion. *J. Phys. Chem. C* **2008,** *112* (2), 436-442.

44. Underwood, D. F.; Kippeny, T.; Rosenthal, S. J., Charge Carrier Dynamics in CdSe Nanocrystals: Implications for the Use of Quantum Dots in Novel Photovoltaics. *Eur. Phys. J. D.* **2001,** *16* (1-3), 241-244.

45. Kuno, M.; Lee, J. K.; Dabbousi, B. O.; Mikulec, F. V.; Bawendi, M. G., The Band Edge Luminescence of Surface Modified CdSe Nanocrystallites: Probing the Luminescing State. *J. Chem. Phys.* **1997,** *106* (23), 9869-9882.

46. Pokrant, S.; Whaley, K. B., Tight-Binding Studies of Surface Effects on Electronic Structure of CdSe Nanocrystals: The Role of Organic Ligands, Surface Reconstruction, and Inorganic Capping Shells. *Eur. Phys. J. D* **1999,** *6* (2), 255-267.

47. Knowles, K. E.; McArthur, E. A.; Weiss, E. A., A Multi-Timescale Map of Radiative and Nonradiative Decay Pathways for Excitons in CdSe Quantum Dots. *ACS Nano* **2011,** *5* (3), 2026-2035.

48. Jones, M.; Lo, S. S.; Scholes, G. D., Quantitative Modeling of the Role of Surface Traps in CdSe/CdS/ZnS Nanocrystal Photoluminescence Decay Dynamics. *PNAS* **2009,** *106* (9), 3011.

49. Jones, M.; Lo, S. S.; Scholes, G. D., Signatures of Exciton Dynamics and Carrier Trapping in the Time-Resolved Photoluminescence of Colloidal CdSe Nanocrystals. *J. Phys. Chem. C* **2009,** *113* (43), 18632-18642.

50. Kern, S. J.; Sahu, K.; Berg, M. A., Heterogeneity of the Electron-Trapping Kinetics in CdSe Nanoparticles. *Nano Lett.* **2011,** *11* (8), 3493-3498.

51. Califano, M.; Gómez-Campos, F. M., Universal Trapping Mechanism in Semiconductor Nanocrystals. *Nano Lett.* **2013,** *13* (5), 2047-2052.

52. Zhu, H.; Yang, Y.; Hyeon-Deuk, K.; Califano, M.; Song, N.; Wang, Y.; Zhang, W.; Prezhdo, O. V.; Lian, T., Auger-Assisted Electron Transfer from Photoexcited Semiconductor Quantum Dots. *Nano Lett.* **2014,** *14* (3), 1263-1269.

53. García-Santamaría, F.; Brovelli, S.; Viswanatha, R.; Hollingsworth, J. A.; Htoon, H.; Crooker, S. A.; Klimov, V. I., Breakdown of Volume Scaling in Auger Recombination in CdSe/CdS Heteronanocrystals: The Role of the Core−Shell Interface. *Nano Lett.* **2011,** *11* (2), 687-693.

54. Park, Y.-S.; Bae, W. K.; Padilha, L. A.; Pietryga, J. M.; Klimov, V. I., Effect of the Core/Shell Interface on Auger Recombination Evaluated by Single-Quantum-Dot Spectroscopy. *Nano Lett.* **2014,** *14* (2), 396-402.

55. Derfus, A. M.; Chan, W. C. W.; Bhatia, S. N., Probing the Cytotoxicity of Semiconductor Quantum Dots. *Nano Lett.* **2004,** *4* (1), 11-18.

56. Taylor, P. N.; Schreuder, M. A.; Smeeton, T. M.; Grundy, A. J. D.; Dimmock, J. A. R.; Hooper, S. E.; Heffernan, J.; Kauer, M., Synthesis of Widely Tunable and Highly Luminescent Zinc Nitride Nanocrystals. *J. Mat. Chem. C* **2014,** *2* (22), 4379-4382.

57. Xie, R.; Battaglia, D.; Peng, X., Colloidal InP Nanocrystals as Efficient Emitters Covering Blue to Near-Infrared. *J. Am. Chem. Soc.* **2007,** *129* (50), 15432-15433.

58. Niezgoda, J. S.; Harrison, M. A.; McBride, J. R.; Rosenthal, S. J., Novel Synthesis of Chalcopyrite $Cu_xIn_yS_2$ Quantum Dots with Tunable Localized Surface Plasmon Resonances. *Chem. Mater.* **2012,** *24* (16), 3294-3298.

59. Brunetti, V.; Chibli, H.; Fiammengo, R.; Galeone, A.; Malvindi, M. A.; Vecchio, G.; Cingolani, R.; Nadeau, J. L.; Pompa, P. P., InP/ZnS as a Safer Alternative to CdSe/ZnS Core/Shell Quantum Dots: In Vitro and In Vivo Toxicity Assessment. *Nanoscale* **2013,** *5* (1), 307-317.

60. Gary, D. C.; Terban, M. W.; Billinge, S. J. L.; Cossairt, B. M., Two-Step Nucleation and Growth of InP Quantum Dots via Magic-Sized Cluster Intermediates. *Chem. Mater.* **2015,** *27* (4), 1432-1441.

61. Lim, J.; Bae, W. K.; Lee, D.; Nam, M. K.; Jung, J.; Lee, C.; Char, K.; Lee, S., InP@ZnSeS, Core@Composition Gradient Shell Quantum Dots with Enhanced Stability. *Chem. Mater.* **2011,** *23* (20), 4459-4463.

62. Guzelian, A. A.; Katari, J. E. B.; Kadavanich, A. V.; Banin, U.; Hamad, K.; Juban, E.; Alivisatos, A. P.; Wolters, R. H.; Arnold, C. C.; Heath, J. R., Synthesis of Size-Selected, Surface-Passivated InP Nanocrystals. *J. Phys. Chem.* **1996,** *100* (17), 7212-7219.

63. Won, Y.-H.; Cho, O.; Kim, T.; Chung, D.-Y.; Kim, T.; Chung, H.; Jang, H.; Lee, J.; Kim, D.; Jang, E., Highly Efficient and Stable InP/ZnSe/ZnS Quantum Dot Light-Emitting Diodes. *Nature* **2019,** *575* (7784), 634-638.

64. Byun, H. J.; Song, W. S.; Yang, H., Facile Consecutive Solvothermal Growth of Highly Fluorescent InP/ZnS Core/Shell Quantum Dots Using a Safer Phosphorus Source. *Nanotechnology* **2011,** *22* (23), 235605.

65. Reid, K. R.; McBride, J. R.; Freymeyer, N. J.; Thal, L. B.; Rosenthal, S. J., Chemical Structure, Ensemble and Single-Particle Spectroscopy of Thick-Shell InP–ZnSe Quantum Dots. *Nano Lett.* **2018,** *18* (2), 709-716.

66. Yu, W. W.; Qu, L.; Guo, W.; Peng, X., Experimental Determination of the Extinction Coefficient of CdTe, CdSe, and CdS Nanocrystals. *Chem. Mater.* **2003,** *15* (14), 2854-2860.

67. Allen, M. W., Measurement of Fluorescence Quantum Yields. Thermo Fisher Scientific 2010; Technical Note: 52019.

68. Kane, D. J.; Trebino, R., Characterization of Arbitrary Femtosecond Pulses using Frequency-resolved Optical Gating. *IEEE J. Quantum Electron.* **1993,** *29* (2), 571-579.

69. Bhasikuttan, A. C.; Suzuki, M.; Nakashima, S.; Okada, T., Ultrafast Fluorescence Detection in Tris(2,2‘-bipyridine)ruthenium(II) Complex in Solution: Relaxation Dynamics Involving Higher Excited States. *J. Am. Chem. Soc.* **2002,** *124* (28), 8398-8405.

70. Orfield, N. J.; McBride, J. R.; Keene, J. D.; Davis, L. M.; Rosenthal, S. J., Correlation of Atomic Structure and Photoluminescence of the Same Quantum Dot: Pinpointing Surface and Internal Defects That Inhibit Photoluminescence. *ACS Nano* **2015,** *9* (1), 831-839.

71. Reid, K. R.; McBride, J. R.; La Croix, A. D.; Freymeyer, N. J.; Click, S. M.; Macdonald, J. E.; Rosenthal, S. J., Role of Surface Morphology on Exciton Recombination in Single Quantum Dot-in-Rods Revealed by Optical and Atomic Structure Correlation. *ACS Nano* **2018,** *12* (11), 11434-11445.

72. Orfield, N. J.; McBride, J. R.; Wang, F.; Buck, M. R.; Keene, J. D.; Reid, K. R.; Htoon, H.; Hollingsworth, J. A.; Rosenthal, S. J., Quantum Yield Heterogeneity Among Single Nonblinking Quantum Dots Revealed by Atomic Structure-Quantum Optics Correlation. *ACS Nano* **2016,** *10* (2), 1960-1968.

73. Shen, Y.; Gee, M. Y.; Tan, R.; Pellechia, P. J.; Greytak, A. B., Purification of Quantum Dots by Gel Permeation Chromatography and the Effect of Excess Ligands on Shell Growth and Ligand Exchange. *Chem. Mater.* **2013,** *25* (14), 2838-2848.

74. Ng, A.; Poplawsky, J. D.; Li, C.; Pennycook, S. J.; Rosenthal, S. J., Direct Electronic Property Imaging of a Nanocrystal-Based Photovoltaic Device by Electron Beam-Induced Current via Scanning Electron Microscopy. *J. Phys. Chem. Lett.* **2014,** *5* (5), 856-860.

75. Kovtun, O.; Tomlinson, I. D.; Bailey, D. M.; Thal, L. B.; Ross, E. J.; Harris, L.; Frankland, M. P.; Ferguson, R. S.; Glaser, Z.; Greer, J.; Rosenthal, S. J., Single Quantum Dot Tracking Illuminates Neuroscience at the Nanoscale. *Chem. Phys. Lett.* **2018,** *706*, 741-752.

76. Schreuder, M. A.; Xiao, K.; Ivanov, I. N.; Weiss, S. M.; Rosenthal, S. J., White Light-Emitting Diodes Based on Ultrasmall CdSe Nanocrystal Electroluminescence. *Nano Lett.* **2010,** *10* (2), 573-576.

77. Dukes III, A. D.; McBride, J. R.; Rosenthal, S., Luminescent Quantum Dots. *ECS Trans.* **2011,** *33* (3), 3-16.

78. Janke, E. M.; Williams, N. E.; She, C.; Zherebetskyy, D.; Hudson, M. H.; Wang, L.; Gosztola, D. J.; Schaller, R. D.; Lee, B.; Sun, C.; Engel, G. S.; Talapin, D. V., Origin of Broad Emission Spectra in InP Quantum Dots: Contributions from Structural and Electronic Disorder. *J. Am. Chem. Soc.* **2018,** *140* (46), 15791-15803.

79. Kim, T.-G.; Zherebetskyy, D.; Bekenstein, Y.; Oh, M. H.; Wang, L.-W.; Jang, E.; Alivisatos, A. P., Trap Passivation in Indium-Based Quantum Dots Through Surface Fluorination: Mechanism and Applications. *ACS Nano* **2018,** *12* (11), 11529-11540.

80. Li, Y.; Hou, X.; Dai, X.; Yao, Z.; Lv, L.; Jin, Y.; Peng, X., Stoichiometry-Controlled InP-Based Quantum Dots: Synthesis, Photoluminescence, and Electroluminescence. *J. Am. Chem. Soc.* **2019,** *141* (16), 6448-6452.

81. Tessier, M. D.; Baquero, E. A.; Dupont, D.; Grigel, V.; Bladt, E.; Bals, S.; Coppel, Y.; Hens, Z.; Nayral, C.; Delpech, F., Interfacial Oxidation and Photoluminescence of InP-Based Core/Shell Quantum Dots. *Chem. Mater.* **2018,** *30* (19), 6877-6883.

82. Hahm, D.; Chang, J. H.; Jeong, B. G.; Park, P.; Kim, J.; Lee, S.; Choi, J.; Kim, W. D.; Rhee, S.; Lim, J.; Lee, D. C.; Lee, C.; Char, K.; Bae, W. K., Design Principle for Bright, Robust, and Color-Pure InP/$ZnSe_xS_{1-x}$/ZnS Heterostructures. *Chem. Mater.* **2019,** *31* (9), 3476-3484.

83. Cao, F.; Wang, S.; Wang, F.; Wu, Q.; Zhao, D.; Yang, X., A Layer-by-Layer Growth Strategy for Large-Size InP/ZnSe/ZnS Core–Shell Quantum Dots Enabling High-Efficiency Light-Emitting Diodes. *Chem. Mater.* **2018,** *30* (21), 8002-8007.

84. Kim, Y.; Ham, S.; Jang, H.; Min, J. H.; Chung, H.; Lee, J.; Kim, D.; Jang, E., Bright and Uniform Green Light Emitting InP/ZnSe/ZnS Quantum Dots for Wide Color Gamut Displays. *ACS Appl. Nano Mater.* **2019,** *2* (3), 1496-1504.

85. Brodu, A.; Ballottin, M. V.; Buhot, J.; van Harten, E. J.; Dupont, D.; La Porta, A.; Prins, P. T.; Tessier, M. D.; Versteegh, M. A. M.; Zwiller, V.; Bals, S.; Hens, Z.; Rabouw, F. T.; Christianen, P. C. M.; de Mello Donega, C.; Vanmaekelbergh, D., Exciton Fine Structure and Lattice Dynamics in InP/ZnSe Core/Shell Quantum Dots. *ACS Photonics* **2018,** *5* (8), 3353-3362.

86. Rafipoor, M.; Dupont, D.; Tornatzky, H.; Tessier, M. D.; Maultzsch, J.; Hens, Z.; Lange, H., Strain Engineering in InP/(Zn,Cd)Se Core/Shell Quantum Dots. *Chem. Mater.* **2018,** *30* (13), 4393-4400.

87. Chandrasekaran, V.; Tessier, M. D.; Dupont, D.; Geiregat, P.; Hens, Z.; Brainis, E., Nearly Blinking-Free, High-Purity Single-Photon Emission by Colloidal InP/ZnSe Quantum Dots. *Nano Lett.* **2017,** *17* (10), 6104-6109.

88. Biadala, L.; Siebers, B.; Beyazit, Y.; Tessier, M. D.; Dupont, D.; Hens, Z.; Yakovlev, D. R.; Bayer, M., Band-Edge Exciton Fine Structure and Recombination Dynamics in InP/ZnS Colloidal Nanocrystals. *ACS Nano* **2016,** *10* (3), 3356-3364.

89. Ellingson, R. J.; Blackburn, J. L.; Yu, P.; Rumbles, G.; Mićić, O. I.; Nozik, A. J., Excitation Energy Dependent Efficiency of Charge Carrier Relaxation and Photoluminescence in Colloidal InP Quantum Dots. *J. Phys. Chem. B* **2002,** *106* (32), 7758-7765.

90. Hughes, K. E.; Stein, J. L.; Friedfeld, M. R.; Cossairt, B. M.; Gamelin, D. R., Effects of Surface Chemistry on the Photophysics of Colloidal InP Nanocrystals. *ACS Nano* **2019,** *13* (12), 14198-14207.

91. Bae, W. K.; Padilha, L. A.; Park, Y.-S.; McDaniel, H.; Robel, I.; Pietryga, J. M.; Klimov, V. I., Controlled Alloying of the Core–Shell Interface in CdSe/CdS Quantum Dots for Suppression of Auger Recombination. *ACS Nano* **2013,** *7* (4), 3411-3419.

92. Freymeyer, N. J.; Click, S. M.; Reid, K. R.; Chisholm, M. F.; Bradsher, C. E.; McBride, J. R.; Rosenthal, S. J., Effect of Indium Alloying on the Charge Carrier Dynamics of Thick-Shell InP/ZnSe Quantum Dots. *J. Chem. Phys.* **2020**, Accepted.

93. Toufanian, R.; Piryatinski, A.; Mahler, A. H.; Iyer, R.; Hollingsworth, J. A.; Dennis, A. M., Bandgap Engineering of Indium Phosphide-Based Core/Shell Heterostructures Through Shell Composition and Thickness. *Front. Chem.* **2018,** *6* (567).

94. Stein, J. L.; Holden, W. M.; Venkatesh, A.; Mundy, M. E.; Rossini, A. J.; Seidler, G. T.; Cossairt, B. M., Probing Surface Defects of InP Quantum Dots Using Phosphorus Kα and Kβ X-ray Emission Spectroscopy. *Chem. Mater.* **2018,** *30* (18), 6377-6388.

95. De, C. K.; Mandal, S.; Roy, D.; Ghosh, S.; Konar, A.; Mandal, P. K., Ultrafast Dynamics and Ultrasensitive Single-Particle Intermittency in Small-Sized Toxic Metal Free InP-Based Core/Alloy-Shell/Shell Quantum Dots: Excitation Wavelength Dependency Toward Variation of PLQY. *J. Phys. Chem. C* **2019,** *123* (46), 28502-28510.

96. Rowland, C. E.; Liu, W.; Hannah, D. C.; Chan, M. K. Y.; Talapin, D. V.; Schaller, R. D., Thermal Stability of Colloidal InP Nanocrystals: Small Inorganic Ligands Boost High-Temperature Photoluminescence. *ACS Nano* **2014,** *8* (1), 977-985.

97. Qidwai, A. A.; Woods, J., Defect Levels in Indium and Gallium Doped Zinc Selenide. *J. Cryst. Growth* **1982,** *59* (1), 217-222.

98. Lee, S. H.; Kim, Y.; Jang, H.; Min, J. H.; Oh, J.; Jang, E.; Kim, D., The Effects of Discrete and Gradient Mid-Shell Structures on the Photoluminescence of Single InP Quantum Dots. *Nanoscale* **2019,** *11* (48), 23251-23258.

99. Xie, R.; Kolb, U.; Li, J.; Basché, T.; Mews, A., Synthesis and Characterization of Highly Luminescent CdSe−Core CdS/$Zn_{0.5}Cd_{0.5}S$/ZnS Multishell Nanocrystals. *J. Am. Chem. Soc.* **2005,** *127* (20), 7480-7488.

100. Roy, D.; Routh, T.; Asaithambi, A. V.; Mandal, S.; Mandal, P. K., Spectral and Temporal Optical Behavior of Blue-, Green-, Orange-, and Red-Emitting CdSe-Based Core/Gradient Alloy Shell/Shell Quantum Dots: Ensemble and Single-Particle Investigation Results. *J. Phys. Chem. C* **2016,** *120* (6), 3483-3491.